High-Resolution X-Ray Scattering Studies of Thin Film Superconductors and Semiconductors

Wen-Jih Lin

A thesis submitted in fulfilment of the requirements

for the degree of Doctor of Philosophy

to the

University of Edinburgh

1998

Declaration

This thesis has been composed by myself and it has not been submitted in any previous application for a degree. The work reported within was executed by me, unless otherwise stated. Some of the results of this thesis have appeared in:

1. J.H.Li, W.J.Lin, P.D.Hatton, Z.H.Mai, and S.F.Xu, *Triple-axis x-ray diffraction analysis of highly oriented $YBa_2Cu_3O_7$ thin films on $LaAlO_3$ substrates*, Physica C **245**, 139 (1995)

2. W.J.Lin, J.H.Li, P.D.Hatton, and Z.H.Mai, *Morphology and interface structure of pulsed laser deposited $YBa_2Cu_3O_7$ thin films on $LaAlO_3$ substrates*, Chinese Journal of Physics, **34**, 621 (1996)

3. W.J.Lin, P.D.Hatton, F.Baudenbacher, and J.Santiso, *A high-resolution synchrotron x-ray scattering study of the surface and interface structures of $YBa_2Cu_3O_x$ thin films*, Physica B, in publishing

January 1998

Acknowledgement

It is a delightful stage to writing this acknowledgement after my study in UK. There are many people to whom I would like to express my greatest appriciation. First, I would like to thank to my supervisor, Dr. P. D. Hatton in Durham. Without his guidance and help, there will not be this thesis. I would also like to thank my second supervisor, Professor G. S. Pawley in Edinburgh for his kindness of discussion and encouragement.

I am grateful to all group members, Dr. C. H. Du, Dr. I. Pape, T. P. A. Hase and Y. Su, for their great assistant in experiment and discussion. Especially, I would like to give my thanks to Professor S. F. Cui of Chinese Academy of Science, China, for his helpful discussion during his visit in Durham.

I sincerely acknowledge all the collaborators as well: Dr. J. H. Li of Chinese Academy of Science, and Dr. R. E. Somekh, Dr. F. Baudenbacher, Dr. G. A. Wagner, Dr. S. C. Fan, Dr. J. Santiso, of Cambridge IRC. I would also like to thank Dr. C. C. Tang of Daresbury for his assistance during the experiments in Daresbury. Furthermore, Mr. M. C. Miller for his help in using PINCER program desired my greatest thanks. The technicians and secretaries both in Edinburgh and Durham, Mr. H. Vass, Mrs. E. McKirdy and Mrs. E. McIvor, and Mr. J. Dobson, helped me a lot during my studies and I would like to express my thanks to them, too.

Finally, I would like to thank Marie for her companionship and encouragement during my study. I would also like to thank my family for their totally, unselfish support all the time. Especially my parents, they can not be thanked enough for everything they have done. This thesis is dedicated to them.

Abstract

High-resolution x-ray scattering has attracted intensive attention for both fundamental research and industrial applications. Recently, the advance of synchrotron radiation sources has dramatically improved x-ray intensities, brightness and resolution, which has enhanced the ability of x-ray scattering studies. In spite of weak scattering cross-sections, high-brilliance x-ray sources have made the studies of surfaces and interfaces possible. In the last decade, many new x-ray techniques such as glancing-incidence-x-ray-reflectometry, crystal-truncation-rod analysis and reciprocal-space-mapping have been established and have had great success in exploring the structure of various materials.

This thesis starts with a review of high-resolution x-ray scattering which covers both the theoretical and the experimental backgrounds. Near perfect semiconducting thin films are examined to demonstrate the abilities of high-resolution x-ray scattering. Glancing incidence x-ray reflectometry was used to explore the interface morphology of a $Si_{0.1}Ge_{0.9}$ heterostructure grown with and without antimony acting as a surfactant. The results demonstrate that the film is smoother when grown with a sub-monolayer of the surfactant. Furthermore, due to the existence of the surfactant during growth, abnormally strong scattering was found from the long-range coherent conformal roughness.

$YBa_2Cu_3O_x$ thin film superconductors grown on various substrates from different growers were studied. Using high-resolution x-ray scattering techniques, the sample quality was measured using the position and the width of the Bragg reflections. By analysing the reciprocal space maps, the surface parallel lattice parameters were also determined.

One of the best samples, the $YBa_2Cu_3O_x$ grown on $SrTiO_3$ by pulsed laser deposition was studied further. The results suggest that an ultra-high-quality crystal with thousands Ångstrom vertical and microns horizontal correlation occupies nearly 95% of volume. However, due to the interface roughness, the scattering from this crystal can only be observed with low angle Bragg reflections and, therefore, is often ignored. Because this type of film is the best single crystal high-T_c superconductor, it will be the doorway to understanding high-T_c superconductivity.

Contents

Chapter 1

Introduction

1.1 General introduction

Thin films are widely employed in many areas. The existence of surfaces and interfaces represent breaks in the otherwise infinite periodicity of the lattice, and so they often exhibit properties different from those of the bulk[1]. However, these properties are often dependent upon the quality of the thin film. Imperfections within such thin films, such as surface and interface roughness, strain, defects, and grain boundaries, are known to affect the optical, electrical and mechanical properties of samples[2,3,4,5,6,7,8]. Furthermore, the thickness of the thin film is essential for optimum performance in many applications[9,10]. The understanding and control of the imperfections of such films is one of the essential factors in fabricating materials with desired properties. Therefore, studies of thin film structures, including the morphology of surface and buried interfaces, are important in many fields of industry and technology.

1.2 Review of experimental techniques for surface/interface and thin film structure analysis

Since the existence of surface, interface and the finite thickness that of thin films provide an alteration of the properties of materials, studies of structural variation

from bulk materials are crucial. Both the crystallographic and chemical structures of thin films are strongly linked to their bulk counterparts. Generally speaking, the techniques for surface, interface and thin film structure studies can be classified into direct and indirect measurements. The direct measurement techniques usually refer to enhanced microscopy techniques which "visualise" the structures of small features of material surfaces. Fine "probes" scan the surface of materials and detectors collect signals simultaneously from the interaction between the probes and the samples. By mapping the signal to the position of the probe, an image of the specimen is made.

To observe details of the sample, scattering experiments are also employed. The probing beams, such as x-rays or electrons, are fired towards the specimen and a certain volume of the specimen is illuminated. Due to the interaction between the specimen atoms and the probing beams, elastic or inelastic scattering will occur and then secondary radiation or particles are generated. By collecting the secondary radiation, the structure of specimens can be determined. Unlike the direct measurement, such probes do not "scan" on the sample surface. The use of scattering techniques probes a large volume of the specimen, and the results are averaged across the active region. However, by choosing special surface sensitive probes, such as electron beams or a special geometry, such as grazing incidence, the active region being probed can be restricted to surface or near-surface areas. Therefore, these techniques can become surface-sensitive. Because these scattering techniques often reveal the structure in wavevector, or reciprocal space rather than in direct space, transformations have to be applied to the experimental data in order to determine the crystal structure in direct space. Therefore, they are often referred to as indirect measurements.

Some of the direct and indirect techniques employed frequently in surface, interface and thin film structural studies are briefly reviewed in this chapter. We will concentrate our attention on those techniques which provide information on the atomic or crystallographic structure of thin films and surfaces/interfaces. There are still many other techniques which have been widely employed to study the detail of thin films which have been discussed comprehensively by Brundle et al.[11]

1.2.1 Direct measurements

Scanning Electron Microscopy (SEM)

Scanning electron microscopy (SEM) is one of the simplest methods for examining the surface of materials[11,12]. In SEM, an electron beam is focused into a fine probe and subsequently scanned over a small area. As the beam interacts with the sample, it induces secondary electrons which are then collected by a detector. In mapping the signal intensity of the secondary electrons to the position of the probe, an image of the sample surface within the scan area can be formed. The best lateral resolution is about 1 nm, depending on the accelerating voltage of the electron beam. The probed depth also depends on the accelerating voltage, ranging from a few nm to a few μm. However, depth profiling is difficult using SEM. To avoid the charging problem of the primary electrons, testing specimens have to be electrically conductive, or a thin conducting film needs to be coated on the top of the sample. Furthermore, SEM measurements can only be undertaken under high vacuum conditions. Nevertheless, SEM is a widely employed technique of great utility. SEM was also employed to determine the structure of $YBa_2Cu_3O_x$ thin films[13,14,15]. Particularly, noteworthy for the latter chapter of this thesis is the use of SEM in determining the orientation of multiphase in $YBa_2Cu_3O_x$ thin films.

Transmission Electron Microscopy (TEM)

Another version of electron microscopy, widely employed in thin film structure studies, is transmission electron microscopy (TEM). In TEM, a thin solid specimen with a thickness of about 200 nm, or less, is bombarded with a highly focused, monoenergetic electron beam. TEM be operated in two different modes: diffraction and image. In diffraction mode, the detector is placed behind the sample and the optical elements collect the electron transmission diffraction pattern of the illuminated area. When TEM is operated in diffraction mode, it is similar to low-energy electron diffraction (LEED) which will be briefly reviewed later. Because the electron beam is highly focused, selected-area diffraction (SAD, sometimes referred to as micro-diffraction) then becomes possible. When TEM is operated in image

mode, a contrast image of the illuminated sample area is produced. The contrast is due to various effects such as the dislocation density, thickness inhomogeneous, diffraction contrast, etc. The principle of this mode is similar to x-ray topography except its probe is electrons instead of x-rays. Because of the highly focused and highly monochromated electron beam, the lateral resolution can be as good as 2Å which is much better than SEM. Thus, atomic-scale imaging is possible. However, like SEM, the samples need to be electrically conducting, or coated, and vacuum system is needed. One of the most successful applications of TEM in thin film structure determination is high-resolution cross-section transmission election microscopy (HRXTEM) which can reveal details of the depth dependent atomic structure. In HRXTEM, delicate sample preparation is needed in obtaining ultra-thin cross-section specimens. The interface atomic structure of high-quality $YBa_2Cu_3O_x$ thin films were precisely determined by HRXTEM[16,17,18].

X-ray Topography

X-ray topography is employed to image defects such as dislocations, precipitates, fault planes and local blisters and cracks in near perfect samples including single crystal and epitaxial films[11,19,20]. An x-ray topograph is an image of diffracted intensity across the test specimen. Contrast is created by local variations in the intensity caused by changes in the diffraction conditions, and is seen frequently due to the strain fields associated with defects. A topograph must be interpreted with the dynamical theory (Dynamical theory will be reviewed in Chapter 2). Although the lateral resolution of x-ray topography (~ 1 μm) is about 1000 times poorer than TEM, much smaller strains (~ 10^{-6}) can be detected and larger sample areas (~ 1 – 10 cm) can be explored. Conventionally, the depth probed is about 1 μm thick. The minimum probing thickness, however, can be reduced to about 0.1 μm by employing grazing incidence geometry, to produce surface-sensitive topography.

Scanning Tunnelling Microscopy (STM) and Atomic Force Microscopy (AFM or Scanning Force Microscopy SFM)

Scanning tunnelling microscopy (STM) and its related offspring technique, atomic force microscopy (AFM), are real-space imaging techniques, which can produce topographic images of a surface with atomic resolution in all three dimensions[11,12,21,22]. The STM was first invented by Binnig and Rohrer in 1981[23] who were awarded the Nobel Prize for Physics in 1986. In STM, a solid specimen in air or vacuum is scanned by a sharp tip located within a few Å of the surface. A quantum-mechanical tunnelling current flows between those atoms on the surface and those on the tip. The magnitude of the tunnelling current strongly depends on the separation between the specimen surface and the tip. When the tip scans across the sample surface, the surface morphology will be recorded by the variation of the tunnelling current. On the other hand, the specimen surface can also be mapped by measuring the tiny feedback adjustment of the separation between the tip and the surface so that the tunnelling current is able to remain constant. The resolution of STM is typically 0.01Å vertically and 1Å laterally. Because STM measures the tunnelling current, the samples can be either conductors or semiconductors. For insulators, a conductive coating is required as for SEM, TEM, etc. In addition, the results of STM are extremely sensitive to surface oxidation, which often changes the surface conductivity. In AFM, instead of the tunnelling current, it is the atomic force between the tip and the surface which is kept constant, and the movement of the tip maps the surface. The resolution of AFM is typically about 0.1Å vertically and a few Å laterally. AFM can be applied to all kinds of materials including liquids. It does not require the sample surface to be electrically conductive, nor vacuum conditions. Both STM and AFM are superior for surface morphology mapping, however, depth profiling is not possible in either case. At an early stage of growth, the skew dislocations of $YBa_2Cu_3O_x$ thin films were reported by both STM and AFM[24,25,26,27,28].

1.2.2 Indirect measurements using electrons

Low Energy Electron Diffraction (LEED)

Low energy electron diffraction (LEED) is one of the most popular techniques in examining the surface or near-surface structure of materials[12,21,29]. The first LEED experiment was performed by Davisson and Germer in 1927 to demonstrate the wave nature of electrons[30]. Low-energy electrons, with energy ranging from 10 to 1000 eV, are made incident on the specimen, at the surface normal direction and diffracted according to Bragg's law. A fluorescent screen is typically used to collect the diffracted electrons. A Faraday cup or some modern detectors can also be used to increase the spatial resolution. Because the electrons interact strongly with materials, their penetration depth is only a few atomic layers. As a result, LEED is extremely surface-sensitive. However, some difficulties arise in using the technique. Firstly, because the samples are bombarded by electrons, only materials with reasonable conductivity can be investigated. Insulators pose difficulties because of the charge accumulated on the sample, preventing the incident beam from striking the surface, and eventually removing the LEED pattern. Secondly, the use of LEED for quantitative determinations of atomic positions on a surface is complicated by the multiple scattering of the electron, which is highly sensitive to the scattering geometry. The sample alignment has to be set precisely prior to LEED measurement. The multiple scattering effects also require massive calculations for the analysis of the results. Additionally, a high-sensitivity detector is essential for measuring the weak reflections. LEED is widely used to determine surface crystallography and microstructure, such as surface reconstruction. It can also be used to determine surface cleanliness. However, the depth probed is generally less than 20Å, which is too short for exploring the buried interface in many cases.

Reflection High-Energy Electron Diffraction (RHEED)

In reflection high-energy electron diffraction (RHEED), a beam of high-energy electrons (typically 5 – 50 keV) is accelerated towards the surface of a conducting or semiconducting sample crystal. Unlike LEED, the primary electron beam strikes the

sample surface at a grazing angle (~5 – 10°) and the scattering is also at grazing angle. This geometry is similar to grazing incidence x-ray diffraction (GIXD) which will be reviewed later. Because the wavelength of the electrons is shorter than inter-atomic spacing, the electron beam can be diffracted by the surface atoms according to Bragg's law and then a "streak-like" diffraction pattern can be observed. The RHEED pattern directly reflects the structure of the sample surface such as the surface symmetry, lattice constant, and degree of perfection. One of the major uses of RHEED is to monitor crystal structure during film growth in ultrahigh vacuum. The intensity oscillation as a function of film coverage is an indication of whether the growth is two-dimensional or three-dimensional. The probing depth is 2 – 100 Å and the lateral resolution can be as good as a few nm. As with other electron-probing techniques like LEED or SEM, high vacuum systems and conducting samples are essential. RHEED has been used by several groups to determine the growth model of $YBa_2Cu_3O_x$ thin films on various substrates[31,32].

1.2.3 Indirect measurements using x-rays

Generally speaking, x-ray scattering is a technique for bulk structural studies due to its large penetration depth. In thin film applications, it is still able to provide useful structure information on the films, since the structures of the films are often different from that of the bulk and therefore the scattering from films and substrates can be separated. Furthermore, because the actual penetration depth or extinction distance depends on the scattering angle, depth profiles are possible to achieve by analysing the details of the scattering profiles. Meanwhile, the scattering profiles also contain information on sample asymmetry which are frequently related to film thickness and perfection. The other way to achieve surface-sensitive x-ray scattering is by using grazing incident geometry to limit the active volume to the near-surface area. Many techniques which employ both elastic and inelastic x-ray scattering were developed to reveal the surface, interface and thin film structure.

Grazing-Incidence X-ray Reflectivity (GIXR)

One of the most powerful x-ray techniques to study the surface and interface morphology is that of grazing incidence x-ray reflectivity (GIXR)[33,34]. By measuring the reflectivity profiles near the surface total-reflection critical angle, the electron density distribution along the surface normal direction can be revealed. Because GIXR is effectively measuring the diffraction pattern of the zeroth order Bragg reflection, this is not affected by the crystallographic structure. Instead, the variation of the electron density near the surface and interface is probed by the GIXR technique. The resolution obtainable with GIXR of roughness and thickness is between 0.1 to 1Å. However, because of its small scattering angle, and absorption of the specimen, GIXR is not as sensitive to the deep buried interface as the surface. In addition studies of the diffuse scattering away from the specular reflectivity streak provide information on the lateral correlation of the roughness, for both the surface and buried interface. Further details of the GIXR technique can be found in Chapter 4.

Reciprocal Space Mapping (RSM)

Within the kinematical approximation, the diffraction pattern is simply the Fourier transform of the electron density distribution of the crystalline sample. By driving a "probe" of the x-ray diffraction within reciprocal space, a diffraction intensity distribution map can be made. The maps are known as reciprocal space maps (RSM)[35,36]. By using high-resolution x-ray diffraction, two-dimensional (or three-dimensional) diffraction patterns can be collected to reveal the "true" lattice structure. Further details of RSM techniques can be found in Chapters 3 and 5.

Crystal-Truncation-Rods (CTR)

For crystalline materials, because of the existence of crystal "terminations", the surface and interface, the symmetry along the surface normal direction is broken and, consequently, the diffraction intensity profiles behave like a "rod" perpendicular to the specimen surface in reciprocal space[37,38]. This phenomenon is known as the

crystal-truncation-rod (CTR). The principles of the CTR can be understood within kinematical theory, where the Fourier transform of a semi-infinite crystal shows delta-functions in surface parallel directions and q^{-2} decay tails at surface perpendicular directions. When there is roughness on the surface or interface, Debye-Waller-like factors associated with the root-mean-square roughness will appear in the reflectivity and the CTR falls off more rapidly. On the other hand, when the thickness of the crystal is finite, interference fringes will appear in the CTR profiles, known as Laue finite size fringes or crystal-truncation-rod interference fringes. The thickness of the film can be calculated directly by the frequency of these fringes. Combining CTR measurements with conventional x-ray measurements such as θ-2θ scans and rocking curves, the thin film structure including the surface and interface roughness can be revealed. More details about CTR can be found in Chapter 6.

Grazing Incidence X-ray Diffraction (GIXD)

In order to explore the surface or near surface crystallographic structure, the scattering from bulk has to be minimised. To achieve this reduction, grazing incidence x-ray diffraction (GIXD) is employed[39,40]. The GIXD technique studies the surface Bragg reflections by limiting the incident or scattering grazing angles below, or close to, the surface total reflection critical angles. As a result, the penetration depth is minimised and the bulk is "unobserved" by x-rays. Therefore, GIXD is rendered surface sensitive. The depth probed by GIXD is normally less than 100Å. Depth profiles of GIXD are possible by varying the grazing angle. Since the scattering vectors of the GIXD are in the plane of the surface and the interatomic separations of the surface layer are measured. GIXD is widely employed in exploring the surface reconstruction phenomena.[41]

X-ray Fluorescence (XRF)

When a specimen is irradiated by an x-ray beam, fluorescent x-rays are emitted[33,42,43]. The spectrum of the fluorescent x-rays can be analysed by a spectrometer or an energy dispersive detector[11]. By identifying the wavelength of the fluoresce peaks, the chemical composition of the film can be determined. The peak

intensities of the fluorescent spectrum provide the quantitative information on the specific composition. Although XRF is mainly a surface-insensitive technique, it is still successfully used in determining the composition of single-layer or multilayer films. The thicknesses of the layers are possible to obtain from XRF measurement by considering the absorption of the x-ray as well as the active volume of a specific composition. The total-reflection x-ray fluorescence (TXRF) is a variation of XRF, by limiting the incident and scattered x-rays below the surface total reflection critical angle. In this geometry, almost all the fluorescence comes from the near-surface region (about 1 – 5 nm) rather than ~ 10μm in normal XRF. Because XRF is not related to the crystal structure, it is not possible to obtain crystallographic parameters. Furthermore, the analyses of the XRF spectrum will be complex if the compositions of two or more layers are the same. In conclusion, the structural information obtainable on thin film specimens revealed from XRF measurements is limited.

X-ray Standing Waves (XSW)

According to the dynamical scattering theory, when x-ray diffraction occurs, interference wave fields are established in the crystal as standing waves[44,45,46]. The movement of the interference wave fields is a function of the reflection angle. By measuring the inelastic scattering from a crystal excited by the interference wave, the real-space position relationship between the standing waves and the atoms can be revealed. Because XSW consists of information from both elastic and inelastic scattering, both the atomic positional parameters and the composition of the samples can be determined. Since the availability of synchrotron x-ray and ultra-high-vacuum for high-quality film growth, XSW has become one of the best surface analysis techniques. Because of the large penetration depth of x-rays, it is also possible to obtain information on buried interfaces. The best resolution of XSW is about 10^{-2}Å. However, the technique finds only limited applications. Firstly, because the dynamical effects are important only for highly perfect single crystals and strong Bragg reflections, XSW is not a generally applicable technique. Secondly, because XSW occurs near Bragg reflections, periodicities larger than the unit cell can not be

observed. The details of atomic structures at the $YBa_2Cu_3O_x$ thin film interface were reported by employing the XSW technique[47].

1.3 Outline of the thesis

The aim of this thesis is to demonstrate the ability of high-resolution x-ray scattering for examining surface, interface, and thin film structures. In particular important new information has been found for the surface and interface structure of some semiconducting and superconducting materials.

In Chapter 2, the elementary theories of x-ray scattering are briefly reviewed. It starts from kinematical scattering theory, which assumes that the interaction between x-ray photons and samples is weak. Therefore, multiple scattering and dispersion are neglected. The kinematical approximation is justified in most cases, except the scattering from large, perfect single crystals. In these exceptions, x-rays strongly interact with samples when the Bragg conditions are satisfied. The scattering can only be explained by the use of dynamical theories which will also be reviewed in Chapter 2.

Chapter 3 covers the various aspects of the experimental techniques which are essential in performing x-ray scattering experiments. The principles of x-ray generators, both conventional x-ray and synchrotron radiation sources, are presented. The structure of diffractometers, which were used to perform the experiments, is also discussed in detail. The effects of resolution from optical elements of the diffractometer, such as monochromator, analyser or x-ray source dispersion, will be presented qualitatively. Finally, various operations of the diffractometer recognised as different scan modes will be demonstrated. The information revealed by the scans will also be explained.

The surface and buried interface morphology of Si_xGe_{1-x} single quantum-well thin films grown with and without antimony as surfactant were studied, and is presented in Chapter 4. Grazing incidence x-ray reflectivities were used to explore the surface and interface roughness structures. It was found that the existence of a surfactant

improves both the surface and interface quality. These improvements include the smaller root-mean-square roughness and the longer roughness correlation length. Furthermore, the surfactants also enhance the vertical correlation between interfaces. As a result, the roughness of the substrate surface is replicated to interfaces between layers.

Chapter 5 presents studies of $YBa_2Cu_3O_7$ high temperature oxide thin film superconductors grown on $LaAlO_3$ or $SrTiO_3$ substrates. Samples from various sources using different deposition techniques were examined using high-resolution x-ray scattering. Traditional scans such as rocking curves and θ-2θ scans were used to quantify the quality of the samples. With the help of two-dimensional reciprocal space mapping, the microscopic crystal structures of the $YBa_2Cu_3O_7$ thin film samples were determined.

The $YBa_2Cu_3O_7$ thin film grown on the $SrTiO_3$ substrate by laser ablation was found to have much more complex structure and more detailed studies are presented in Chapter 6. It was found that the $YBa_2Cu_3O_7$ thin film starts from a thin layer of mosaic epitaxial film on the substrate surface which is slightly mis-cut. Then, an ultra-high-quality single crystal film forms along surface normal direction with horizontal coherence length exceeding tens μm and coherent over whole thickness. Some small mosaic grains with size of ~100Å are randomly distributed within the ultra-high-quality film. Due to the disorder at the interface, the Bragg reflections of the single crystal $YBa_2Cu_3O_7$ film can only be observed in particular cases. The existence of the ultra-high-quality film has never been reported in numerous studies in the literature.

---

[1] R.Feidenhans'l, Surface Science Reports **10**, 105 (1989)

[2] A.B.Hinder, Thin Solid Films **77**, 272 (1981)

[3] J.Mannhart, P.Chaudhari, D.Dimos, C.C.Tsuei, and T.R.McGuire, Phys. Rev. Lett. **61**, 2476 (1988)

[4] M.P.Siegal, J.M.Phillips, A.F.Hebard, R.B.van Dover, R.C.Farrow, T.H.Tiefel, and J.H.Marshall, J. Appl. Phys. **70**, 4982 (1991)

[5] R.Ramesh, A.Inam, T.Sands, and C.T.Rogers, Mater. Sci. Eng. B **14**, 188 (1992)

[6] Y.H.Li, C.Leach, Y.Li, J.A.Kilner, D.Lacey, A.D.Caplin, and R.E.Somekh, J. Mater. Sci. **30**, 3968 (1995)

[7] P.F.Fewster, Rep. Prog. Phys **59**, 1339 (1996)

[8] H.J.Laidler, Mag. Mag. Mat. **154**, 165 (1996)

[9] A.Fert, Physics World, Nov., 34 (1994)

[10] A.Neminsky, J.Dumas, B.P.Thrane, C.Schlenker, H.Karl, and B.Stritzker, Phys. Rev. B **50**, 3307 (1994)

[11] C.R.Brundle, C.A.Evans, Jr., and S.Wilson, *Encyclopedia of Materials Characterization: Surfaces, Interfaces, Thin Films* (Butterworth-Heinemann, 1992)

[12] H.Luth, *Surfaces and Interfaces of Solid Materials* (Springer, 1995)

[13] A.H.Carim, S.N.Basu, and R.E.Muenchausen, Appl. Phys. Lett. **58**, 871 (1991)

[14] A.C.Westerhiem, P.C.Mcintyre, S.N.Basu, D.Bhatt, L.S.Yu-Jahnes, A.C.Anderson, and M.J.Cima, J. Elect. Mater. **22**, 1113 (1993)

[15] D.Bhatt, S.N.Basu, A.C.Westerhiem, and A.C.Anderson, Physica C **222**, 283 (1994)

[16] H.W.Zandbergen, J.G.Wen, C.Traeholt, and V.Svetchnikov, J. Alloy Comp. **195**, 85 (1993)

[17] C.Traeholt, J.G.Wen, V.Svetchnikov, and H.W.Zandbergen, Physica C **230**, 297 (1994)

[18] L.P.Guo, Y.J.Tain, J.Z.Liu, S.F.Xu, L.Li, Z.X.Zhao, Z.H.Chen, D.F.Cui, H.B.Lu, Y.L.Zhou, ang G.Z.Yang, Appl. Phys. Lett. **66**, 3356 (1995)

[19] H.Klapper, "*X-ray Diffraction Topography: Principles and Techniques*", in *X-ray and Neutron Dynamical Diffraction: Theory and Applications*, edit by A.Authier, S.Lagomarsino, and B.K.Tanner (Plenum Press, 1996)

[20] L.H.Schwartz, and J.B.Cohen, *Diffraction from Materials* (Springer-Verlag, 1987)

[21] H.K.Wickramasinghe, Scitific American, Oct., 74 (1989)

[22] J.R.Hook, and H.E.Hall, *Solid State Physics* (John Wiley and Sons, 1991)

[23] G.Binnig, H.Rohrer, C.Gerber, and E.Weibel, Appl. Phys. Lett. **40**, 178 (1982); Phys. Rev. Lett., **50**, 120 (1983)

[24] C.Gerber, D.Anselmetti, J.G.Bednorz, J.Mannhart, and D.G.Schlom, Nature **350**, 279 (1991)

[25] M.Hawley, I.D.Raistrick, J.G.Beery, and R.J.Houlton, Science **251**, 1587 (1991)

[26] X.Y.Zheng, D.H.Lowndes, S.Zhu, J.D.Budai, and R.J.Warmack, Phys. Rev. B **45**, 7584 (1992)

[27] K.Hirata, F.Baudenbacher, and H.Kinder, Physica C **214**, 272 (1993)

[28] Q.D.Jiang, D.M.Smilgies, R.Feidenhans'l, M.Cardona, and J.Zegenhagen, Solid State Comm. **98**, 157 (1996)

[29] C.Kittel, *Introduction to Solid State Physics* (John Wiley and Sons, 1986)

[30] C.J.Davisson, L.H.Germer, Nature **119**, 558 (1927); Phys. Rev. **30**, 705 (1927)

[31] T.Terashima, Y.Bando, K.Iijima, K.Yamamoto, K.Hirata, K.Kamigaki, and H.Terauchi, Physica C **162-164**, 615 (1989); Phys. Rev. Lett. **65**, 2684 (1990); J. Appl. Phys. **69**, 3653 (1991)

[32] A.Ichinose, and A.Shirabe, Physica C **277**, 243 (1997)

[33] D.K.G.de Boer, A.J.G.Leenaers, and W.W.van den Hoogenhof, X-ray Spec. **24**, 91 (1995)

[34] I.Pape, Ph.D. Thesis, University of Durham (1997)

[35] P.F.Fewster, Appl. Phys. A **58**, 121 (1994)

[36] P.F.Fewster, *"Reciprocal Space Mapping"*, in *X-ray and Neutron Dynamical Diffraction: Theory and Applications*, edit by A.Authier, S.Lagomarsino, and B.K.Tanner (Plenum Press, 1996)

[37] S.R.Andrews, and R.A.Cowley, J. Phys. C: Solid State Phys., **18**, 6427 (1985)

[38] I.K.Robinson, Phys. Rev. B **33**, 3830 (1986)

[39] W.C.Marra, J. Appl. Phys. **50**, 6927 (1979)

[40] W.C.Marra, Phys. Rev. B **46**, 1081 (1981)

[41] C.A.Lucas, S.C.Dower, D.F.McMorrow, G.C.L.Wong, F.J.Lamelas, and P.H.Fuoss, Phys. Rev. B **47**, 10375 (1993)

[42] B.D.Cullity, *Elements of X-ray Diffraction* (Addison-Wesley, 1978)

[43] A.G.Michette, and C.J.Buckley, *X-ray Science and Technology* (Institute of Physics, 1993)

[44] B.W.Batterman, and H.Cole, Rev. Modern Phys. **36**, 681 (1964)

[45] J.Zegenhagen, Surf. Sci. Rep. **18**, 199 (1993)

[46] J.R.Patel, *"x-ray standing waves"*, in *X-ray and Neutron Dynamical Diffraction: Theory and Applications*, edit by A.Authier, S.Lagomarsino, and B.K.Tanner (Plenum Press, 1996)

[47] J.Zegenhagen, H.U.Habermeier, T.Siegrist, J.R.Patel, E.Fontes, and L.E.Berman, Physica C **185-189**, 2077 (1991); Solid State Comm. **93**, 763 (1995)

Chapter 2

Elementary Theory of X-ray Scattering

2.1 Introduction

Since 1912 when x-ray diffraction was first observed by Laue, Friedrich, Knipping, and Bragg, x-ray scattering has become one of the most powerful and popular techniques to explore the microstructure of materials. One of the most important reasons for this is that x-ray scattering is generally non-destructive. The importance of x-ray scattering is of benefit not only in pure science research but also in many industrial applications.

In this chapter, the fundamental principles of x-ray scattering, both kinematical and dynamical, will be reviewed briefly. The review starts with the kinematical theory which has been successfully applied in describing the scattering by small, imperfect crystals. In this case, the interaction between the x-rays and the crystal is weak. Therefore the single scattering assumption is used and dispersion can be neglected. This review chapter will first discuss the scattering from a single atom and the extension to the calculation of the diffraction pattern. The concept of reciprocal (or wavevector) space and the relationship between x-ray diffraction and Fourier transforms will be also developed.

Furthermore, the development of the dynamical theory for the scattering from highly perfect crystals will also be explained. It mainly follows the Ewald-von Laue treatment. The interaction between the x-rays and the samples is the major difference

between kinematical theory and dynamical theory. This review will first discuss the allowed wave vector of the crystal and the dispersion surface. To link the x-rays propagating inside the crystal and the x-rays observed outside the crystal, boundary conditions have to be considered. Two different approximations will be illustrated to show how dynamical diffraction theory works. These are, the one-wave approximation, for the case where no diffraction is excited and secondly, the two-wave approximation, for the case that only one diffracted wave is excited and interferes with the incident wave inside the crystal. Finally, the differences between kinematical theory and dynamical theory will be summarised.

Further details about the both kinematical and dynamical theories can be found in many references[1,2,3,4,5].

2.2 Kinematical theory

2.2.1 Scattering of x-rays by an atom and the atomic form factor

In kinematical theory, the central assumption is that of single scattering, which means that every x-ray photon only interacts with the sample crystal once. The coherent scattering from different scattering centres gives rise to interference causing the observed diffraction. We start our derivation with the scattering from a single atom.

Consider a plane x-ray wave with wave vector $\vec{k}_i$ ($|\vec{k}| \equiv 2\pi/\lambda$, where λ is the wavelength) incident upon an atom located at $\vec{r}$

$$E = E_0 e^{i(\omega t - \vec{k}_i \cdot \vec{r})} \tag{2.1}$$

If the electron density of the atom is $\rho(\vec{r})$, then the electric field amplitude of the scattered x-ray at a distance R from the atom is

$$E(\vec{q},\vec{r}) = E_0 \frac{e^2}{mc^2}\frac{1}{R}\int e^{i\vec{q}\cdot(\vec{r}+\vec{r}')}\rho(\vec{r}')d\vec{r}' \tag{2.2}$$

where the factor $\frac{e^2}{mc^2}$ is known as the *classical electron radius*, which has the value of 2.817×10^{-15} m. The momentum transfer vector, $\vec{q}$, is defined as $\vec{q} = \vec{k}_f - \vec{k}_i$, whilst the *atomic form factor*, $f(q)$, is defined as the Fourier transform of the electron density of a single atom

$$f(q) = \int_{atom} \rho(\vec{r}) e^{i\vec{q}\cdot\vec{r}} d\vec{r} \tag{2.3}$$

Figure 2.1 shows the vector relationship between the incident wave, the scattered wave, and the momentum transfer vector involved in x-ray scattering.

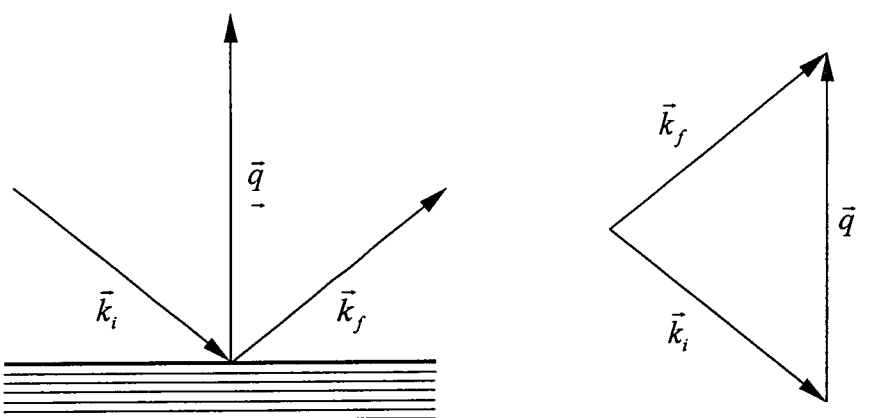

Figure 2.1 The vector relationship between the incident wave ($\vec{k}_i$), the scattered wave ($\vec{k}_f$) and the resulting momentum transfer vector ($\vec{q}$) involved in x-ray scattering where $\vec{q} = \vec{k}_f - \vec{k}_i$

By substituting Equation (2.3) into Equation (2.2) we can obtain

$$E(\vec{q},\vec{r}) = E_0 \frac{e^2}{mc^2} \frac{1}{R} f(q) e^{i\vec{q}\cdot\vec{r}} \tag{2.4}$$

By neglecting the constant factors, we can define the *scattering amplitude*, $A(\vec{q})$ as

$$A(\vec{q}) = f(q) e^{i\vec{q}\cdot\vec{r}} \tag{2.5}$$

The above calculation of the atomic form factors is based upon the assumption that the wavelength of the x-ray used is much shorter than the absorption edge wavelength of the atom. Under this assumption, the electrons of an atom are treated as classical free electrons. However, the scattering power of a bound electron is different from the scattering power of the free electron. Furthermore, the scattering usually involves a phase shift. In practice, the atomic form factors should be of a complex form and thus

$$f = f^0 + \Delta f' + i\Delta f'' \tag{2.6}$$

where $\Delta f'$ and $\Delta f''$ are the real and imaginary parts of the dispersion correction. However, when the wavelength of the x-ray is much shorter than the absorption edges, $\Delta f'$ and $\Delta f''$ are very small and hence negligible. The approximate values of f^0, $\Delta f'$ and $\Delta f''$ for different elements can be found tabulated in the *International Tables for X-ray Crystallography*[6].

2.2.2 Scattering of x-rays by a unit cell and the structure factor

X-rays scattered from different atoms within a crystal interfere with each other and thus diffraction occurs. For a crystal, which has a periodic structure, the first step in calculating the diffraction pattern is to consider the diffraction from a single unit cell, the building block of the crystal structure.

Under the single scattering assumption, the scattering amplitude of a crystal can be obtained by summing up the scattering amplitudes of all the atoms embedded in it. Because of the periodicity, Equation (2.5) can be written as

$$\begin{aligned} A(\vec{q}) &= \sum f(q) e^{i\vec{q}\cdot\vec{r}} \\ &= \sum_n \sum_j f_j(q) e^{i\vec{q}\cdot(\vec{R}_n + \vec{r}_j)} \\ &= \sum_n F(\vec{q}) e^{i\vec{q}\cdot\vec{R}_n} \end{aligned} \tag{2.7}$$

Here, $f_j(q)$ is the atomic form factor of the j-th atom in a unit cell. $\vec{R}_n$ is the position vector of the unit cell containing the atom and $\vec{r}_j$ is the position vector of the atom from the origin of the unit cell. The scattering amplitude of a unit cell, $F(\vec{q})$, is known as the *structure factor* and is defined as

$$F(\vec{q}) = \sum_j f_j(q) e^{i\vec{q}\cdot\vec{r}_j} \tag{2.8}$$

Thus,

$$\begin{aligned} A(\vec{q}) &= \sum_n F(\vec{q}) e^{i\vec{q}\cdot\vec{R}_n} \\ &= F(\vec{q}) \sum_n e^{i\vec{q}\cdot\vec{R}_n} \end{aligned} \tag{2.9}$$

The second term, $\sum_n e^{i\vec{q}\cdot\vec{R}_n}$, depends only upon the "distribution" of the unit cells in the crystal or the shape of the crystal, which will be discussed in the next section.

2.2.3 3D diffraction pattern of a crystal and reciprocal space

Consider the case of a crystal with the shape of a parallelepiped with edges N_1a_1, N_2a_2 and N_3a_3 where a_1, a_2, a_3 are the lattice parameters. From Equation (2.7), the scattering amplitude of this crystal can be written as

$$\begin{aligned} A(\vec{q}) &= \sum_n F(\vec{q}) e^{i\vec{q}\cdot\vec{R}_n} \\ &= F(\vec{q}) \sum_{n_1=0}^{N_1-1} \sum_{n_2=0}^{N_2-1} \sum_{n_3=0}^{N_3-1} e^{i\vec{q}\cdot(n_1\vec{a}_1+n_2\vec{a}_2+n_3\vec{a}_3)} \end{aligned} \tag{2.10}$$

A function $S_N(x)$ can be defined as

$$\begin{aligned} S_N(x) &= \sum_{n=0}^{N-1} e^{ixn} \\ &= \frac{1-e^{ixN}}{1-e^{ix}} \end{aligned} \tag{2.11}$$

The squared modulus of S_N is

$$|S_N(x)|^2 = \frac{\sin^2(Nx/2)}{\sin^2(x/2)} \tag{2.12}$$

Equation (2.10) then becomes

$$A(\vec{q}) = F(\vec{q})S_{N_1}(\vec{q}\cdot\vec{a}_1)S_{N_2}(\vec{q}\cdot\vec{a}_2)S_{N_3}(\vec{q}\cdot\vec{a}_3) \tag{2.13}$$

The diffraction intensity is proportional to the square modulus of the scattering amplitude and thus

$$\begin{aligned} I &= I_e|F(\vec{q})|^2\left|S_{N_1}(\vec{q}\cdot\vec{a}_1)\right|^2\left|S_{N_2}(\vec{q}\cdot\vec{a}_2)\right|^2\left|S_{N_3}(\vec{q}\cdot\vec{a}_3)\right|^2 \\ &= I_e|F|^2\frac{\sin^2\left(\frac{N_1(\vec{q}\cdot\vec{a}_1)}{2}\right)}{\sin^2\left(\frac{\vec{q}\cdot\vec{a}_1}{2}\right)}\frac{\sin^2\left(\frac{N_2(\vec{q}\cdot\vec{a}_2)}{2}\right)}{\sin^2\left(\frac{\vec{q}\cdot\vec{a}_2}{2}\right)}\frac{\sin^2\left(\frac{N_3(\vec{q}\cdot\vec{a}_3)}{2}\right)}{\sin^2\left(\frac{\vec{q}\cdot\vec{a}_3}{2}\right)} \end{aligned} \tag{2.14}$$

where

$$I_e = I_0\left(\frac{e^2}{mc^2}\right)^2\frac{1}{R^2}\left(\frac{1+\cos^2 2\theta}{2}\right) \tag{2.15}$$

When N approaches infinity, the diffraction intensity is negligible everywhere except when $\vec{q}\cdot\vec{a}$ is equal to zero or 2π times any integer.

$$\begin{aligned} \vec{q}\cdot\vec{a}_1 &= 2\pi h \\ \vec{q}\cdot\vec{a}_2 &= 2\pi k \\ \vec{q}\cdot\vec{a}_3 &= 2\pi l \end{aligned} \tag{2.16}$$

Here h, k and l are called the *Miller indices*. Equation (2.16) is known as the Laue condition, which is equivalent to the Bragg equation

$$2d\sin\theta = n\lambda \tag{2.17}$$

Let

$$\vec{q} = h\vec{b}_1 + k\vec{b}_2 + l\vec{b}_3 \tag{2.18}$$

where

$$\begin{aligned}
\vec{b}_1 &= 2\pi \frac{\vec{a}_2 \times \vec{a}_3}{\vec{a}_1 \cdot \vec{a}_2 \times \vec{a}_3} \\
\vec{b}_2 &= 2\pi \frac{\vec{a}_3 \times \vec{a}_1}{\vec{a}_1 \cdot \vec{a}_2 \times \vec{a}_3} \\
\vec{b}_3 &= 2\pi \frac{\vec{a}_1 \times \vec{a}_2}{\vec{a}_1 \cdot \vec{a}_2 \times \vec{a}_3}
\end{aligned} \tag{2.19}$$

From Equation (2.18), it is clear that $\vec{q}$ is the linear combination of vectors $\vec{b}_1$, $\vec{b}_2$ and $\vec{b}_3$. Mathematically, we can define a vector space[7], q-space, by using $\vec{b}_1$, $\vec{b}_2$ and $\vec{b}_3$ as the bases of the space. In other words, $\vec{b}_1$, $\vec{b}_2$ and $\vec{b}_3$ *span* the q-space. The integer h, k and l define a lattice system called the *reciprocal lattice* in q-space, which represents the solutions for the Laue condition or the three-dimensional Bragg equations. This q-space is commonly referred to as *reciprocal space*.

Figure 2.2 shows the *Ewald construction* of x-ray scattering in reciprocal space. s_o/λ is the wave vector of an incident x-ray which points to the origin of reciprocal space, O. A sphere of radius $1/\lambda$ centred at the initial end of s_o/λ, C, can be drawn. Whenever the surface of the sphere passes through any lattice point, the Laue conditions are fulfilled and scattering will be observed from that position. The wave vector of the diffracted beam, s/λ, is also predicted. This sphere is known as the sphere of reflection or *Ewald sphere*. The Ewald sphere is the graphical representation of the Laue conditions in reciprocal space, which is directly related to the geometry of the scattering. On the other hand, the reciprocal lattice represents the crystal structure in reciprocal space. Whenever they crossover at a point, a solution for both conditions is found and scattering is observed.

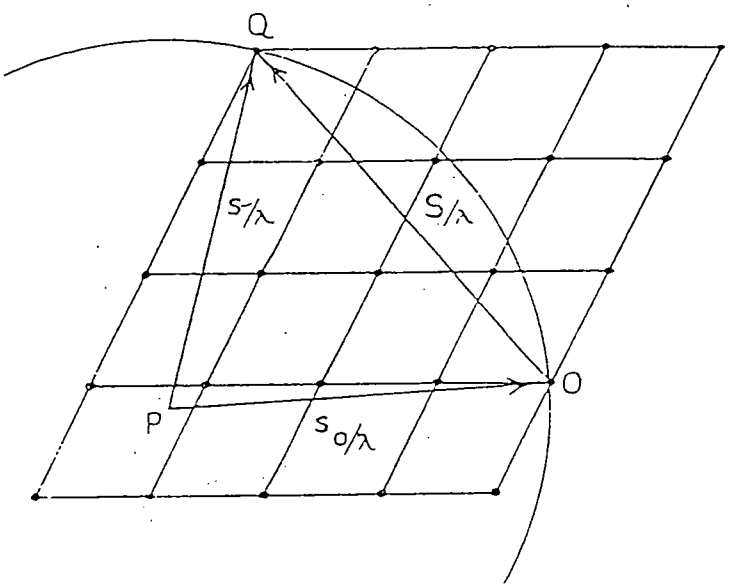

Figure 2.2 The Ewald construction of x-ray scattering in reciprocal space.

From Equation (2.14) it is clear that the diffraction intensity has a non-zero value at non-integer h, k and l, when N_1, N_2 and N_3 are less than infinite. In other words, the diffraction intensity is no longer only defined on the reciprocal lattice but also all over reciprocal space. The intensity distribution around a certain reciprocal lattice point is dependent upon N, which is related to the size and the shape of the crystal.

Consider the squared modulus of S_N in the case in which N approaches infinity

$$\begin{aligned} \left|S_N(\vec{q}\cdot\vec{a})\right|^2 &= \frac{\sin^2\left[\frac{N(\vec{q}\cdot\vec{a})}{2}\right]}{\sin^2\left[\frac{\vec{q}\cdot\vec{a}}{2}\right]} = \frac{\sin^2\left[\frac{N(\vec{q}'\cdot\vec{a})}{2}\right]}{\sin^2\left[\frac{\vec{q}'\cdot\vec{a}}{2}\right]} \\ &\approx N^2 \exp\left[-\frac{N^2(\vec{q}'\cdot\vec{a})^2}{\pi}\right] \end{aligned} \tag{2.20}$$

Here, $\vec{q}'$ is the vector difference from the nearest reciprocal lattice point,

$$\vec{q}' = \vec{q} - \left(h\vec{b}_1 + k\vec{b}_2 + l\vec{b}_3\right) \tag{2.21}$$

When $\vec{q}'$ is sufficiently small, the modulus of the square of the sine function can be approximated to a Gaussian function with the same maximum position and the same integral area. With such an approximation, it can be shown that the width of the diffracted intensity distribution is

$$B_{2\theta} = \frac{\lambda}{Na\cos\theta} = \frac{\lambda}{L\cos\theta} \tag{2.22}$$

A more exact treatment gives

$$B_{2\theta} = \frac{0.94\lambda}{L\cos\theta} \tag{2.23}$$

where $B_{2\theta}$ is the full width of the reflection in radians and L (= Na) is the average crystal grain size. Equation (2.23) is known as the Scherrer formula[5]. The constant in the equation is strongly depend on the distribution of the grain size and shape and, generally, varies from 0.89 to 0.94. The Scherrer formula allows the calculation of the dimensions of the crystallographically coherent grains from the width of a Bragg reflection. Thus, it is often used as a measurement of crystal quality.

Since the Bragg reflections have finite width, it is clear that the maximum intensity from (2.14) is

$$I_{\max} = I_e |F|^2 N_1^2 N_2^2 N_3^2 \tag{2.24}$$

By rotating a crystal at a constant speed while measuring the reflected intensity, the total energy of the reflection can be measured.

$$E = \frac{P_0}{\omega}\frac{N^2\lambda^3}{2\mu}|F|^2\left(\frac{e^2}{mc^2}\right)^2\left(\frac{1+\cos^2 2\theta}{2\sin 2\theta}\right) \tag{2.25}$$

where, ω is the angular speed of the crystal, $P_0 = I_0 A_0$ is the power of the primary beam, $N = N_1 N_2 N_3$ is the number of the unit cells in the crystal and μ is the linear absorption coefficient.

2.2.4 Diffraction and th e Fourier transform

The complete structure of crystalline materials can be described by the electron density distribution function in space, $\rho(\vec{r})$. Therefore, the scattering amplitude according to Equation (2.3) can be generalised to

$$A(\vec{q}) = \int \rho(\vec{r}) e^{i\vec{q}\cdot\vec{r}} d\vec{r} \tag{2.26}$$

Here, $\rho(\vec{r})$ is the electron density distribution of the whole crystal and the integral is taken over all space. It is clearly that the calculation of the scattering amplitude is exactly the *Fourier transform* of the electron density distribution. The result follows that the inverse Fourier transform is applicable.

$$\rho(\vec{r}) = \int A(\vec{q}) e^{-i\vec{q}\cdot\vec{r}} d\vec{q} \tag{2.27}$$

As can be seen, by simply applying the inverse Fourier transform on the scattering amplitude, the electron density distribution function or the structure of the crystal can be solved. However, the scattering amplitude is a complex function and cannot be measured in an experiment directly. Instead, the intensity distribution, the square modulus of the scattering amplitude, is a measurable physical quantity. Because the scattering intensity does not contain the phase information, it is impossible to solve the crystal structure directly. This is known as the *crystallographic phase problem*[8].

If $\rho_u(\vec{r})$ is the electron density distribution within the unit cell located at the origin, the electron density distribution of the unit cell at $\vec{R}$ will be $\rho_u(\vec{r}+\vec{R})$. Now let us consider the scattering amplitude of a crystal. The electron density distribution of the whole crystal is

$$\begin{aligned} \rho(\vec{r}) &= \sum_{\vec{R}} \rho_u(\vec{r}+\vec{R}) \\ &= \sum_{n_1=0}^{N_1-1}\sum_{n_2=0}^{N_2-1}\sum_{n_3=0}^{N_3-1} \rho_u(\vec{r}+n_1\vec{a}_1+n_2\vec{a}_2+n_3\vec{a}_3) \end{aligned} \tag{2.28}$$

The scattering amplitude is the Fourier transform of the electron density distribution

$$
\begin{aligned}
A(\vec{q}) &= \int \rho(\vec{r}) e^{i\vec{q}\cdot\vec{r}} d\vec{r} \\
&= \int \sum_{n_1=0}^{N_1-1} \sum_{n_2=0}^{N_2-1} \sum_{n_3=0}^{N_3-1} \rho_u(\vec{r} + n_1\vec{a}_1 + n_2\vec{a}_2 + n_3\vec{a}_3) e^{i\vec{q}\cdot\vec{r}} d\vec{r} \\
&= \sum_{n_1=0}^{N_1-1} \sum_{n_2=0}^{N_2-1} \sum_{n_3=0}^{N_3-1} \int \rho_u(\vec{r} + n_1\vec{a}_1 + n_2\vec{a}_2 + n_3\vec{a}_3) e^{i\vec{q}\cdot\vec{r}} d\vec{r} \\
&= \int \rho_u(\vec{r}) e^{i\vec{q}\cdot\vec{r}} d\vec{r} \sum_{n_1=0}^{N_1-1} \sum_{n_2=0}^{N_2-1} \sum_{n_3=0}^{N_3-1} e^{i\vec{q}\cdot(n_1\vec{a}_1 + n_2\vec{a}_2 + n_3\vec{a}_3)} \\
&= F(\vec{q}) \sum_{n_1=0}^{N_1-1} \sum_{n_2=0}^{N_2-1} \sum_{n_3=0}^{N_3-1} e^{i\vec{q}\cdot(n_1\vec{a}_1 + n_2\vec{a}_2 + n_3\vec{a}_3)} \\
&= F(\vec{q}) G_a G_b G_c
\end{aligned}
\tag{2.29}
$$

The last result is identical to the result of Equation (2.9)

According to the *shift theorem*[9] of the Fourier transform, G_a, G_b and G_c can be written as

$$
\begin{aligned}
G_a &= \sum_{n_1=0}^{N_1-1} e^{i\vec{q}\cdot n_1\vec{a}_1} = \int \sum_{n_1=0}^{N_1-1} \delta(\vec{r} - n_1\vec{a}) e^{i\vec{q}\cdot\vec{r}} d\vec{r} \\
G_b &= \sum_{n_2=0}^{N_2-1} e^{i\vec{q}\cdot n_2\vec{a}_2} = \int \sum_{n_2=0}^{N_2-1} \delta(\vec{r} - n_2\vec{a}) e^{i\vec{q}\cdot\vec{r}} d\vec{r} \\
G_c &= \sum_{n_3=0}^{N_3-1} e^{i\vec{q}\cdot n_3\vec{a}_3} = \int \sum_{n_3=0}^{N_3-1} \delta(\vec{r} - n_3\vec{a}) e^{i\vec{q}\cdot\vec{r}} d\vec{r}
\end{aligned}
\tag{2.30}
$$

It is clear that G_a, G_b and G_c are the Fourier transforms of the crystal lattice and only relate to the size and the shape of the crystal.

In most cases, the effective scattering volume of the crystal in x and y directions is limited by the coherence length of the x-ray source, the size over which the x-ray radiation field is coherent. This coherence length varies with the x-ray source and is often on the order of microns. The number of unit cells in the x and y directions, N_1 and N_2 respectively, are very large. Therefore, G_a and G_b is the reciprocal lattice with δ-functions at every lattice point along the x and y directions. The peak width of the reflections along the x and y directions are virtually dominated by the instrument

resolution function[10]. However, it is generally not the case in the z direction. The existence of the surface termination of the sample breaks the symmetry.

$$G_c = \sum_{n_3=0}^{N_3-1} e^{i\vec{q}\cdot n_3\vec{a}_3} = \frac{1-e^{i\vec{q}\cdot N_3\vec{a}_3}}{1-e^{i\vec{q}\cdot\vec{a}_3}} \approx \frac{1}{1-e^{i\vec{q}\cdot\vec{a}_3}} \approx \frac{1}{i\vec{q}'\cdot\vec{a}_3} \tag{2.31}$$

Here, we assume that N_3 is very large and the scattering concerned is very close to a reciprocal lattice point. Therefore,

$$I \propto |G_c|^2 \propto \frac{1}{(q')^2} \tag{2.32}$$

The scattering profile in the z direction is not a δ-function. Instead, $(q')^2$ tails can be found on either side of the reflection. It is clear that the diffraction shows a rod-shape in three-dimensional reciprocal space. This phenomenon is known as the *crystal truncation rod*[11,12,13].

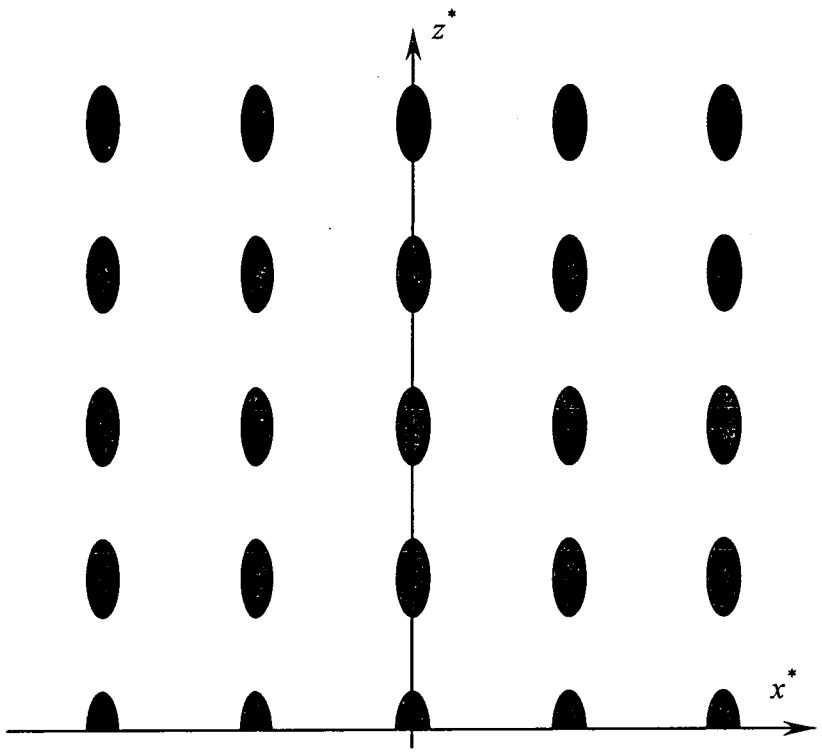

Figure 2.3 The crystal truncation rods in reciprocal space.

For a thin crystal, N_3 is finite and finite size oscillations will occur.

$$I \propto |G_c|^2 = \frac{\sin^2\left[\frac{N(\vec{q}' \cdot \vec{a})}{2}\right]}{\sin^2\left[\frac{\vec{q}' \cdot \vec{a}}{2}\right]} \tag{2.33}$$

The oscillation frequency is directly related to the thickness of the crystal. Further discussion of this will be delayed until Chapter 6.

2.3 Dynamical theory

2.3.1 An introduction to the dynamical scattering theories

The derivation of the scattering theory, so far, has been based upon the assumption that the interaction between the x-rays and the crystal is sufficiently weak. In this case, the primary x-ray beam passes through the crystal with the velocity of light in

free space, c, without any loss of intensity, and is scattered by the scattering centres just once. The scattering theory based on this kinematical approximation is justified as long as we are considering small crystals and weak reflections. However, for large and highly perfect crystals, kinematical theory is not able to explain the scattering intensity profiles. Because the summation is over all scattered radiation from individual scattering centres, the scattering amplitude diverges to infinity at strong Bragg reflections for large perfect crystals. This is unphysical. The high reflectivity also leads to considerable multiple reflections which satisfy the Laue condition simultaneously. This is at variance with one of the assumptions of the kinematical theory. Furthermore, considering the scattering mechanism, there will be dispersion phenomena because the scattered x-rays have phase differences compared to the primary beam and they will interfere with each other within the material. All the above reasons require a more rigorous theory, *dynamical theory*.

The dynamical theory was first introduced by Darwin in 1914[14]. Meanwhile, a completely different but more general approach was presented independently by Ewald in 1916-1917[15] and reformulated by von Laue in 1931[16]. In this section, a brief review of the Ewald-von Laue treatment will be performed.

The basic idea of the dynamical theory is that the interaction between the x-ray and the material is no longer negligible. Therefore, it is important first to find out the possible electromagnetic waves (x-rays) which are allowed propagation throughout the crystal. According to von Laue's theory, the lattice point of the crystal is considered to be occupied by an electric dipole which can be excited and set into oscillation by the radiation field of any electromagnetic wave passing through the crystal. As the electric dipole oscillates, another photon will be emitted. The original radiation and the scattered radiation will interact with each other and a new radiation field is formed. Because of the periodicity, only some of the new radiation fields can reach the resonance and propagate within the crystal. These are the allowed waves within the crystal. In other words, the whole system must be dynamically self-contained. The possible solutions of x-rays propagating inside the crystal form a continuous surface in reciprocal space. This is called the *dispersion surface*. After

determining the dispersion surface, the x-rays travelling inside and outside the crystal can be identified by matching the surface boundary conditions and the dispersion surface.

2.3.2 Allowed wave vectors within the crystal

One of the most important concepts in dynamical theory is the dispersion effect. Because the scattering process occurs inside crystal, the interaction between x-rays and the crystal plays an important role in the process. The x-rays with different frequencies will have different speeds when they pass through the crystal and, therefore, dispersion occurs. The first step in understanding dynamical theory is to find out the allowed wave vectors with the same frequencies within the crystal.

The dielectric constant of a crystal can be written as

$$\eta = 1 - \frac{e}{\pi m \nu^2}\rho \tag{2.34}$$

where e is the electric charge, m is the electron mass, ν is the frequency of the x-ray and ρ is the electron density distribution of the crystal. The second term in Equation (2.33), $\left(\frac{e}{\pi m \nu^2}\rho\right)$ is of the order of 10^{-6}. So η is just slightly less than unity.

Let $\vec{E}$ and $\vec{D}$ be the vectors representing the electric field and the electric displacement, so

$$\vec{D} = \eta\vec{E} \tag{2.35}$$

The dielectric polarisation, $\vec{P}$, is

$$4\pi\vec{P} = (1-\eta)\vec{E} = \left(1 - \frac{1}{\eta}\right)\vec{D} = \phi\vec{D} \tag{2.36}$$

where ϕ is the polarisability of the medium.

$$\phi = 1 - \frac{1}{\eta} \approx -\frac{e}{\pi m v^2}\rho \tag{2.37}$$

For crystalline materials, because of the inherent periodicity, the polarisability, ϕ, can be expanded as a Fourier series over the reciprocal lattice

$$\phi = \sum_q \phi_q \exp\left[-2\pi i\left(\vec{R}_q \cdot \vec{r}\right)\right. \tag{2.38}$$

where the Fourier coefficients are

$$\phi_q = \frac{1}{V}\int \phi \exp\left[2\pi i\left(\vec{R}_q \cdot \vec{r}\right)\right] d\vec{r} \tag{2.39}$$

Therefore,

$$\phi_q = -\frac{e^2}{\pi m v^2}\frac{F\left(\vec{R}_q\right)}{V} = -\frac{e^2\lambda^2}{mc^2\pi}\frac{F\left(\vec{R}_q\right)}{V} \tag{2.40}$$

where $F\left(\vec{R}_q\right)$ is the structure factor for the reciprocal vector $\vec{R}_q$.

When x-rays propagate through the crystal, Maxwell's equations must be followed

$$\nabla^2 \vec{D} - \frac{1}{c^2}\frac{\partial^2 \vec{D}}{\partial t^2} = -\nabla \times \left[\nabla \times \left(\phi \vec{D}\right)\right] \tag{2.41}$$

When a plane wave of x-rays with wave vector, $\vec{K}_0$, passes through a crystal according to Ewald's theory[15], a large number of diffracted waves will be excited. The scattered waves interfere with each other and form a *wave-field* inside the crystal. The diffracted waves are associated with the reciprocal lattice

$$\begin{aligned} \vec{D} &= \sum_n \vec{D}_n \exp\left\{2\pi i \nu t - 2\pi i\left(\vec{K}_0 + \vec{R}_n\right)\cdot \vec{r}\right\} \\ &= \sum_n \vec{D}_n \exp\left\{2\pi i \nu t - 2\pi i \vec{K}_n \cdot \vec{r}\right\} \end{aligned} \tag{2.42}$$

where $\vec{R}_n$ is the reciprocal lattice vector and the summation is over all reciprocal lattice. $\vec{K}_n$ is the diffracted wave associated to $\vec{R}_n$ and

$$\vec{K}_n = \vec{K}_0 + \vec{R}_n \tag{2.43}$$

By substituting Equation (2.38) into Equation (2.42)

$$\begin{aligned}\vec{D}\phi &= \sum_n \sum_q \phi_n \vec{D}_n \exp\left\{2\pi i\left[\nu t - \left(\vec{K}_n + \vec{R}_q\right)\cdot \vec{r}\right]\right. \\ &= \sum_n \sum_q \phi_n \vec{D}_n \exp\left\{2\pi i\left[\nu t - \vec{K}_{n+q}\cdot \vec{r}\right]\right\} \\ &= \sum_m \sum_n \phi_{m-n} \vec{D}_n \exp\left\{2\pi i\left[\nu t - \vec{K}_m \cdot \vec{r}\right]\right\} \\ &= \sum_m \left(\phi\vec{D}\right)_m \exp\left\{2\pi i\left[\nu t - \vec{K}_m \cdot \vec{r}\right]\right\}\end{aligned} \tag{2.44}$$

where a new index number $m=n+q$ is taken and

$$\left(\phi\vec{D}\right)_m \equiv \sum_n \phi_{m-n}\vec{D}_n \tag{2.45}$$

Let us substitute Equation (2.42) and Equation (2.44) into Equation (2.41)

$$\begin{aligned}&\left(K_m - \frac{\nu^2}{c^2}\right)\vec{D}_m = {K_m}^2 \sum_n \phi_{m-n}\vec{D}_{n[m]} \\ &= \left(K_m - {k_0}^2\right)\vec{D}_m\end{aligned} \tag{2.46}$$

where $\vec{D}_{n[m]}$ is the component of $\vec{D}_n$ perpendicular to $\vec{K}_m$ and

$$k_0 = \frac{\nu}{c} = \frac{1}{\lambda} \tag{2.47}$$

Equation (2.46) shows the coupling between the incident and the scattering waves in the crystal. There are infinite sets of non-trivial solutions to Equation (2.46). Each set of solutions is known as a *tie point*. A tie point matches a set of allowed wave vectors in the crystal. The loci of all tie points form a surface in reciprocal space, which is known as the *dispersion surface*.

2.3.3 Dispersion surface

The locus of the non-trivial solutions of Equation (2.46) forms the dispersion surface in reciprocal space. The dispersion surface is a "constant energy" surface which is similar to the "Fermi surface" in electron band theory of solids[17]. In this section, the dispersion surface for the one-wave approximation and the two-wave approximation will be demonstrated.

2.3.3.1 One-wave approximation

When there is only one wave propagating in the crystal, Equation (2.45) becomes

$$\frac{\left(K_0^{\,2}-k_0^{\,2}\right)}{K_0^{\,2}}\vec{D}_0=\phi_0\vec{D}_0\approx 2\varepsilon_0\vec{D}_0 \tag{2.48}$$

where

$$K_m=k_0\left(1+\varepsilon_m\right) \tag{2.49}$$

A non-trivial solution of equation (2.43) is the dispersion condition

$$K_0=nk_0=\left(1+\frac{1}{2}\phi_0\right)k_0=k_0\left\{1-\frac{e^2}{mc^2}\frac{\lambda^2}{2\pi}\frac{F(0)}{V}\right\} \tag{2.50}$$

where n is the refraction index of the crystal.

Equation (2.50) shows the magnitude of the allowed wave vectors in the crystal under the one-wave approximation. However, there is no limitation on the propagating direction of the wave. Therefore, the dispersion surface is a spherical surface with a radius K_0 (as shown in Figure 2.4).

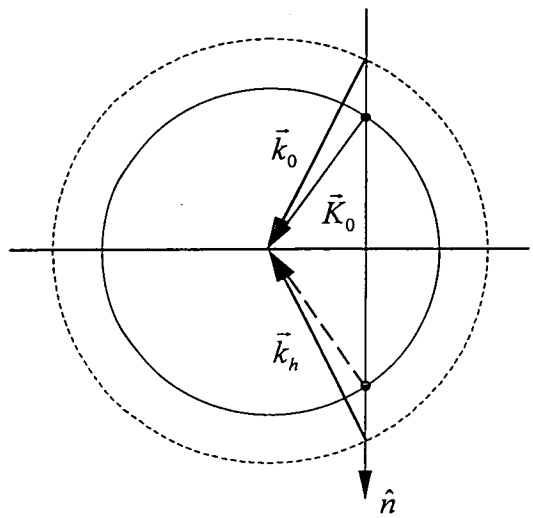

(a)

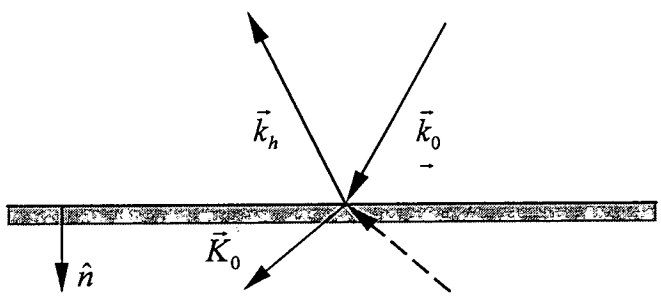

(b)

Figure 2.4 (a) The dispersion surface in the one-wave approximation case and the wave fields determined by the dispersion surface and the boundary condition. The dash arrow represents the reflecting wave from bottom interface of the thin film sample with finite thickness. (b) The waves in real space.

2.3.3.2 Two-wave approximation

When two waves, incident and diffracted waves, propagate in a crystal simultaneously, they will interfere with each other. In this case, the two-wave approximation is applied and equation (2.46) becomes

$$\begin{cases} 2\varepsilon_0 \vec{D}_0 = \phi_0 \vec{D}_{0[0]} + \phi_{\bar{h}} \vec{D}_{h[0]} \\ 2\varepsilon_h \vec{D}_h = \phi_h \vec{D}_{0[h]} + \phi_0 \vec{D}_{h[h]} \end{cases} \tag{2.51}$$

$$\begin{cases} (\phi_0 - 2\varepsilon_0)\vec{D}_0 + \phi_{\bar{h}} C \vec{D}_h = 0 \\ \phi_h C \vec{D}_0 + (\phi_0 - 2\varepsilon_h)\vec{D}_h = 0 \end{cases} \tag{2.52}$$

Here, C is the *polarisation factor*: $C = 1$ for σ polarisation ($\vec{D}$ perpendicular to scattering plane) and $C = \cos(2\theta)$ for π polarisation ($\vec{D}$ parallel to scattering plane).

For the non-trivial solution of equation (2.52)

$$(\phi_0 - 2\varepsilon_0)(\phi_0 - 2\varepsilon_h) = C^2 \phi_h \phi_{\bar{h}} = C^2 |\phi_h|^2 \tag{2.53}$$

Equation (2.53) gives a dispersion surface which is shown in Figure 2.5. The dispersion surface in this case consists of two spheres of radius nk_0 centred at O (the initial end of the incident wave vector) and H (the initial end of the diffracted wave vector). However, non-linear behaviour around the crossovers occurs and small gaps result. This phenomenon is similar to the band gap in electron band theories of solid.

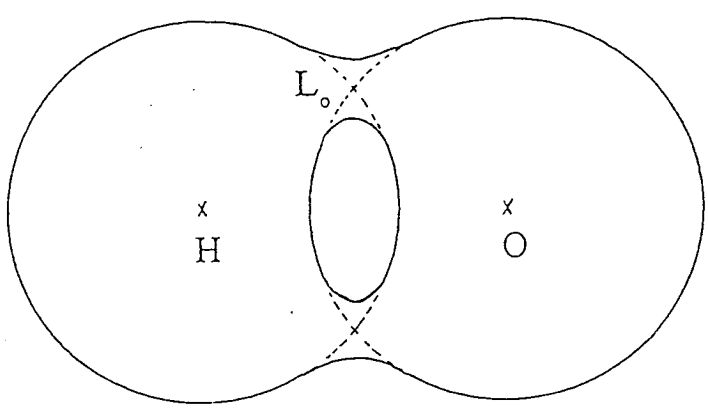

Figure 2.5 The dispersion surface of the two-wave approximation case

2.3.4 Boundary conditions

The dispersion surface shows all possible allowed waves in a crystal with the same frequency or energy. When an x-ray is incident in a crystal, the incident wave vector and the boundary condition determine which allowed wave vectors will be excited. So far, we have assumed that the crystal is infinite and there is no boundary. However, this never exists in the real world. The x-ray is always incident outside the crystal, injects energy into the crystal, and establishes the wave field inside the crystal. The boundary condition determines the wave fields that survive in the crystal. Because of the phase continuity at the surface, when a wave $\vec{k}_0$ outside the crystal gives rise to a wave $\vec{K}_0$ inside it, the phase velocities of the two related waves parallel to the surface must be the same. That is to say, the component of the two wave vectors $\vec{k}_0$ and $\vec{K}_0$ parallel to the surface must be equal. This is true for all pairs of directly related waves inside and outside the crystal.

2.3.4.1 One-wave approximation

When no diffraction occurs inside the crystal, there is only the transmission wave field established. Figure 2.4 shows that the construction of the wave fields in a semi-infinite crystal under the one-wave approximation. $\vec{k}_0$ is the incident x-ray from outside the crystal and $\vec{K}_0$ is the excited wave inside the crystal. By matching the boundary condition, the relationship between the incident wave vector and refracted wave vector is

$$k_0 \cos\theta = K_0 \cos\theta' \tag{2.54}$$

This result is an analogue of Snell's law in optics.

2.3.4.2 Two-wave approximation

In most cases, all the diffracted waves are too far away from reciprocal lattice points except one. So, there is only one diffracted wave excited. The transmitted and only the diffracted waves propagate inside the crystal and the two-wave approximation is

required. This is a much more important and realistic case. An incident wave $\vec{k}_0$ from outside the crystal excites a transmitted wave $\vec{K}_0$ inside the crystal, and then scattered to a diffracted wave $\vec{K}_h$. There are two different cases of the diffraction geometry: the Laue case and the Bragg case (Figure 2.6). In the Laue case, the diffracted beam is directed towards the crystal (transmission diffraction). However, in the Bragg case, the diffracted beam is directed towards the crystal surface and eventually escapes from the crystal (reflection diffraction). Throughout this thesis, all the x-ray scattering experiments were taken in the Bragg case geometry. It will be further discussed hereafter.

Figure 2.7 shows the construction of the diffraction of two-wave approximation graphically. In the figure, *O* is the origin of the reciprocal space and *H* is the lattice where the diffraction occurred. Two spheres with a radius of $k = \frac{\nu}{c}$ are drawn centred at *O* and *H* respectively and intersected at L_a, the *Laue point*, which is the centre of Ewald sphere in kinematical theory. The sphere centre at *O* is known as the *incident circle* (*II* in Figure 2.7(b)), which is the locus of the starting point of the incident wave vector. The dispersion surface in this case is described by another two spheres with smaller radius, $K = nk$, centred at *O* and *H*, where *n* is the refractive index. Around the intersection L_o, the *Lorentzian point*, the dispersion surfaces show non-linear behaviour and become two hyperbolas which centred at L_o. We must note that the radii of these hyperbolas are only the order of $10^{-6} \cdot k$. In Figure 2.7, $\vec{k}$ (L_aO) is the incident wave vector which completely satisfies the Laue condition regardless of dispersion. Let us consider another incident wave, $\vec{k}_0$, with a small angular offset, $\Delta\theta$, form $\vec{k}$ and with a starting point at *P* on the incident circle, *II*. Draw a line which passes through *P* and is parallel to the surface normal direction $\hat{n}$. This line will intersect with the dispersion surface (*DD*) at a tie point *A*. *AO* ($\vec{K}_0$) and *AH* ($\vec{K}_h$) are the transmission and diffraction wave inside the crystal. Because *A* is the

intersection of the dispersion surface and the surface normal, $\vec{K}_0$ and $\vec{K}_h$ are the solutions of the dispersion equations and satisfy the boundary conditions.

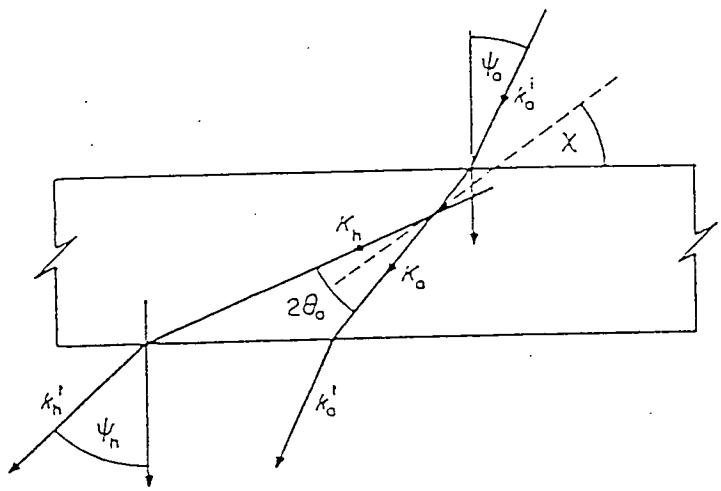

(a)

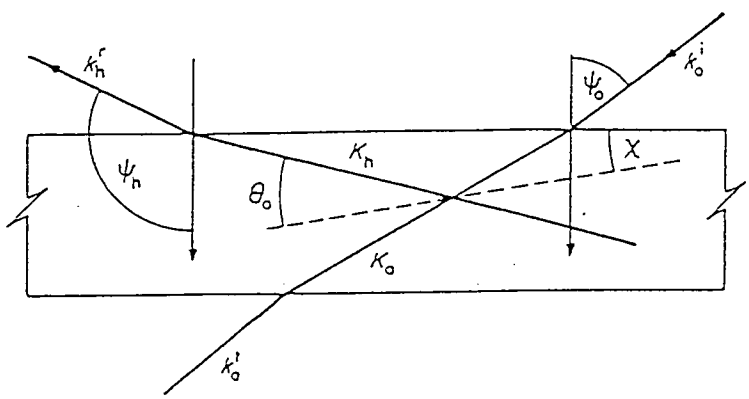

(b)

Figure 2.6 (a) Laue case (transmission). (b) Bragg case (reflection)

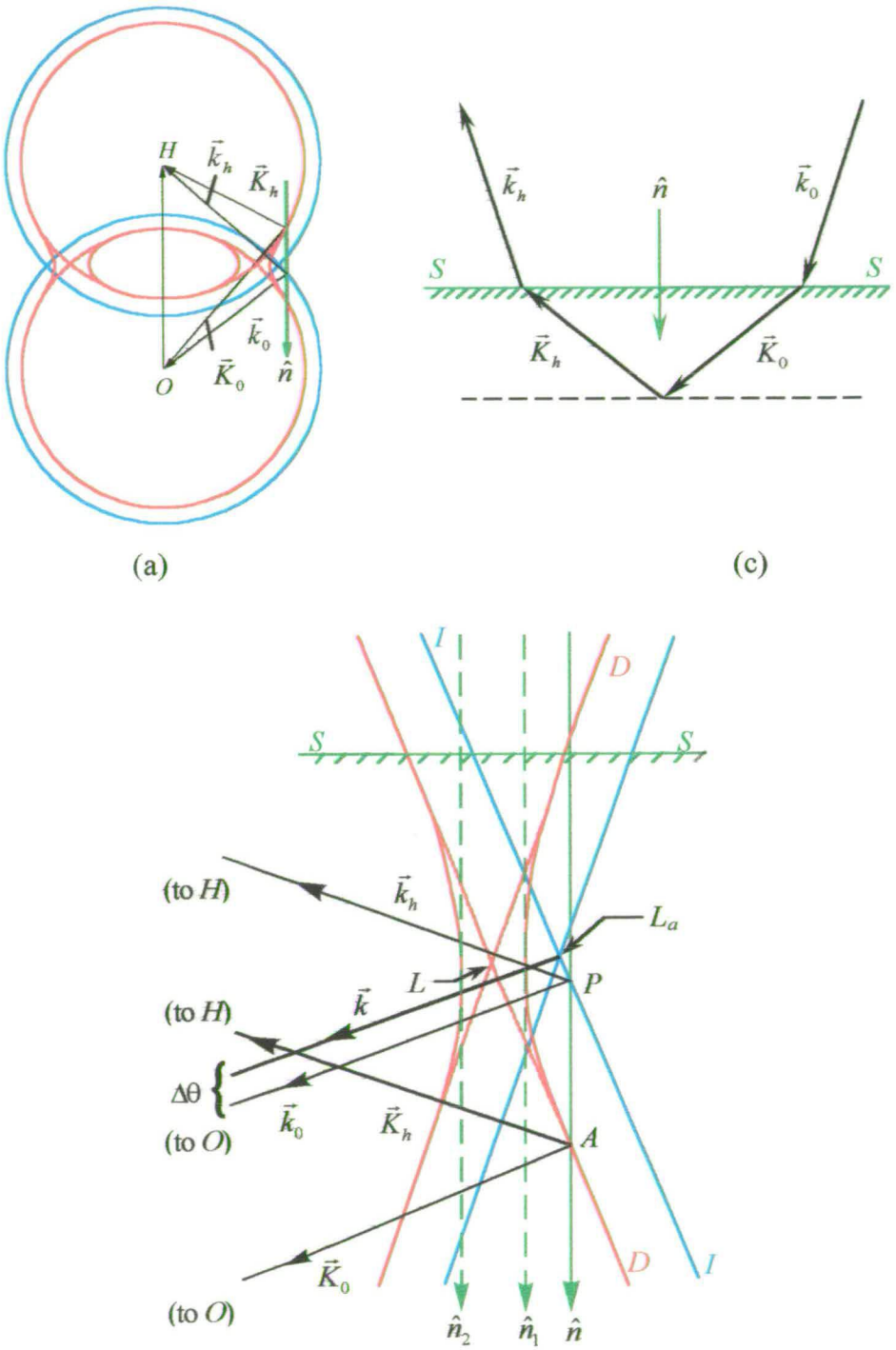

Figure 2.7 The construction of the wave fields in two-wave approximation (Bragg case) (a) in reciprocal space (b) the enlarged view around the Laue point (c) in real space. The blue lines represent the incident and diffracting spheres, red lines represent the dispersion surface and the green lines represent the surface and surface normal.

By changing $\Delta\theta$, P moves on the incident circle. The tie point, which stays on the same surface normal with P, also moves on the dispersion surface. However, when P is located between $\hat{n}_1$ and $\hat{n}_2$, there is no intersection between the surface normal and the dispersion surface. In other words, there is no real solution of the dispersion equation which fulfils the boundary condition. Therefore, no wave can propagate inside the crystal which is excited by the incident wave. However, because the energy must be conserved, it is clear that all the energy has been completely reflected. This is thus a total reflection region. Therefore, dynamical theory predicts a total reflection region on the rocking curve of a highly perfect crystal. The detailed calculation gives intensity profiles similar to Figure 2.8 with a flat total reflection platform and $(\Delta\theta)^{-2}$ tails.

The integrated intensity can also be calculated by dynamical theory,

$$E = \frac{P_0}{\omega}\frac{8N\lambda^2}{3\pi}|F|\left(\frac{e^2}{mc^2}\right)^2\left(\frac{1+\cos^2 2\theta}{2\sin 2\theta}\right) \tag{2.55}$$

Compared with Equation (2.25), it is clear that the integrated intensity is proportional to $|F|$ in dynamical theory but to $|F|^2$ in kinematical theory.

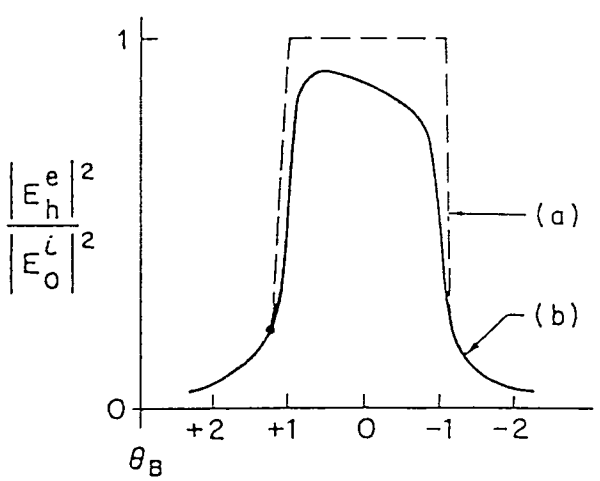

Figure 2.8 The theoretical rocking curve with and without absorption. (a) without absorption. (b) with absorption.

The above derivation assumes that there is no x-ray absorption in the crystal. However, there is always some x-ray absorption. To retain the mathematics, it is convenient to generalise the structure factors as complex.

2.4 Summary

In most real cases, the scattering cross-section of the x-ray is sufficient small so that the kinematical approximation is valid. However, for highly perfect crystals, such as a silicon single crystal, the reflectivity is so high that the kinematical approximation is no longer correct. When a strong reflection occurs, the interaction between the x-rays and the crystal become strong. The primary and diffracted beams interfere with each other inside the crystal and dispersion occurs. The most important thing in this process is the energy conservation which is completely neglected in the kinematical theory. However, when the dispersion correction is very small ($\sim 10^{-6}$), the kinematical and dynamical results are close enough in many cases. Unlike kinematical theory, dynamical theory is no longer based on the Fourier transformation of the electron density. Therefore, it is possible to reveal the phase information of the scattering.

In the early days of x-ray scattering, the dynamical theory was applied to explain the abnormal reflection intensity and the extinction phenomena of high quality crystals such as those of NaCl crystal. Because it was difficult to access high brilliance x-ray source and high quality single crystals, there were very few applications which needed dynamical theory. However, because of the availability of high brilliance x-ray source, such as rotating anode x-ray generators or synchrotron radiation sources, dynamical theory is not only active in basic science research but also in industrial applications. High-resolution x-ray diffraction, x-ray topography, interferometry are some of the new applications and can only be explained adequately by dynamical theory.

In this chapter, the theoretical aspects of x-ray scattering were reviewed. The instrumentation required will be presented in next chapter.

[1] R.W.James, Solid State Phys. **15**, 53 (1963)

[2] W.Z.Zachariasen, *Theory of X-ray Diffraction in Crystals* (Dover, New York, 1967)

[3] R.W.James, *The Optical Principles of the Diffraction of X-ray* (Ox Bow Press, Woodbridge, 1982)

[4] L.H.Schwartz, and J.B.Cohen, *Diffraction from Materials* (Springer-Verlag, Berlin, 1987)

[5] B.E.Warren, X-*ray Diffraction* (Dover, New York, 1990)

[6] The International Union of Crystallography, *International Tables for X-ray Crystallography*, Vol. IV (Kynoch Press, Birmingham, 1974)

[7] G.Arfken, *Mathematical Methods for Physicists* (Acadmic Press, 1985)

[8] J.M.Cowley, *Diffraction Physics* (North-Holland, Amsterdam, 1975)

[9] R.N.Bracewill, *The Fourier Transform and Its Application* (McGraw-Hill, New York, 1978)

[10] This is only true for perfect crystal without any mosaicity.

[11] S.R.Andrews, and R.A.Cowley, J. Phys. C: Solid State Phys. **18**, 6427 (1985)

[12] I.K.Robinson, Phys. Rev. B **33**, 3830 (1986)

[13] C.A.Lucas, P.D.Hatton, S.Bates, T.W.Ryan, S.Miles, and B.K.Tanner, J. Appl. Phys. **63**, 1936 (1988)

[14] C.G.Darwin, Phil. Mag. **27**, 315,675 (1914)

[15] P.P.Ewald, Ann. Physik **49**, 1, 117 (1916); **54**, 519 (1917)

[16] M.von Laue, Ergeb. Exakt. Naturw. **10**, 133 (1931)

[17] A.Authier, *"Dynamical Theory of X-ray Diffraction"*, in *X-ray and Neutron Dynamical Diffraction: Theory and Applications* (Plenum Press, New York, 1996)

Chapter 3

Experimental Techniques of X-ray Scattering

3.1 Introduction

In the previous Chapter, the kinematical and dynamical theories of x-ray scattering were succinctly reviewed. X-ray scattering is undoubtedly a powerful technique in exploring the structure of materials. The aim of this chapter is to demonstrate how to implement the theories in experiments. The general nature of the x-ray sources and the diffractometers will be discussed in the next two sections. The principles of data collection by diffractometers will be presented next. Then, various scan procedures will be illustrated and discussed. Finally, two different diffractometers where the experiments in this thesis were performed will be presented: the in-house CPEX diffractometer, University of Durham, and Station 2.3, at the Synchrotron Radiation Source, Daresbury Laboratory.

3.2 Production of x-rays

One factor in an x-ray diffraction experiment is the intensity of the x-ray source employed. Conventional x-ray sources and newly-developed synchrotron radiation sources are briefly reviewed in this section. Further details about x-ray sources can be found in the references[1,2,3,4,5].

3.2.1 Conventional x-ray sources

Conventional x-ray generators produce x-rays through the interaction between electrons and materials. There are two types of generators widely employed by this method: a sealed x-ray tube and a rotating anode x-ray source. Figure 3.1 shows the structure of a traditional x-ray tube which was invented by Coolidge in 1913. A schematic drawing of the production of x-rays in a conventional x-ray tube is illustrated in Figure 3.2. An x-ray tube consists of a tungsten filament cathode and a water-cooled metal anode target. A high negative electric potential, about 30000 to 50000 volts, is applied between the filament and the target. The thermal electrons produced by the heated filament are accelerated towards the metal target. When the electrons hit the target, they transfer their energy and momentum to the target and decelerate. The energy lost due to the deceleration is partially transferred into x-rays forming a continuous spectrum. This radiation is called bremsstrahlung radiation, or, by analogy with the visible spectrum, white radiation. Furthermore, when the high-energy electrons pass through the target, the electrons of the target atoms in the inner shell are ionised. Then, electrons in the outer shell will transit into the vacancy in the inner shell and then other x-rays are emitted. Because the x-rays are generated directly from the electron transition, their energy is only related to the energy gap of the transition and their wavelength is discrete. Thus, when the voltage on an x-ray tube exceeds a certain value, sharp intensity maxima will appear at certain wavelength superimposed on the bremsstrahlung spectrum. These sharp intensity maxima are known as the characteristic lines. A full spectrum, including the bremsstrahlung radiation and the characteristic lines, from the conventional x-ray tube with a molybdenum target is shown in Figure 3.3.

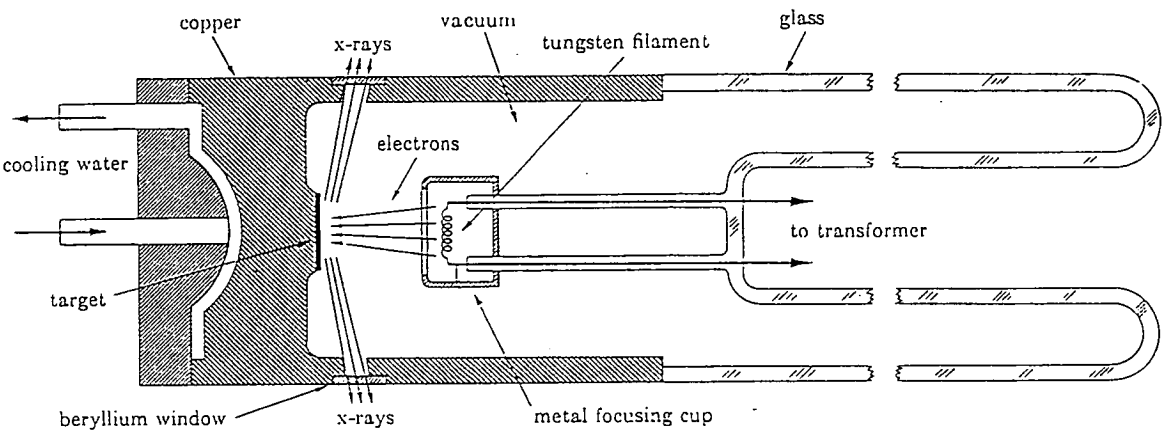

Figure 3.1 A schematic cross section drawing of a traditional x-ray tube[1]

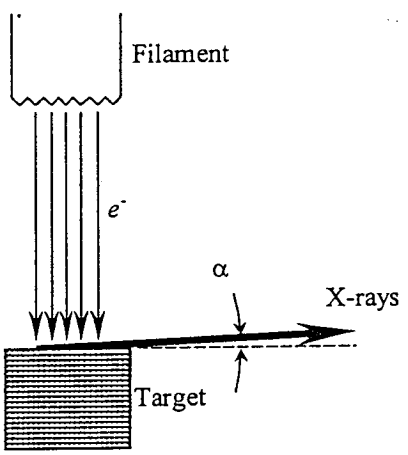

Figure 3.2 The accelerated electron beam is fired towards the target and emit x-rays

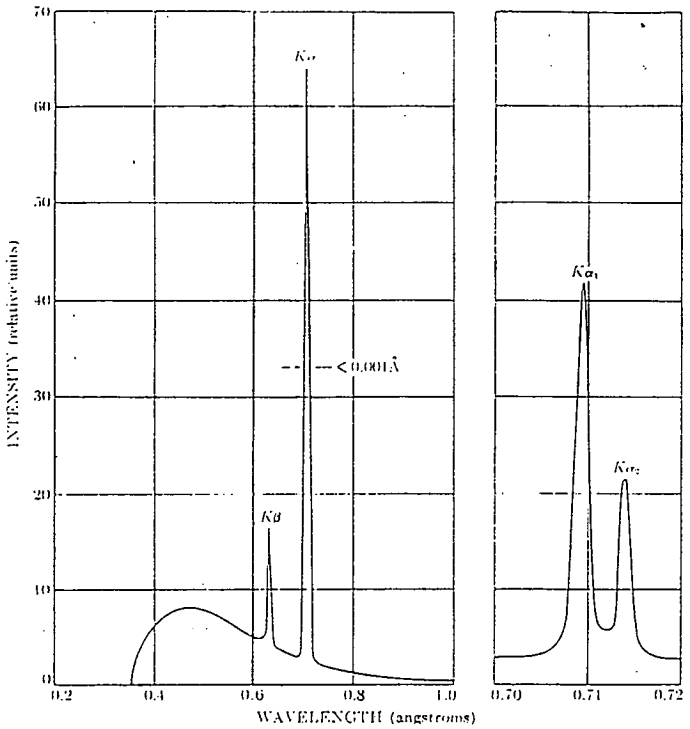

Figure 3.3 The spectrum from a conventional x-ray tube with a molybdenum target. The right panel shows the doublet of the K_α rediation.[1]

Since the efficiency of an x-ray tube is less than 1% in producing x-rays, the intensity generated from it is very low. One of the solutions to overcome this problem is the use of rotating anode generator. The anode of this generator is rotated continuously and a fresh part of the target metal is brought into the focal-spot area by the rotation. In this way, the input power of the generator can be increased without excessive heating and degradation of the anode. Figure 3.4 presents two different designs which have been used successfully. The rotating anode generators can operate at a power over ten times higher than that of conventional sealed tubes. Additionally, because the anode is removable, it is easy to change to different targets and achieve different wavelengths in different experiments. Moreover, because it is possible to open the system to the atmosphere, it is easy to change the filament, if necessary, and to clean the anode surface. However, one of the most difficult problems for this type of generators is the maintenance of the vacuum system. Because of the rotation of the anode and the ability to expose the system to the atmosphere to change the anode and for its maintenance, a dynamical vacuum system

must be used for a rotating anode generator. The dynamical vacuum system is far more delicate than the static vacuum system of the sealed x-ray tube and is difficult to maintain. Therefore, unless increased x-ray intensity is essential, sealed x-ray tubes are still the economical choice.

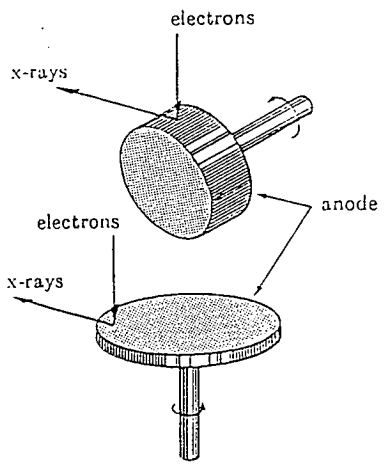

Figure 3.4 Schematic drawings of the two different geometries of the rotating anode of high-power x-ray generators[1]

3.2.2 Synchrotron radiation sources

One of the major disadvantages of a conventional x-ray source is the low efficiency. This disadvantage is caused in two ways. Firstly, much of the electron energy is converted to heat in the anode, instead of x-rays. Secondly, conventional generator emits radiation isotropically with a large solid angle and, therefore, only a small fraction of the x-rays produced is used. The employment of synchrotron radiation improves this efficiency problem.

The discovery of synchrotron radiation was in the 1940's. For decades, synchrotron radiation had been treated as an unused, and largely unwanted, by-product of many high-energy physics experiments. In the 1970's, scientists began to employ this radiation by constructing add-on facilities at some accelerators. The capability of

these "parasitic" facilities was limited because their design and scheduled operation were compromised, as their primary use was dictated by high-energy physics research. It was not until the 1980's that specialised and dedicated sources of synchrotron radiation were proposed and built throughout the world. Today, third generation synchrotron radiation sources, such as the European Synchrotron Radiation Facility (ESRF) in France and the Advanced Photon Source (APS) in USA, are also available. The latest advances in design enables these third generation generators to be super-machines with both high-brilliance and low-emittance. Figure 3.5 shows the development of the x-ray sources and their brilliance[2].

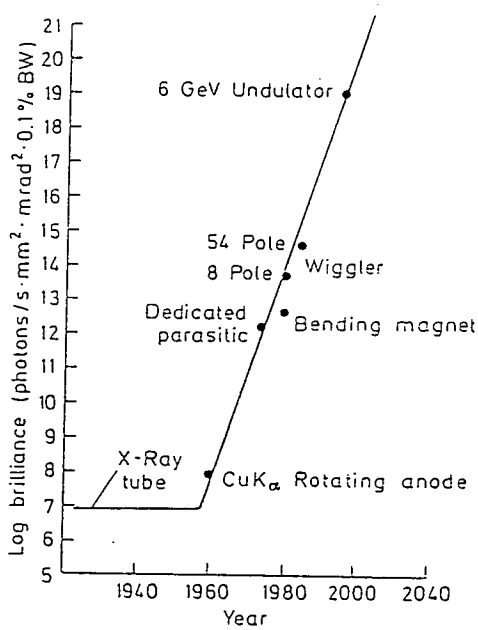

Figure 3.5 The development of x-ray sources[2]

Any synchrotron radiation source consists of three parts: a linear accelerator, a booster and a storage ring. Electrons are generated and accelerated in the linear accelerator, then, passed to the booster where their energy is raised again. Finally, the electrons with a speed close to light speed are injected into the storage ring. The storage ring is mainly a circular tube containing an ultra high vacuum. At the corners of the storage ring, dipole magnets are used to provide a central force to bend the

trajectory of the electrons and make the trajectory a stable polygonal orbital in the storage ring. When the electron are deflected, x-rays will be emitted at a tangent to the orbital with a small angular divergence of $1/\gamma$ (in radians), according to the relativistic equation.

$$\gamma = \frac{1}{\sqrt{1-\frac{v^2}{c^2}}} = \frac{E}{m_e c^2} \tag{3.1}$$

Figure 3.6 shows the synchrotron radiation x-ray fan generated by the high speed electrons when they are deflected in the magnetic field.

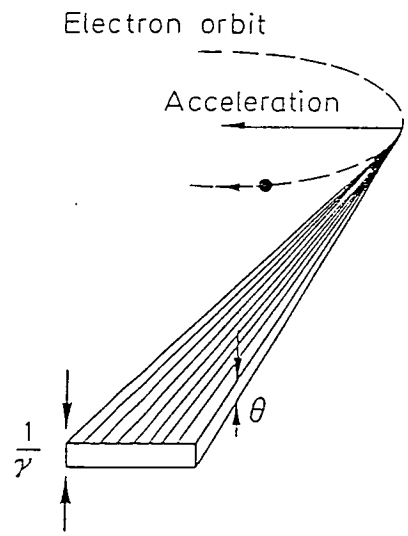

Figure 3.6 A schematic drawing of the x-ray fan from a synchrotron source[2]

Because the x-rays generated by the synchrotron radiation source are purely from the relativistic properties of electrons, their energy comes from the lost energy when they are deflected. This transform is almost 100% efficient, ensuring a much greater flux. Furthermore, synchrotron radiation is highly collimated, which means that the beam is much brighter and far more of the x-rays produced can be employed in experiments even with small samples. Figure 3.7 shows an x-ray spectrum generated

by a synchrotron radiation source. It is a continuous spectrum with a critical wavelength, λ_c.

$$\lambda_c = \frac{4\pi R}{3\gamma^3} = \frac{5.59R}{E^3} = \frac{18.6}{BE^2} \tag{3.2}$$

With monochromators and mirrors, the continuous spectrum provides the possibility of tuning the wavelength for various experiments. This is another advantage of using the synchrotron radiation sources which users are given a choice of x-ray wavelength – important in experiments employing anomalous scattering.

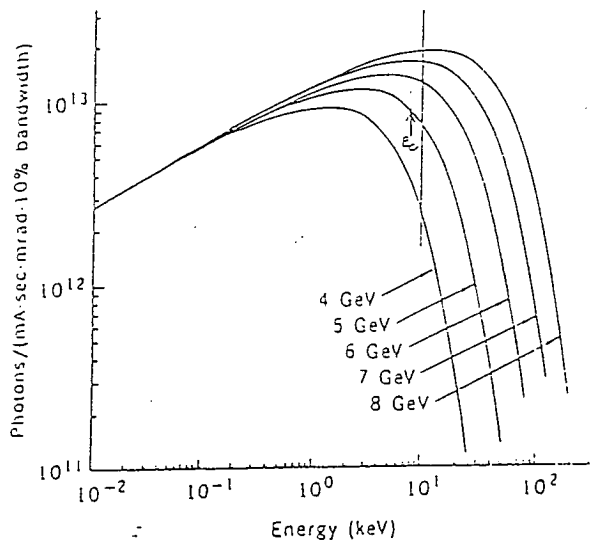

Figure 3.7 A typical x-ray spectrum generated by a synchrotron radiation source

All the experiments using synchrotron radiation source covered in this thesis were performed at the Synchrotron Radiation Source (SRS), Daresbury Laboratory. Table 3.1 shows the some major parameters of the source[3].

Table 3.1 Parameters of the Synchrotron Radiation Source, Daresbury Laboratory

Electron energy	E_0	2 GeV
Bending radius in dipoles	R_0	5.56 m
Dipole field	B	1.2 T
Relativistic factor	γ	3914
Overall radius	R	15.28 m
Orbit length	$L_0=2\pi R$	96 m
Characteristic energy	E_c	3.2 KeV
Critical wavelength	λ_c	3.9 Å
Radio frequency (RF)	ν	500 MHz
Wavelength of RF	c/ν	600 mm

3.3 Structure of diffractometer

Apart from the x-ray source, the other determinate in x-ray scattering experiments is the instrument to perform the experiments. In this section, the design and use of diffractometers will be briefly reviewed.

3.3.1 Two-circle diffractometer

The two-circle x-ray diffractometer was first used by W.H. and W.L.Bragg in their early work on the x-ray spectra and crystal structure. However, it was not widely used until the 1940's when commercial diffractometers became available. Nowadays, diffractometers equipped with computer control system and advanced detectors are widely available and have become a standard instrument in both research and industrial laboratories.

Figure 3.8 shows the major elements of a two-circle diffractometer. The x-rays from the source T are incident on a crystal C which may be set at any angle to the incident beam, ω, by rotating about an axis through O, the centre of the diffractometer. D is an x-ray detector which can also be rotated about O. The detector is set to any desired scattered angle 2θ and measures the intensity of the x-ray scattered by the

crystal. The diffractometer is directly based on Bragg's law and hence can be used for two entirely different purposes. One is to determine the structure of unknown crystals by the use of a given fixed x-ray wavelength. By measuring the diffraction pattern, or the scattering angles of Bragg reflections of the sample crystal, the structure of the crystal can be revealed. Alternatively, one can use a known d-spacing in a crystal to determine the wavelength of the incident x-rays. When a diffractometer is used to determine the x-ray wavelength involved, it is also known as a *spectrometer*.

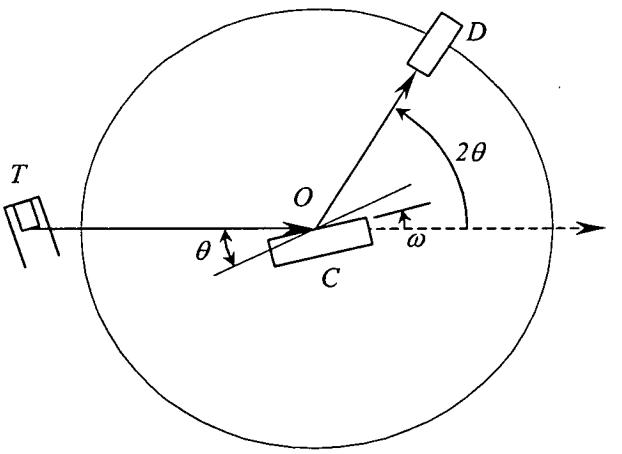

Figure 3.8 The structure of the simplest x-ray diffractometer

One of the simple methods to find out where the diffraction maximum will occur is to use Ewald's construction. Figure 3.9 illustrates a reciprocal lattice (blue spots) of a simple cubic system. X-rays with a wavevector $\vec{k}_i$ are incident on the crystal C, with a glancing incident angle, ω and then diffracted with a wavevector $\vec{k}_f$ and a scattering angle 2θ. Here, $\vec{q}$ is the diffraction vector where $\vec{q} = \vec{k}_f - \vec{k}_i$ and S is the Ewald sphere of the diffraction condition. Since $\vec{q}$ terminates at a lattice point, the diffraction maximum occurs. The scattered angle 2θ is directly related to the magnitude of $\vec{q}$ and the glancing incident angle ω is related to the direction of $\vec{q}$. Because 2θ can not exceed 180°, it is obvious that the magnitude of $\vec{q}$ can not

exceed a certain size. Consequently, it is not possible to have a $\vec{q}$ vector terminated outside the *limit circle*, L, which is a circle centred at the origin of reciprocal space with radius $2\pi/\lambda$. Furthermore, for a large crystal with a flat surface, the incident wave and diffracted wave are above the crystal. That is to say, both 2θ and ω should always be positive. Under these limitations, there are two *forbidden regions*, F, in reciprocal space within which $\vec{q}$ can never end inside these regions. So, only those lattice points within the limit circle but outside the forbidden regions are accessible by the diffractometer.[6]

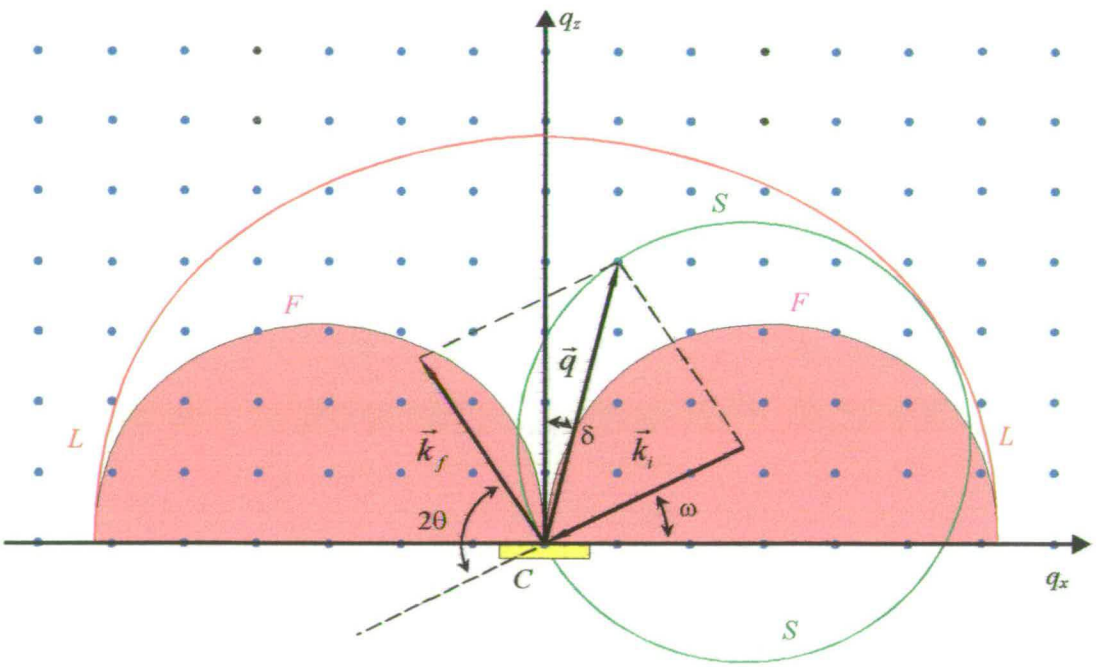

Figure 3.9 The reciprocal space and Ewald's construction of the diffraction condition

3.3.2 Four-circle diffractometer

The diffractometer discussed earlier has only two rotation adjustments, 2θ and ω. This is why it is normally referred as a *two-circle* diffractometer. Using this kind of diffractometer, the diffraction vectors accessible are only those ones on the scattering plane defined by the incident and scattering wave vectors. Therefore, only the structure along the scattering plane can be solved. To obtain information outside the

diffraction plane, more rotation adjustments are necessary to change the crystal orientation and bring the diffraction vector desired into the scattering plane. In principle, a three-circle diffractometer is sufficient to access any position in three-dimensional reciprocal space. However, more circles are necessary to avoid the limitation of a special diffraction geometry such as the forbidden regions. It is therefore popular to use a *four-circle* diffractometer in single crystal x-ray studies.

A standard *four-circle* diffractometer is shown in Figure 3.10. Two extra circles, a χ circle and a ϕ circle, are employed to change the orientation of the crystal, and thus reveal the diffraction pattern on the other planes. The definition of the circles and mathematical calculation of the operation can be found in the *International Tables for X-ray Crystallography*[7] and other references[8,9]. The two extra circles on the sample stage allow the user to select any lattice plane desired as the scattering plane. For any diffraction vector, there are infinite sets of angular settings which can achieve the desired vector. It is often possible to use some special geometry to avoid the forbidden regions. Then, the only factor which limits the applicability of diffractometer is the limit circle which is related to the wavelength of the x-ray source. This is why the four-circle diffractometer is popular in single-crystal diffraction.

There are diffractometers equipped with even more rotation adjustments for special purposes. For example, in surface diffraction measurements, the incident glancing angle and the scattering take-off angle must be fixed. In this case, a six-circle diffractometer is necessary to achieve all the diffraction vectors under the extra geometrical limitation. There are diffractometers with even more circles for special experiments.

For the reason of simplification, the diffractometer referred to in the rest of this chapter is a two-circle diffractometer unless specified.

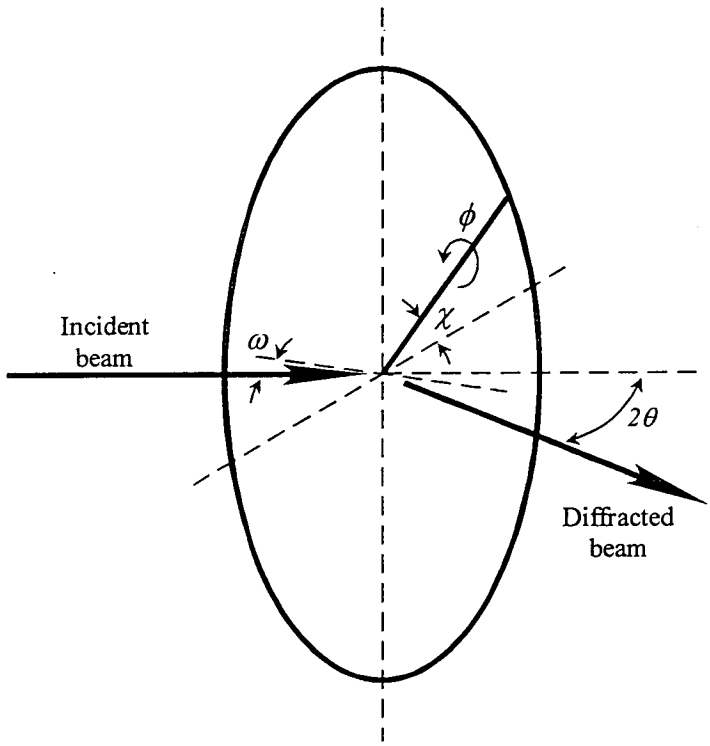

Figure 3.10 The structure of a standard four-circle diffractometer

3.4 The principles of diffraction pattern collection by a diffractometer

When ignoring dynamical effects, the diffraction pattern is the Fourier transform of the electron density distribution of the sample. Since the crystal structure is three-dimensional, the reciprocal lattice is three-dimensional, too. Hence, by collecting the diffraction pattern in three-dimensional reciprocal space, the structure of the sample, especially the periodicity, can be determined. Practically, only the diffraction pattern of the diffraction plane can be accessed directly using a diffractometer. However, by rotating the crystal and changing the orientation of the diffraction plane, the three-dimensional structure can be resolved. The aim of this section is to show how to explore the reciprocal "plane" using a diffractometer. There is an excellent review article about this topic by Fewster[6].

3.4.1 Reciprocal space mapping

As shown in Figure 3.9, any diffraction vector, $\vec{q}$, in reciprocal space has a corresponding set of angular settings (ω,2θ).

$$\begin{aligned} q_z &= k[\sin\omega + \sin(2\theta-\omega)] = 2k\sin(2\theta)\cos\delta \\ q_x &= k[\cos\omega - \cos(2\theta-\omega)] = 2k\sin(2\theta)\sin\delta \end{aligned} \tag{3.3}$$

where $k = 1/\lambda$ and $\delta = \frac{2\theta}{2} - \omega$ is the crystal offset angle from a symmetric reflection.

By sequentially changing the angular setting, one-dimensional or two-dimensional scans can be employed in collecting the diffraction pattern. The increment in the reciprocal lattice unit, Δq_z and Δq_x, are directly related to the change of the angular setting.

$$\begin{aligned} \Delta q_z &= k[\cos\omega\Delta\omega + \cos(2\theta-\omega)(\Delta(2\theta)-\Delta\omega)] \\ \Delta q_x &= k[-\sin\omega\Delta\omega + \sin(2\theta-\omega)(\Delta(2\theta)-\Delta\omega)] \end{aligned} \tag{3.4}$$

By scanning the circles of the diffractometer, an intensity map in reciprocal space can be made, which is proportional to the diffraction pattern of the crystal. This is known as a Reciprocal Space Map (RSM).

In principle, the RSM can provide all details of the diffraction pattern which is useful for revealing the structure of the sample. However, the quality of the results is strongly dependent on the resolution of the diffractometer. This will be discussed in the next section.

3.4.2 Resolution function

3.4.2.1 The relationship between instrument configuration and resolution function

Let us consider the situation in Figure 3.11, a single-axis diffractometer consists of an isotropic x-ray generator without any beam conditioner; a detector receiving signals from all directions; and a large perfect single crystal sample. Because the

sample is a perfect single crystal, there is only a single x-ray beam with the correct Bragg angle that can be diffracted and hence detected by the detector. However, no matter what the Bragg angle is, there is always at least one x-ray beam which satisfies the Bragg equation. The detector will receive the reflection from the crystal, regardless the position of the detector. In other words, although the crystal structure is "well defined" and, therefore, the Bragg angle should be accurately measured, there is no way to determine the value of the Bragg angle using this diffractometer. This diffractometer has no resolution. The resolution of a diffractometer, as a result, is an essential fact in determining the details of the sample structure.

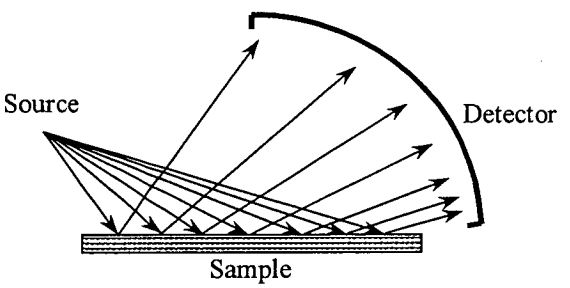

Figure 3.11 A simple single-axis diffractometer consists of an isotropic x-ray source and a detector which is able to receive signal from all directions.

To measure the diffuse intensity distribution, it is crucial to understand the resolution, or the volume of the sampling probe in reciprocal space, as a function of diffraction geometry. This is the resolution function. The resolution function strongly depends on the optical design of the instrument. In fact, the function is the convolution integral of the resolution functions of each individual optical element, such as monochromators and analysers. The general form of the resolution function of a diffractometer with m monochromators and n analysers is[10]

$$I(\Delta\omega,\Delta 2\theta)=\int_{-\infty}^{\infty}\int_{-\infty}^{\infty} J(\Delta\lambda)F(\alpha)R_{M_1}(\theta_{M_1})R_{M_2}(\theta_{M_2})\cdots R_{M_m}(\theta_{M_m})$$
$$R_S(\theta_S)R_{A_1}(\theta_{A_1})R_{A_2}(\theta_{A_2})\cdots R_{A_n}(\theta_{A_n})d\alpha d\lambda$$

where, $J(\Delta\lambda)$ is the spectrum of the x-ray source around the wavelength used, λ. α is the angular divergence of the source and $F(\alpha)$ is the intensity profile as a function of

α. $\theta_{(M,S,A)_i}$ is the angular deviation from the Bragg angle of the i-th optical element (monochromator, sample or analyser) and $R_{(M,S,A)_i}\left(\theta_{(M,S,A)_i}\right)$ is the angular resolution of the element. In this section, a qualitative demonstration of the resolution function will be presented. For reasons of simplicity, the demonstration will be restricted to a double-axis diffractometer and a simple triple-axis diffractometer with (+1,–1,+1) configuration.

3.4.2.2 The difference between double-axis and triple-axis diffractometers

At this point, we need to address the essential differences between double-axis (double-crystal) and triple-axis (triple-crystal) diffractometers. Figure 3.13 and Figure 3.12 show a double-axis diffractometer and a triple-axis diffractometer with the same angular resolution. Under the correct angular setting, the point sources (S_1) emit x-rays which pass through both diffractometers along the full lines and reach the detectors. Let us consider the other point source S_2 next to S_1. The x-rays emitted from S_2 pass through both diffractometers along the dashed lines with the same angular setting. In the double-axis instrument, the x-ray is obscured by one edge of the slit. However, in the triple-axis diffractometer, the x-ray is reflected by the analyser and detected by the detector. It is clear, as shown in Figure 3.14, that the slit in double-axis diffractometer selects the beams passing through it, regardless the direction of the beams. On the other hand, the direction of the beams is selected by the analyser, regardless their position. In other terms, the slit is a "position sensitive" optical element while the crystal analyser is a "direction sensitive" element. Therefore, a triple-axis diffractometer is sensitive to the direction and energy of the scattered x-ray beam and it probes directly a wavevector space (reciprocal space). The double-axis diffractometer, however, is not only sensitive to the direction of the scattering beams but is also sensitive to their position. The resolution of double-axis diffractometer depends on both reciprocal space and direct space effects.

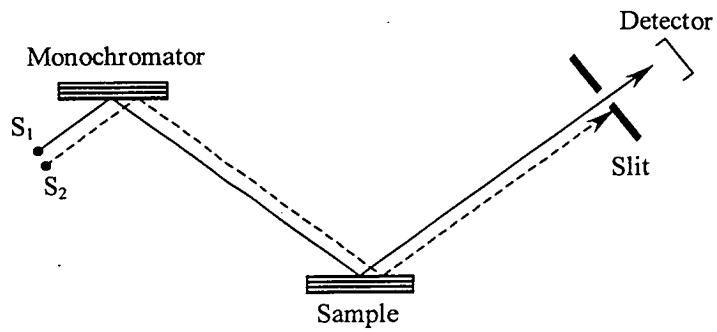

Figure 3.12 A double-axis diffractometer with the (+1,–1) configuration and using a simple slit to limit the diffraction beam divergence. The slit size is set to obtain the same angular divergence of the diffracted beam.

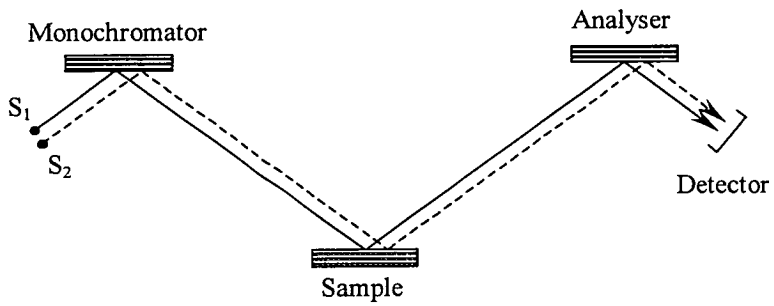

Figure 3.13 A triple-axis diffractometer with the (+1,–1,+1) configuration and using a perfect single crystal as an analyser to limit the diffraction beam divergence

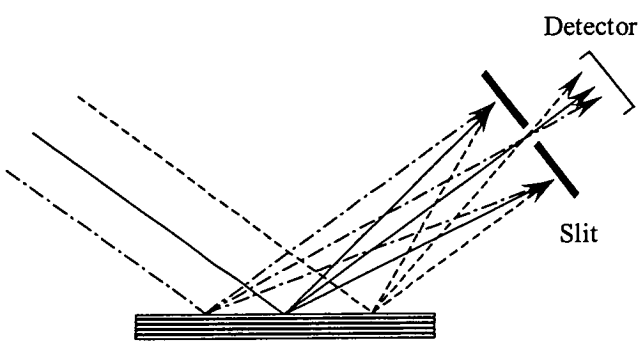

Figure 3.14 Three parallel x-rays are incident on a crystal and reflected towards a detector. A slit is introduced to select the reflected beams according to the position of the beam instead of the direction.

From the above discussion, it can be concluded that a triple-axis diffractometers are better than the double-axis ones. In fact, the resolution is even better when the

number of reflections of monochromators and analysers is increased. For example, a high-resolution four-crystal eight-reflection diffractometer shown in Figure 3.15 was built by Fewster[6,11]. The diffractometer consists of a two-crystal four-reflection monochromator in (+1,–1,–1,+1) configuration and a three-reflection channel-cut analyser in (+1,–1,+1) configuration. Using the combined advantages of the (+1,–1) nondispersive and (+1,+1) dispersive geometry, the wavelength dispersive problem is solved. With the help of the three-reflection analyser, the diffractometer has a near "δ-function" resolution probe in reciprocal space.

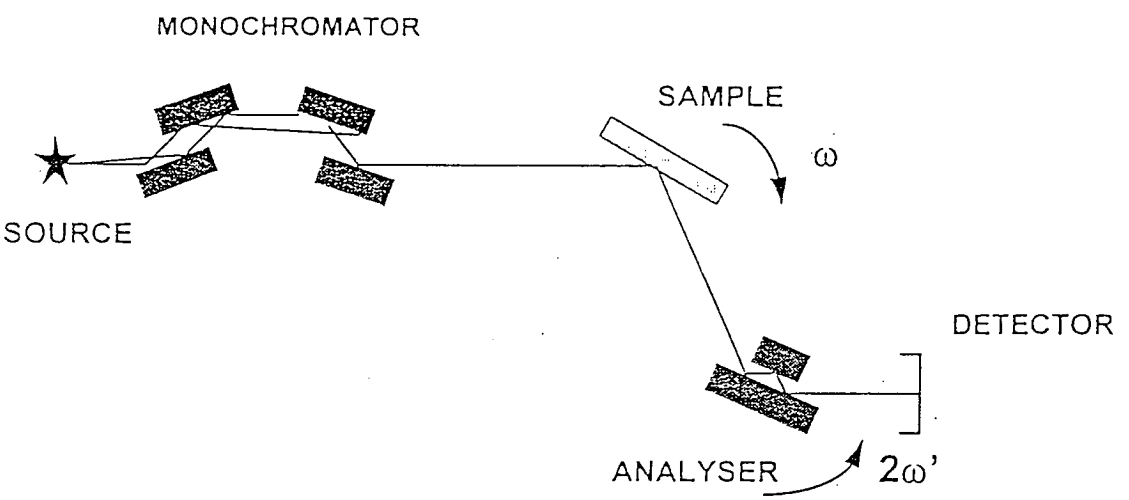

Figure 3.15 A high-resolution four-crystal eight-reflection diffractometer[6,11].

Despite the obvious benefits, increasing the resolution also implies a commensurate reduction of the signal intensity. For imperfect samples, high-resolution instruments are likely to reduce the signal of weak features thus rendering them impossible to detect. Such features may be important in determining the structure. Consequently, it is very important to reach a proper balance between the resolution and the signal intensity. Hence, it is important to understand the effects on the resolution function caused by the individual optical elements in the diffractometer.

3.4.2.3 Resolution function of individual optical elements

As discussed, the volume of the probe is essential for x-ray scattering experiments and it is closely related to the instruments employed. In this section, the resolution function from the intrinsic imperfection of individual optical element will be discussed below.

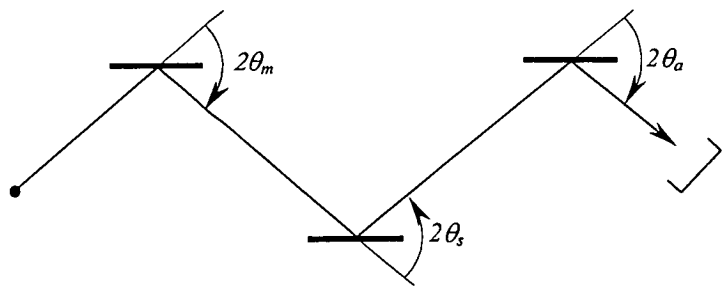

Figure 3.16 The essential elements of a triple-axis diffractometer

(a) $\Delta\theta_m$: The angular spread on the incident beam

Let us assume that the incident x-rays are perfectly monochromatic, and the sample and the analyser are both perfect crystals without any intrinsic diffraction width. The x-rays are scattered into an angular range by the monochromator. Let us consider an x-ray scattered by the monochromator with an angular deviation $\Delta\theta_m$ within the angular range, as shown in Figure 3.17. To satisfy the Bragg condition, ω and 2θ have to rotate until

$$\begin{cases} \Delta\omega = \Delta\theta_m \\ \Delta 2\theta = \Delta\theta_m \end{cases}$$

Therefore, $\Delta\omega=\Delta 2\theta$ and the locus of $\Delta\theta_m$ spread in $\omega/2\theta$ space is a straight line with gradient 1 as shown in Figure 3.18.

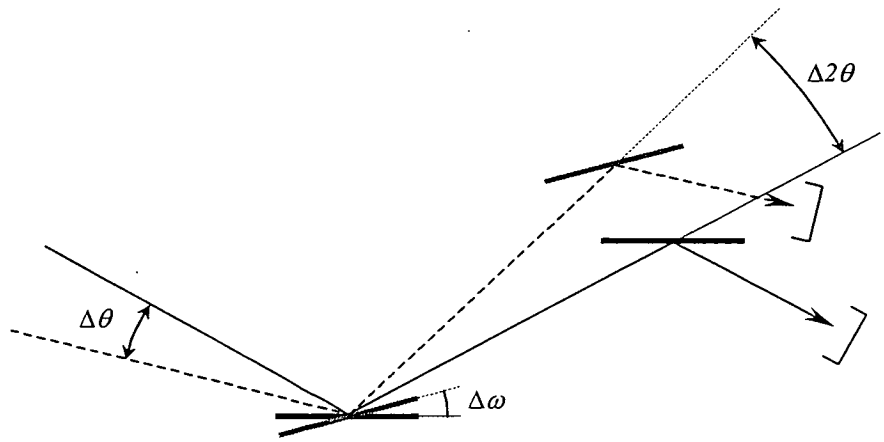

Figure 3.17 The effect of $\Delta\theta_m$ spread.

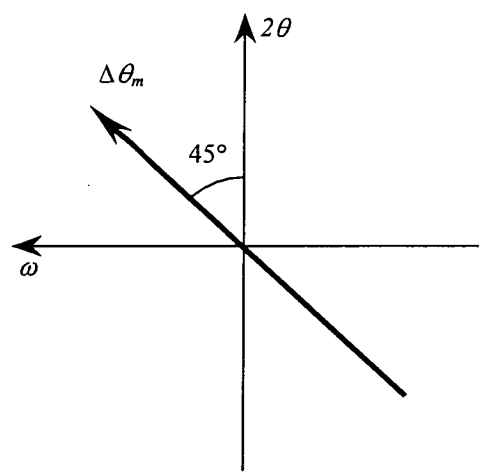

Figure 3.18 The locus of $\Delta\theta_m$ spread in $\omega/2\theta$ space

(b) $\Delta\theta_s$: The angular range through which the mosaic sample crystal can satisfy the Bragg condition

A mosaic crystal always has lots of grains with slightly different orientations. Let us consider the diffraction of a mosaic crystal on a diffractometer with monochromatic x-ray source and perfect monochromator and analyser. Because the monochromator and the analyser are all perfect crystals, and there is only single wavelength, only the incident x-ray completely matching the Bragg condition will be diffracted at both the monochromator and the analyser. To satisfy the Bragg condition of the sample, 2θ needs to be exactly matched because the lattice parameter of the sample is fixed.

However, ω can be rotated within a range where there is still scattering from some grains, in which the Bragg condition is fulfilled. The locus of $\Delta\theta_s$ spread caused by mosaic in $\omega/2\theta$ space is therefore a straight line along the ω axis as shown in Figure 3.19.

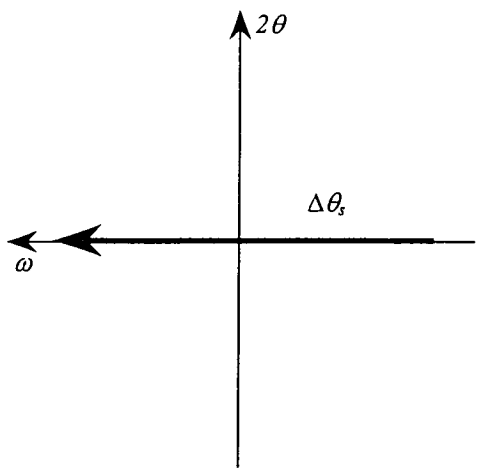

Figure 3.19 The locus of $\Delta\theta_s$ spread in $\omega/2\theta$ space

(c) $\Delta\theta_a$: The angular range through which the sample crystal can satisfy the Bragg condition

$\Delta\theta_a$ defines the acceptance angle of the detector system. Therefore, the locus of $\Delta\theta_a$ spread is simply a straight line along 2θ axis as shown in Figure 3.20.

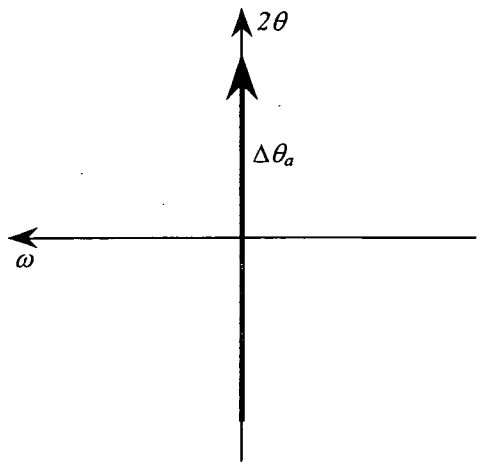

Figure 3.20 The locus of $\Delta\theta_a$ spread in $\omega/2\theta$ space

(d) $\Delta\lambda$: The wavelength spread of the incident beam

The locus of the spectral dispersion, $\Delta\lambda$, in triple-axis diffraction where $\theta_m \neq \theta_s \neq \theta_a$ is not straightforward and must be calculated.

We start with Bragg's law,

$$\lambda = 2d\sin\theta \tag{3.5}$$

The differentiation of which gives

$$\Delta\theta = \frac{\Delta\lambda}{\lambda}\tan\theta \tag{3.6}$$

So, the angular divergence after first crystal, the monochromator, is

$$\Delta\theta_m = \frac{\Delta\lambda}{\lambda}\tan\theta_m \tag{3.7}$$

The angular divergence of the second crystal, the sample, is similar to the one of monochromator. However, the sample needs to rotate through the full range of the angular divergence from monochromator.

$$\Delta\theta_s = \frac{\Delta\lambda}{\lambda}\left(\tan\theta_m - \tan\theta_s\right) \tag{3.8}$$

The negative sign is a consequence of the scattering geometry being opposite between the monochromator and the analyser in the (+1,–1,+1) configuration. Then, the angular divergence of the analyser can be calculated in a similar way.

$$\Delta\theta_a = \frac{\Delta\lambda}{\lambda}(\tan\theta_m - 2\tan\theta_s + \tan\theta_a) \tag{3.9}$$

In terms of the setting angle ω and 2θ,

$$\begin{cases} \Delta\omega = \dfrac{\Delta\lambda}{\lambda}(\tan\theta_m - \tan\theta_s) \\ \Delta 2\theta = \dfrac{\Delta\lambda}{\lambda}(\tan\theta_m - 2\tan\theta_s + \tan\theta_a) \end{cases} \tag{3.10}$$

For identical monochromator and analyser, $\theta_m=\theta_a$, Equation (3.10) can then be simplified as

$$\Delta 2\theta = 2\Delta\omega$$

So the tilting angle for the wavelength dispersion streak is

$$\alpha = \tan^{-1}\left(\frac{1}{2}\right) = 22.5^\circ$$

which is shown in Figure 3.22

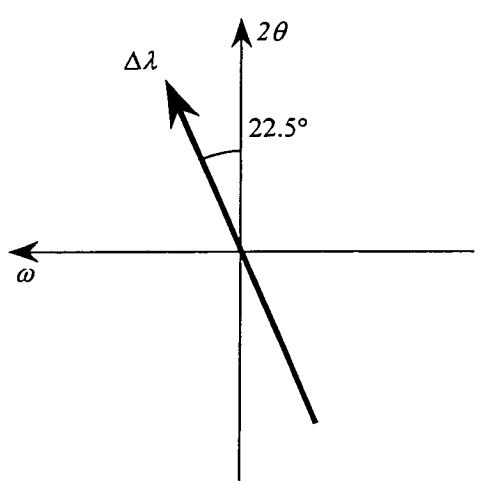

Figure 3.21 The locus of $\Delta\lambda$ spread in $\omega/2\theta$ space

Because all the loci from individual sources will convolute together with each other, all the streaks will be centred at every Bragg reflection. The resolution function can be concluded as Figure 3.22.

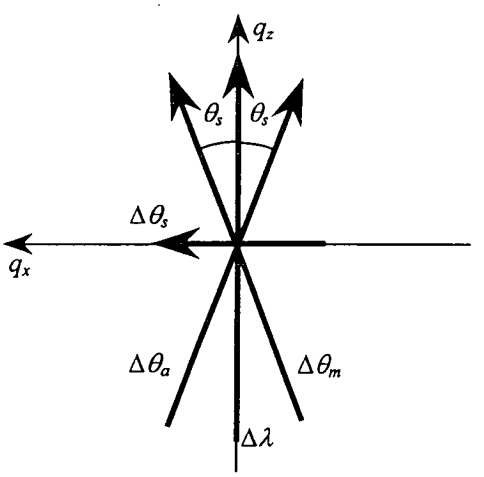

Figure 3.22 The locus of $\Delta\theta_m$, $\Delta\theta_s$, $\Delta\theta_a$ and $\Delta\lambda$ spread in reciprocal space

3.5 One-dimensional x-ray scattered intensity profiles

In principle, it is necessary to use reciprocal space mapping to get the two-dimensional (or even three-dimensional) diffraction pattern, to expose the true crystal structure. However, this is difficult to achieve and is very time consuming. Furthermore, because of the periodicity, useful information is frequently localised within small areas. In most conditions, it is possible to employ several one-dimensional scans to retrieve partial information in every scan instead of time-consuming reciprocal space mapping. Hence, it is vital to decide the proper examinations to reveal the information desired. In this section, different one-dimensional scans will be introduced. Their trace in reciprocal space and the information revealed will be discussed below.

3.5.1 θ-2θ scans

θ-2θ scans are one of the most frequently used scans. During the scans, the increment of sample tilting angle, $\Delta\omega$, and the detector angle, $\Delta(2\theta)$, are coupled together with a 1:2 ratio, and the scan passes through the point of interest. Figure 3.23 and Figure 3.24 show two typical θ-2θ scans around Bragg reflections. As shown in the figures, the Ewald sphere of diffraction moves from the green circle to the orange circle as the ω and the 2θ angle vary during the scan. From Equation (3.3), it is clear that δ is a constant through a θ-2θ scan. In other words, the diffraction vector, $\vec{q}$, remains has the same direction but with a different magnitude. This kind of scan is especially useful for on-axis scans (along the q_z direction) because they provide the information related to the periodicity perpendicular to the sample surface. For example, the lattice parameter of different parts of the sample (a layer structure or a multiphase crystal) can be measured from the peak of the intensity profile of a θ-2θ scan. The width and the line shape of the intensity profiles also gives a measurement of the sample quality because these are directly related to the uncertainty of the lattice parameters which is caused by residual strain or disorder. As shown in Figure 3.23, the scan gives the intensity profile along the surface perpendicular direction which contains information about the sample along the z direction.

As shown in Figure 3.24, when a θ-2θ scan is performed at an off-axis reflection, the trace of the scan is not along any crystal axis. The meaning of the scan becomes very confusing because there is no primitive periodicity in this direction. Hence, unless there is a special reason, this scan will rarely be used for off-axis reflections.

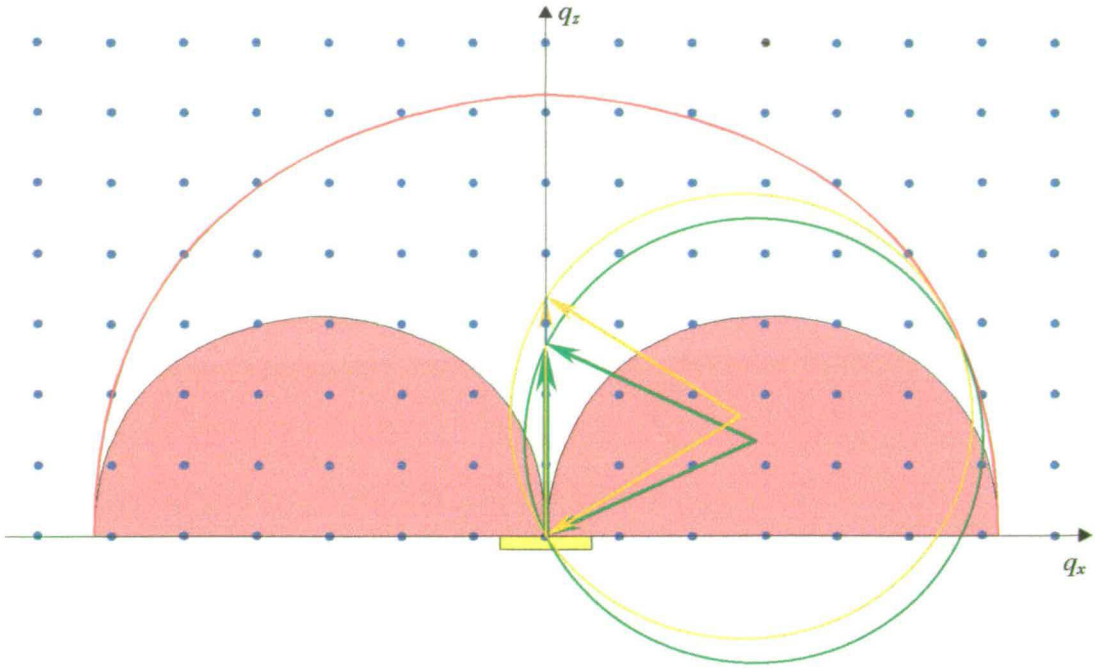

Figure 3.23 A θ-2θ scan through an on-axis Bragg reflection. The Ewald sphere of diffraction moves from the green circle to the orange circle when ω and 2θ angle varying during the scan.

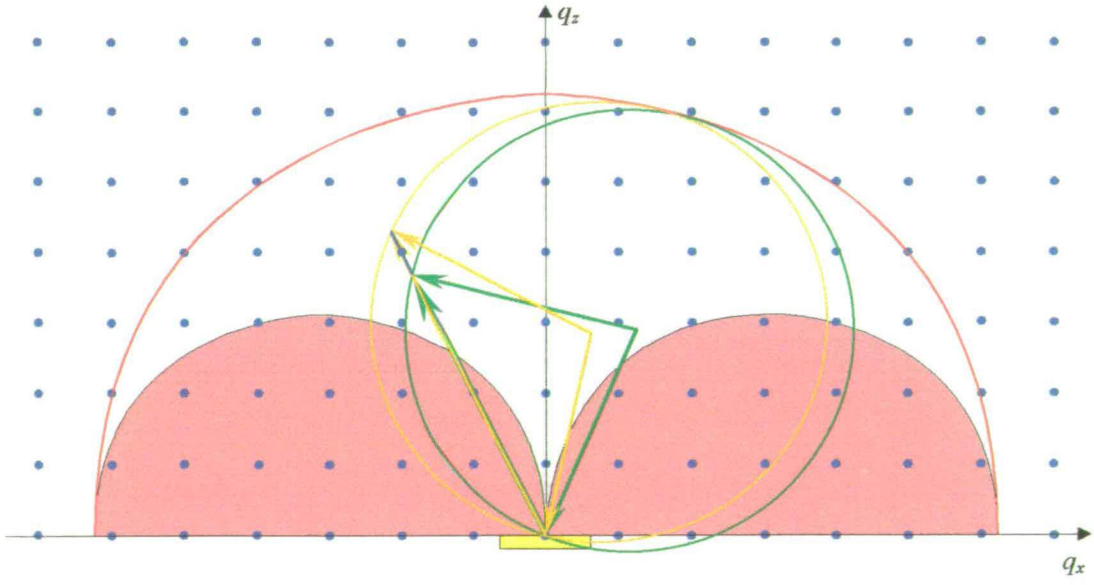

Figure 3.24 A θ-2θ scan through an off-axis Bragg reflection

3.5.2 Rocking curves

Another useful one-dimensional scan is a rocking curve. As Figure 3.25 illustrates, during the scan, the 2θ angle remains unchanged and only the glancing incident angle, ω, changes. In other words, the detector position is fixed and the diffraction intensity is recorded while the crystal is rocking. Because the 2θ angle is fixed, the lattice parameter examined is also fixed. Therefore, the scan reveals the orientation distribution of identical crystal grains within the sample. The intensity profile of a rocking curve provides information on the mosaicity of the sample, which contains important information about the crystal structure.

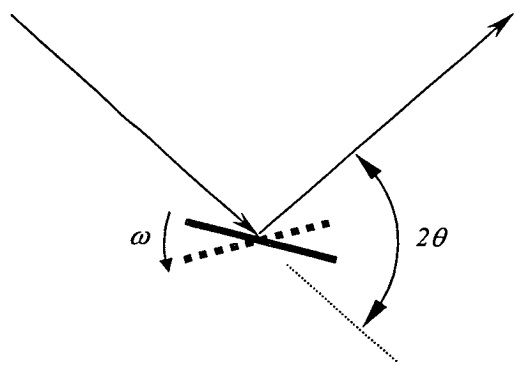

Figure 3.25 A typical rocking curve scan

Figure 3.26 shows the rocking curve scan of an on-axis Bragg reflection in reciprocal space. According to equation (3.4), because 2θ is fixed and $\Delta(2\theta)$ vanishes, then

$$\Delta q_x = -2k \sin\omega \Delta\omega$$
$$\Delta q_z = 0$$

The scan is along the q_z direction. For a perfect single crystal with no mosaicity, this scan also indicates the periodicity along the surface parallel direction. Thus, the rocking curve width is an indication of the grain size parallel to the crystal surface, or the crystal quality along the surface parallel direction.

For a rocking curve of an off-axis Bragg reflection, the scan is along the tangential direction which is not parallel to any crystal axis. Unlike the θ-2θ scan, the width of

the profile still implies the mosaicity of the crystal because the mosaicity is not directly related to any crystal axis. However, for crystal quality along the surface parallel or q_x direction of perfect crystal, the q_x scan, not the rocking curve, should be taken.

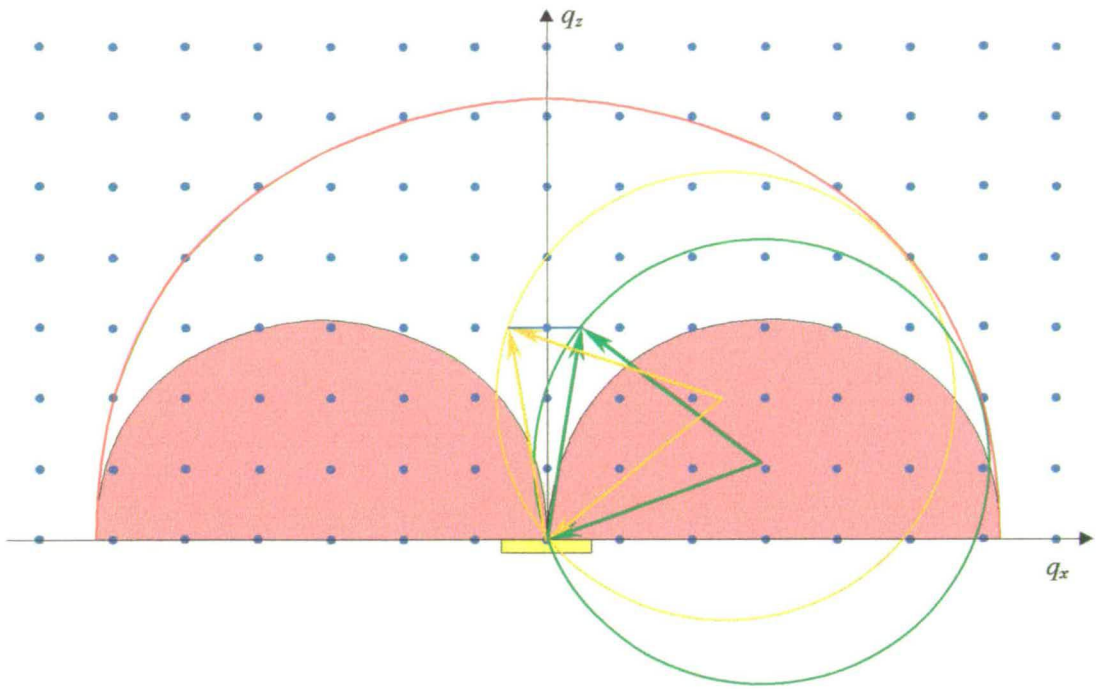

Figure 3.26 A rocking curve scan trace in reciprocal space. The Ewald sphere moves from the green circle to the orange circle during the scan.

3.5.3 Crystal-truncation-rod (CTR)

Because of the existence of the crystal surface terminations, crystal truncation rods will appear at every Bragg reflection. For a crystal truncated along the *x-y* plane, the CTR streak is along the *z* direction. In this situation, a θ-2θ scan of an on-axis reflection will give a profile of the CTR because it is along the *z* direction. For an off-axis Bragg reflection, a q_z scan, instead of a θ-2θ scan, should be performed to obtain the CTR profile. Figure 3.28 shows the construction of the CTR scan associated with an off-axis Bragg reflection. The CTR profile contains information on the surface morphology.

When a sample crystal has a mis-cut angle, the CTR streaks are parallel to the surface normal, which is not along any crystal axis. As shown in Figure 3.27, all the CTR streaks associated with different Bragg reflections, both on-axis and off-axis reflections, are parallel to each other. In this condition, to get the CTR profiles, it is necessary to perform a one-dimensional scan in reciprocal space along the surface normal direction. This is a scan with complex angular movement and can only be easily visualised or understood in reciprocal space.

Further details of the information contained in CTRs will be discussed in Chapter 6.

3.5.4 Specular reflectivity

The specular reflectivity is the intensity profile along the surface normal direction within the very small incidence angle region. Figure 3.29 illustrates a typical specular reflectivity measurement. Technically speaking, the scan is simply a θ-2θ scan along the specular reflection ridge. The scan range of θ (or ω) angle is from below the critical angle up to 2° or 3°. The total reflection critical angle is normally between 0.2° to 0.4°, depending on the material and x-ray wavelength. Because the specular reflectivity is a ridge-like profile with tiny width (normally a few mdeg), it is important that the scan is on top of the ridge. To ensure this, rocking curve scans are used to find the centre of the specular ridge prior taking any measurement. Furthermore, the ridge actually consists of the specular reflection plus the diffuse scattering, it is important to take the diffuse component off by subtracting the off-specular reflectivity profile with an off-set angle next to the ridge out of the specular ridge. In this way, the true profile consisting only of the specular component can be obtained.

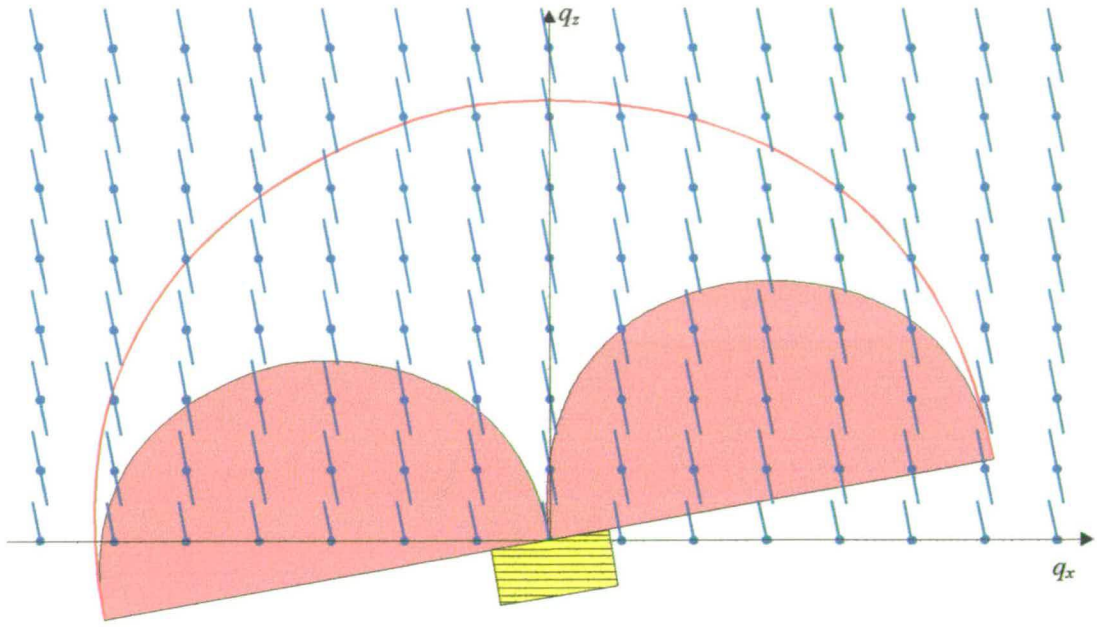

Figure 3.27 Crystal truncation rods of a crystal with surface the mis-cut to the crystallographic planes.

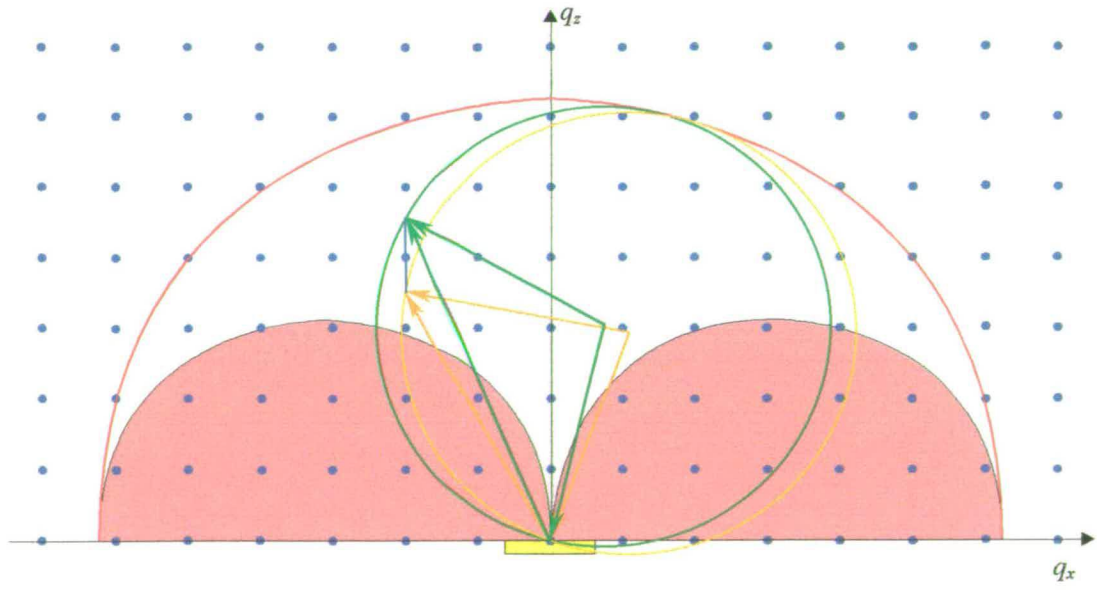

Figure 3.28 A CTR trace in reciprocal space of off-axis reflection

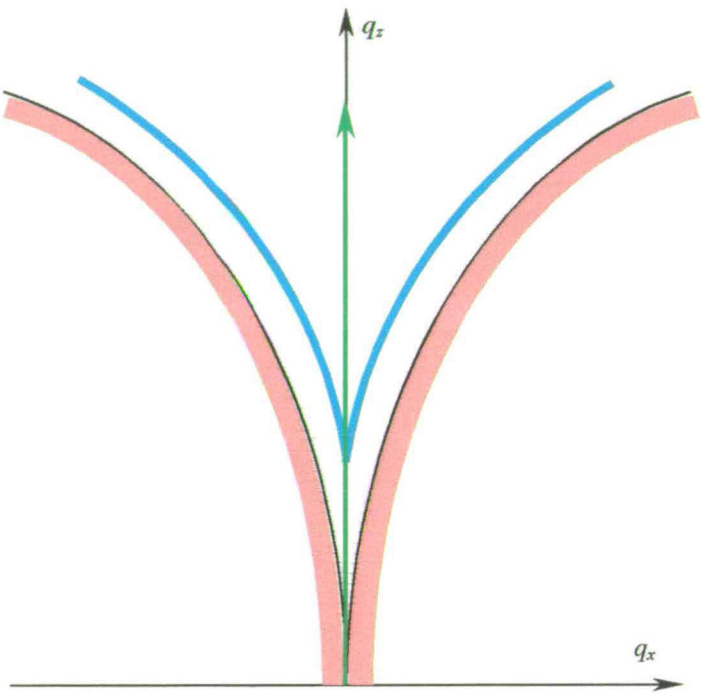

Figure 3.29 Specular reflectivity measurement trace in reciprocal space. The areas below the pink line are the forbidden regions and the blue curves represent the Yoneda wings.

The profile of the specular reflectivity gives the electron density profile of the sample along the surface normal direction. Layer thickness and density of individual layers, RMS roughness of both surface and interfaces can all be revealed by specular reflectivity. Because specular reflectivity effectively measures the (000) Bragg reflection, no information related to the lattice structure can be obtained. Furthermore, because this is an on-axis scan, it is not possible to obtain any information parallel to the surface. In order to get in-plane morphology, diffuse scattering reflectivities and off-specular longitudinal scans should be taken. These will be discussed further in the next section.

Further theoretical details of specular reflectivity will be discussed in Chapter 4.

3.5.5 Diffuse scattering reflectivities and off-specular longitudinal scans

For an ideal smooth surface, there is no diffuse scattering. The specular reflectivity gives the RMS roughness of a rough sample surface. However, there is not enough information in determining the morphology of a rough surface by using RMS roughness alone. To get the morphology of the surface, diffuse scattering should also be also examined. The roughness of the surface scatters the specular intensity to off-specular directions and reduces the specular reflectivity. In general, the diffuse scattering amplitude is the Fourier transform of the surface roughness structure. Using a self-affine fractal to model the sample surface, the fractal dimension and the correlation length of the surface can be determined by fitting the diffuse scattering intensity. Therefore, the surface can be reconstructed by the obtained parameters via both specular and diffuse reflectivity measurements.

There are two different ways to achieve the diffuse scattering profile: the diffuse scattering scans and the off-specular longitudinal reflectivity scans. Figure 3.30 shows a typical diffuse scattering scan and an off-specular longitudinal scan. The diffuse scattering scan is a rocking curve scan at a small incident angle within the reflectivity region. As shown in Figure 3.30, this is also equivalent to a one-dimensional scan along the surface parallel direction. The result of the scan will consist of the specular ridge, the diffuse scattering and two Yoneda wings, which appear at either the incident angle or the take-off angle matching the surface total reflecting critical angle. The other approach is the off-specular longitudinal scan which is simply θ-2θ scan with an offset incident angle. The profile is similar to specular reflectivity but with a different critical angle, which is related to the offset angle. The scan profile consists purely of the diffuse scattering intensity. It is possible to perform a series of diffuse scattering scans, or offset longitudinal scans, or a combination of both scans to achieve the RMS of the reflectivity area. This will certainly help when determining the true morphology of the surface. The reliability of the surface morphology obtained by reflectivity strongly depends on whether the mathematical modelling of the surface is correct. However, because of the

individuality of sample surfaces caused by many uncontrollable factors such as sample species, growth condition, preservation, contamination, etc., there is no simple mathematical model which can be used to describe general surface morphology. Even the fractal model is often inadequate for modelling some surfaces. Therefore, unless the surface is well behaved, there is no benefit in performing such a time-consuming mapping.

Further theoretical details of diffuse reflectivities will be discussed in Chapter 4.

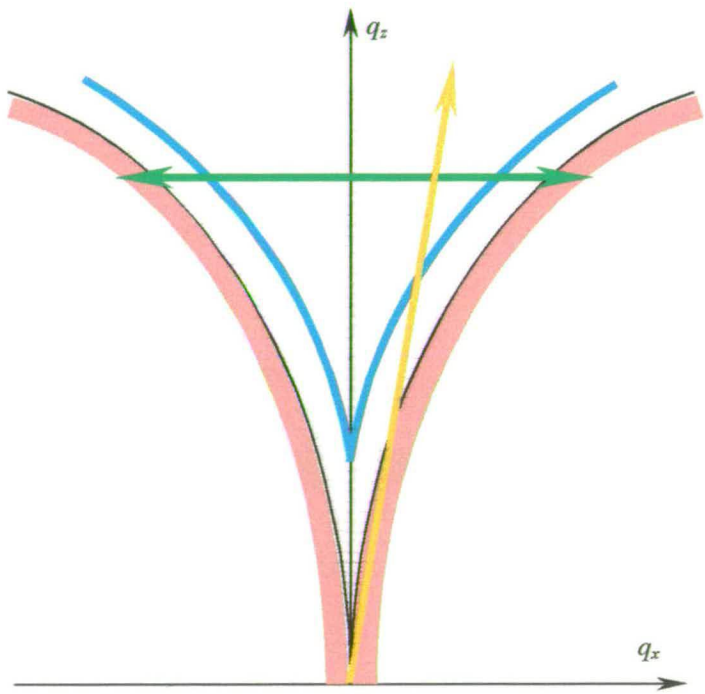

Figure 3.30 The traces of the diffuse scattering scan (green) and off-spacular longitudinal scan (orange). The areas below the pink line are the forbidden regions and the blue curves represent the Yoneda wings.

3.6 Diffractometers used in this thesis

There are two diffractometers which were used to perform the experiments in this thesis: the CPEX in-house diffractometer, University of Durham and Station 2.3, SRS, Daresbury Laboratory. The structure of these two diffractometers is presented below.

3.6.1 CPEX four-circle triple-axis diffractometer --- University of Durham

Most of the pre-experiment measurements, and some experiments, were performed using the triple-axis x-ray diffractometer, CPEX, at the University of Edinburgh which was later moved to University of Durham in 1996. Figure 3.31 shows the optical structure of CPEX system. The diffractometer is based on a Huber 430/440 four-circle goniometer. The diffractometer is equipped with a GEC Avionics GX21 rotating anode x-ray generator operating at 2.7 KW with a copper target. $CuK_{\alpha 1}$ radiation (λ=1.540562Å, $\Delta\lambda$=0.00058Å) is employed for experiments. The monochromator and analyser are arranged in (+,−,+) configuration and define the resolution of the diffractometer. Two different sets of crystals are used for monochromator and analyser to give different resolutions for different experiments.

High-resolution mode: The (111) reflections of perfect germanium crystals are used for both monochromator and analyser. These reflections have a Darwin width of 4.3×10^{-3} degrees.

Low-resolution mode: The (002) planes of pyrolytic graphite crystals are used as both monochromator and analyser. These crystals have a mosaic structure with an approximate Gaussian distribution of orientation and a mosaic spread about 0.4 degrees.

A proportional counter is used as the detector and the energy resolution is about 1.5KeV (FWHM) at 8KeV. The system is controlled by a PC computer with PINCER software. Further details of the PINCER program will be introduced in the next section.

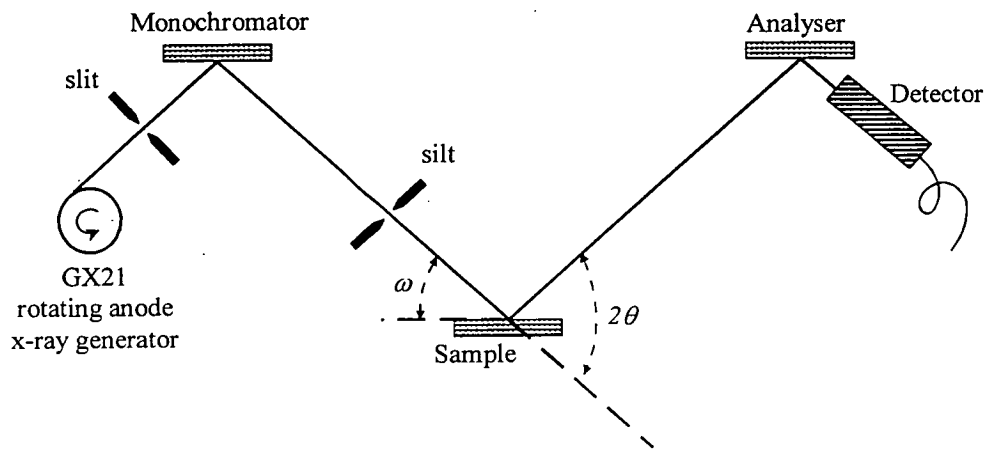

Figure 3.31 A schematic drawing of the configuration of the CPEX diffractometer

More details about the CPEX system can be found in other references[12,13,14].

3.6.2 Two-circle double-axis diffractometer --- Station 2.3, Synchrotron Radiation Source, Daresbury

The major results of this thesis were taken using Station 2.3 at the Synchrotron Radiation Source (SRS), Daresbury Laboratory. Figure 3.32 shows a schematic drawing of the station. This station is situated 16m from the tangent point of a 1.2T bending magnet. The x-ray spectrum of the station is shown in Figure 3.33. A water cooled, double bounce, Si (111) monochromator is used to select the wavelength and gives a dispersion, $\Delta\lambda/\lambda$, of 2×10^{-3} at a wavelength of 1.4 Å. The station is equipped with a two-circle diffractometer for powder diffraction and glancing incident reflection measurements. The sample axis ω and the detector axis 2θ are optically encoded and driven by DC servomotors via an intelligent data buffer and feedback loop. The accuracy of the angular movement is 0.2 and 0.1 mdeg respectively. Although no analyser stage is used in the diffractometer, high-resolution scattering is achieved by a fine detector slit (100 μm) and a large separation between the sample and the detector (655 mm). In other words, the experiments performed at this station are "pseudo-triple-axis" x-ray scattering. Further details of Station 2.3 can be found in other references[15,16,17].

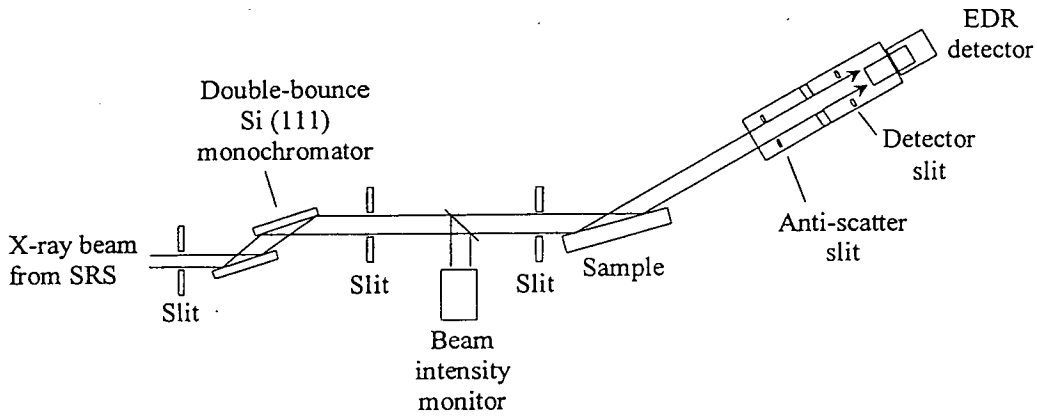

Figure 3.32 A schematic drawing of the configuration of Station 2.3 at Daresbury SRS

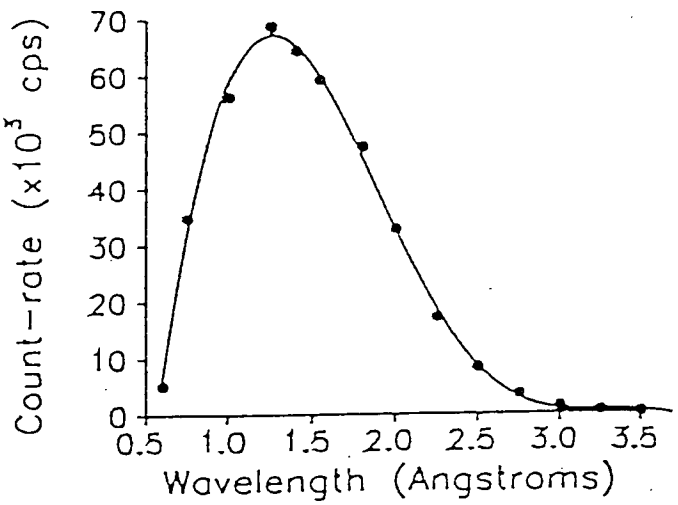

Figure 3.33 The x-ray spectrum of Station 2.3, SRS

A PC computer is used to control the motor system and to collect the experimental data through the PINCER program with PD macros on Station 2.3. PINCER (Portable INstrument Control interpretER) is a computer program developed by M. C. Miller of CCLRC, Daresbury, which was designed to control various motors and other attached devices of diffractometers on Station 2.3 and other stations. The CPEX system in Durham is also controlled by a special version of PINCER program. The program is mainly an interpreter with many of the basic macro blocks. Users are

allowed to build their own macros or group of operations upon existing macros. In Station 2.3, PD macros are used to simplify the operation without touching the PINCER code, which might require some programming. The program recognises a few different pieces of equipment from various manufacturers which make it possible to transfer the program to a different site. The latest version of PINCER employed on Station 16.3, SRS, has another layer of program called a "virtual motor" which enhances the portability and simplifies the operation. Further details about PINCER can be found in the references[18,19].

3.7 Summary

This chapter briefly reviews the experimental techniques. The aspects of x-ray sources and diffractometers, and the relationship between the diffractometer and reciprocal space were examined. Moreover, the processes and the purposes of various scans have also been highlighted. The details of two diffractometers employed in this thesis were explained at the end.

The experimental techniques presented in this chapter will be verified in the following three chapters. The surface and interface morphology of GeSi single quantum-well semiconductors will be examined using x-ray reflectivity in the next chapter. High-T_c thin film superconductors will be studied using reciprocal space mapping in chapter 5 and the crystal truncation rod interference measurements in chapter 6.

---

[1] B.D.Cullity, *Elements of X-ray Diffraction* (Addison-Wesley Publishing Company Inc., 1978)

[2] L.H.Schwartz and J.B.Cohen, *Diffraction from Materials* (Springer-Verlag, 1987)

[3] A.G.Michette and C.J.Buckley, *X-ray Science and Technology* (Institute of Physics Publishing, Bristol, 1993)

[4] A.L.Robinson, Science **295**, 1239 (1979)

[5] K.Wille, Rep. Prog. Phys. **54**, 1005 (1991)

[6] P.F.Fewster, *"Reciprocal Space Mapping"* in *X-ray and Neutron Dynamical Diffraction: Theory and Applications*, Edit by A.Authier, S.Lagomarsino, and B.K.Tanner (Plenum Press, New York, 1996)

[7] The International Union of Crystallography, *International Tables of X-ray Crystallography*, Vol. IV (The Kynoch Press, Birmingham, 1974)

[8] W.R.Rusing, and H.A.Levy, Acta. Cryst. **22** 457 (1967)

[9] E.Vlieg, J.F.van der Veen, J.E.Macdonald, and M.Miller, J. Appl. Cryst. **20**, 330 (1987)

[10] E.L.Gartstein, R.A.Cowley, Acta Cryst. A **46**, 576 (1990)

[11] P.F.Fewster, J. Appl. Cryst. **22**, 64 (1989)

[12] T.W.Ryan, Ph.D. Thesis (University of Edinburgh, 1986)

[13] R.A.Cowley, and T.W.Ryan, J. Phys. D **20**, 61 (1987)

[14] C.A.Lucas, Ph.D. Thesis (University of Edinburgh, 1989)

[15] R.J.Cernik, P.K.Murray, P.Pattison, and A.N.Fitch, J. Appl. Cryst. **23**, 292 (1990)

[16] S.P.Collins, R.J.Cernik, P.Pattison, A.M.T.Bell, and A.N.Fitch, Rev. Sci. Instrum. **63**, 1013 (1992)

[17] I.Pape, Ph.D. Thesis (University of Durham, 1997)

[18] M.C.Miller, K.Ackroyd and G.Oszlanyi, *"Portable Data Acquisition Software based on a powerful Command Interpreter and Object Oriented Hardware Control"*, presented at ESONE Real-time Data Conference (RTD94), Dubna, Russia, 27-31 July 1994; Daresbury Laboratory Preprint DL/CSE/P29E

[19] M.C.Miller, *Data Acquisition Computing Guide: PINCER DATA Acquisition*, Synchrotron Radiation Computing Group, Daresbury Laboratory (1995)

Chapter 4

A Grazing Incidence X-ray Scattering Study of the Interface Morphology of Ge_xSi_{1-x} Single Quantum Well Heterostructures with Antimony as a Surfactant

4.1 Introduction

Grazing-incidence x-ray specular reflectivity was observed as early as 1923 when Compton demonstrated the total external reflection of x-rays from the surface of a solid[1]. In 1931, Kiessig reported that the intensity oscillation fringes were observed in the reflectivity profiles of surface with a thin layer[2]. In the following 20 years, only few studies were reported with little development. Until 1954, Parratt used Fresnel's equations recursively and successfully explained the reflectivities from layered systems[3]. In his paper, Parratt also demonstrated the use of reflectivity measurements to study the copper surface. This was recognised as the first application of reflectivity. The diffuse scattering was observed by Yoneda in 1963. He reported two abnormal off-specular reflections in diffuse scattering reflectivity profiles at small-angles, which are known as Yoneda wings[4]. In 1970's, Croce and Nevot expanded the discussion of x-ray reflectivity to introduce surface roughness

into the calculation of specular reflectivity[5,6,7]. They also suggested that the Yoneda wings were caused by x-ray scattering from surface roughness.

By then, studies of glancing-incidence x-ray scattering were rare and only slowly being developed. The experimental results achievable were severely limited by the low brilliance of traditional x-ray sources[3]. In the 1980's, dedicate synchrotron radiation sources become widely available throughout the world[8,9] which accelerated the development of x-ray reflectivity. In 1988, Sinha et al. published an important paper which purported to explain the behaviour of specular and diffuse reflectivities from solid surfaces using both the Born Approximation (BA) and the Distorted-Wave Born Approximation (DWBA)[10]. The later approximation was first introduced by Vineyard in 1982[11]. The DWBA successfully describes the x-ray scattering close to the total-external reflection region where the BA is inadequate. Sinha et al. also employed the self-affine fractals to describe the surface, which had been developed by Mandelbrot[12], and demonstrated how to extract the lateral statistical information of surface roughness by analysing the diffuse scattering profiles. Further advance was achieved in 1993 when Holy et al. demonstrated the possibility of using both specular and diffuse reflectivities to reveal the roughness of individual interfaces of uncorrelated multilayers[13] and partially correlated systems[14]. Measurement of the vertical correlation across interfaces in multilayer systems is essential in understanding growth mechanisms. Nowadays, glancing-incidence x-ray scattering is one of the most powerful non-destructive techniques and is widely applied to the study of the surface morphology of surface and buried interface structures.

The properties of crystalline Ge-Si alloys have been investigated for many years because of the importance to the electronics industry. Depending on the composition, the bandgap of the alloy varies from 1.1 to 0.7 eV which corresponds to wavelengths from 1000 to 1500 Å. This is a very useful range for bipolar devices, for discrete opto-electronic devices and for integrated opto-electronics on silicon. However, due to the large lattice mis-match between germanium and silicon (~ 4.2%), it is very difficult to produce pseudomorphic epitaxial layers. Unlike lattice-matched III-V

compound semiconductors such as $Al_xGa_{1-x}As$, the growth of Ge_xSi_{1-x} alloy on germanium or silicon substrates developed very slowly with many difficulties.

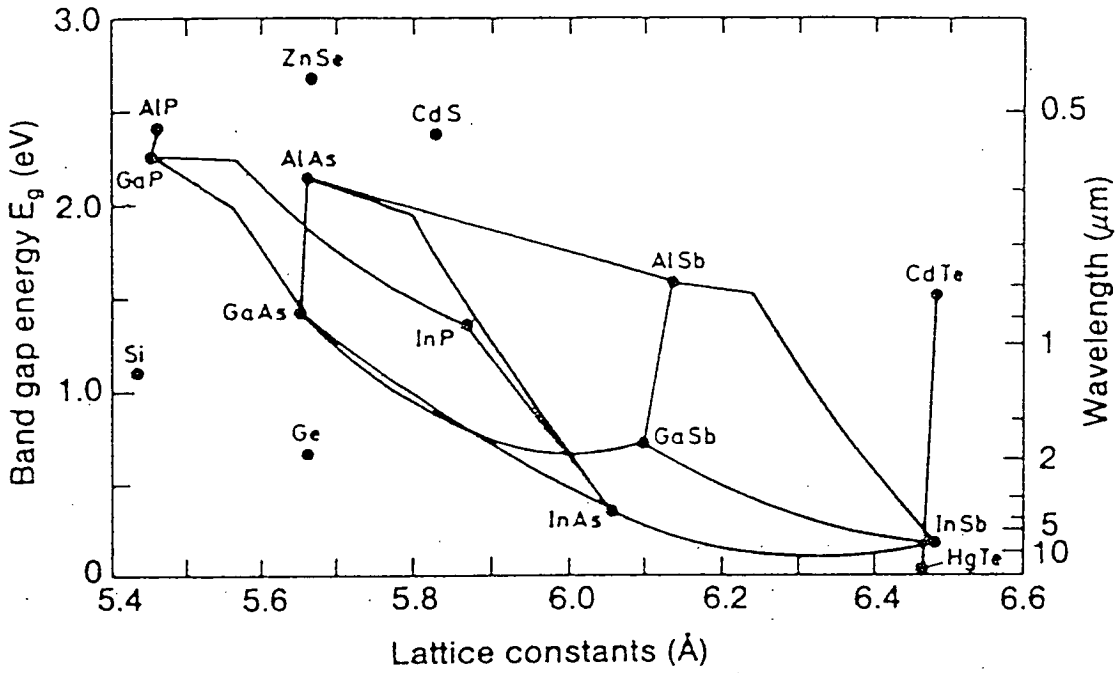

Figure 4.1 Bandgap of some important element and binary compound semiconductors plotted against the lattice parameter at 300K.[15]

When growing germanium epilayers on silicon substrates, the growth follows the Stranski-Krastanov model (2D layer-by-layer growth followed by 3D islanding) to relax the interface strain due to the lattice mis-match. At the early stage of growth, germanium atoms are found clustering and segregating on the top of the silicon substrates[16,17]. This problem also arises in the growth of Ge_xSi_{1-x}-Si hetrostructures. Interface segregation severely reduces the interface quality, which is strongly related to the strain and electron transport properties of the hetrostructures[18]. To overcome this problem, Copel et al. demonstrated the possibility of improving the interface morphology by passivating the silicon surfaces with a monolayer of arsenic acting as a surfactant (surface-active species) prior growth[19,20]. Antimony was also reported as a surfactant in Ge_xSi_{1-x} to growth[21,22]. It was found that the absorption of surfactant materials such as group V metals (Sb or As) can effectively passivate the dangling bounds of the silicon surface and reduce the surface free energy in Ge/Si growth[23,24].

As a result, the growth model is changed to that of layer-by-layer growth. Interface segregation is suppressed and sharp interfaces are formed.

In this chapter, the interface roughness of Ge_xSi_{1-x}-Si hetrostructures, grown with and without an antimony surfactant, were studied by glancing-incidence x-ray scattering. The results demonstrated that the surfactant efficiently improves the interface morphology as regards the RMS roughness and as regards the roughness exponent and correlation length. These results are being prepared for publication.

4.2 Experiment

4.2.1 Experimental details

Ge_xSi_{1-x} single-quantum-well hetrostructure samples grown on Si (100) single crystals were prepared by Molecular Beam Epitaxy (MBE) at the Institute of Physics, Chinese Academy of Science, Beijing, People's Republic of China, were studied by glancing-incidence x-ray scattering. After growth of a 1000Å silicon buffer layer, a 30Å $Ge_{0.1}Si_{0.9}$ layer was grown on sample A (sample number 940302-2) with a substrate temperature of 650°C. Then, the sample was capped by 300Å of silicon. Sample B (sample number 940302-1) was grown under identical conditions except a 0.75 monolayer of antimony was grown prior the growth of the $Ge_{0.1}Si_{0.9}$ layer as a surfactant. The details of the sample growth have been described elsewhere[25,26].

The samples were studied by glancing-incidence x-ray reflectivity at Station 2.3, at the Synchrotron Radiation Source, Daresbury Laboratory, using synchrotron radiation. Details of this station are given in Chapter 3 and in other references[27,28]. The wavelength was set to 1.200Å to optimise the x-ray intensity. Using a 100μm pre-sample slit and pre-detector slit, the angular resolution is on the order of 0.001°. Glancing-Incidence-X-ray-Reflectivity (GIXR) of both specular and off-specular scans was used to examine the samples. The theory of GIXR will be discussed later.

The Grazing Incidence X-Ray Scattering Software (GIXS) developed by Bede Scientific Instruments[29] was employed to simulate the scattering results and used to

fit to the experimental results thereby extracting the information on the interface roughnesses of the samples.

4.2.2 Glancing-incidence x-ray reflectivities

4.2.2.1 Specular reflectivity of perfect flat surfaces and interfaces

At glancing incident geometry, the scattering can be modelled by optical theories which neglect the crystal structure of the materials. This assumption is justified as long as the interatomic distances are much smaller than $\lambda/\sin\theta$, where λ is the wavelength of incident x-ray and θ is the incident angle. In this case, the refractive index of a material is

$$n = 1 - \delta - i\beta \tag{4.1}$$

$$\delta = \frac{N_A r_e \lambda^2 \rho}{2\pi M}(Z + f') \tag{4.2}$$

$$\beta = \frac{N_A r_e \lambda^2 \rho}{2\pi M} f'' = \frac{\lambda \rho \mu_\lambda}{4\pi} \tag{4.3}$$

where N_A is Avogadro's number, r_e is the classical electron radius. ρ, and M are the density and the atomic mass of the material respectively. μ_λ is the linear absorption coefficient of the material at wavelength λ. The atomic scattering factor can be written as

$$f = Z + f' + if'' \tag{4.4}$$

where Z is the atomic number of the material and f' and f'' are the real and imaginary parts of the dispersion corrections. In the x-ray region, where the wavelength is on the order of 1Å, both δ and β are small and have values about 10^{-6} and the refractive index, n, is just less than unity. As a result of Snell's law, total reflection occurs when the incident angle is smaller than the critical angle, θ_c, where

$$\theta_c = \sqrt{2\delta} \tag{4.5}$$

Typical values for the critical angle range from 0.1° to 0.3°, depending on the wavelength and the type of material. When the incident angle is below the critical angle, the x-rays hardly penetrate into the material. However, above this critical angle, penetration takes place and the reflectivity falls sharply. The amplitude of the reflected wave for a perfect interface is governed by Fresnel's laws.

Consider a system which many layers on top of a semi-infinite substrate, the electric fields, E, of the incident and reflected waves follow the pattern in Figure 4.2. The continuity of the tangential components of the electric fields across each interface leads to Parratt's recursive formula[3] for the reflection amplitudes, R

$$R_{j-1,j} = a_{j-1}^4 \left(\frac{R_{j,j+1} + r_{j-1,j}}{R_{j,j+1} + 1} \right) \tag{4.6}$$

where

$$R_{j,j+1} = a_j^2 \left(\frac{E^r{}_{j,j+1}}{E_{j,j+1}} \right) \tag{4.7}$$

$$r_{j-1,j} = \frac{f_{j-1} - f_j}{f_{j-1} + f_j} \tag{4.8}$$

$$a_j = \exp\left(-\frac{i\pi f_j t_j}{\lambda} \right) \tag{4.9}$$

and

$$f_j = \sqrt{\theta^2 - 2\delta_j - 2i\beta_j} \tag{4.10}$$

In these equations, $R_{j-1,j}$ is the reflection amplitude at the interface between the (j-1)-th layer and j-th layer. $r_{j-1,j}$ is the Fresnel coefficient at the interface with no roughness and a_j is the phase factor for half the thickness, t_j, of the j-th layer. Because the substrate is assumed to be infinitely thick and, therefore, has no reflected

wave in it, the recursive formula can be solved by starting at the substrate (layer N) with $R_{N,N+1} = 0$. The reflectivity of the sample is

$$R_{0,1} = \frac{E^r_{1,2}}{E_{1,2}} \tag{4.11}$$

and the reflected intensity is

$$\frac{I_R}{I_0} = |R_{1,2}| = \left|\frac{E^r_{1,2}}{E_{1,2}}\right|^2 \tag{4.12}$$

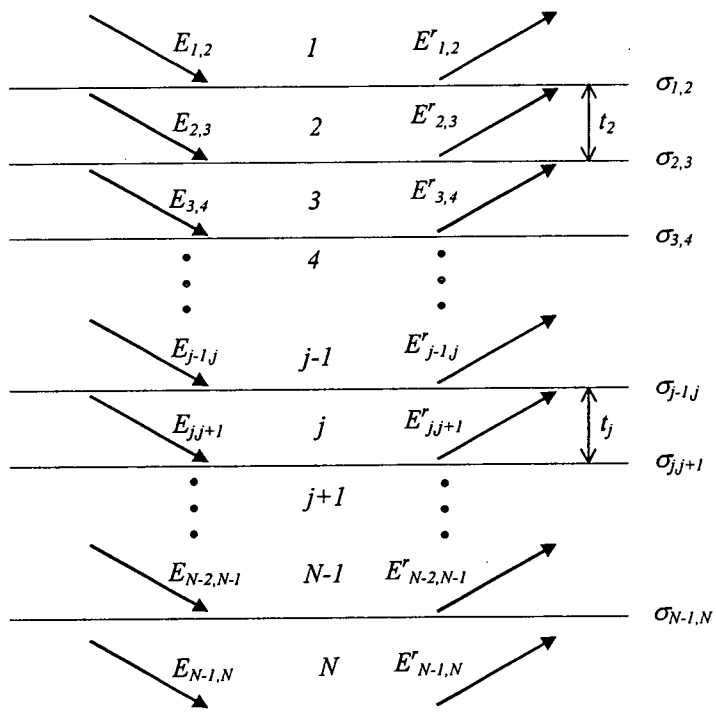

Figure 4.2 The electric fields in a multilayer structure.

4.2.2.2 Specular reflectivity of roughness surface and interface

The model established above is only valid for perfectly flat surfaces and interfaces. Real surfaces and interfaces, however, always have some roughnesses. The effect of roughness is to decrease the reflected intensity of the specular reflectivity profile and, in most cases, scatters the energy to off-specular directions, such as diffuse

scattering. The simplest way to model the rough interfaces is by separating the interface to a series of flat lamellae with slightly different electron density corresponding to the lateral averaging electron density of the rough interface at the same height.

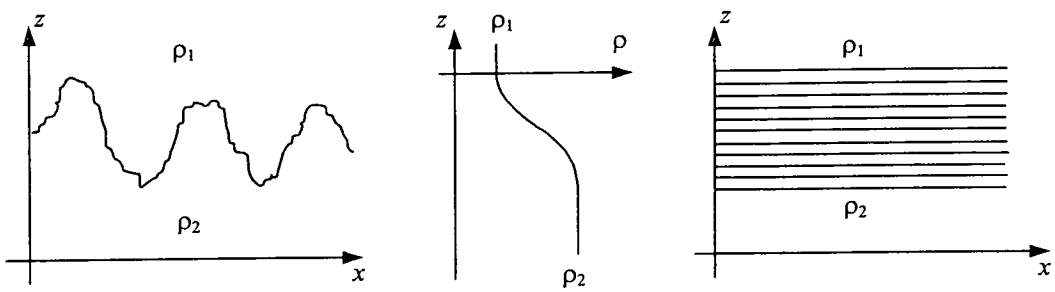

Figure 4.3 Model of rough interface for specular reflectivities. The real rough interface (left) can be modelled by a series of lamellae (right) with the same electron density profile (centre).

The most popular and realistic model of the electron density profile for rough interface is the Gaussian distribution,

$$\rho(z)=\frac{1}{\sqrt{2\pi\sigma^2}}\exp\left[-\frac{(z-z_0)^2}{2\sigma^2}\right] \tag{4.13}$$

where, z_0 is the average interface height, and σ is the root-mean-square (RMS) roughness

By using the Born approximation, an exponential damping factor is introduced into the Fresnel coefficient,

$$r_{j-1,j}=r_F\exp\left(-\tfrac{1}{2}\sigma_{j-1,j}{}^2Q_j{}^2\right) \tag{4.14}$$

where, r_F is the Fresnel coefficient in ideal case and Q_j is the momentum transfer vector

$$\vec{Q}=\vec{k}_f-\vec{k}_i$$

$$Q = 2k\sin\theta = \frac{4\pi}{\lambda}\sin\theta \tag{4.15}$$

As the Born approximation is invalid for calculating the reflectivity close to the total-external reflection critical angle, the Distorted Wave Born Approximation (DWBA) must be used. The Fresnel coefficient is corrected as

$$\begin{aligned} r_{j-1,j} &= r_F \exp\left(-\tfrac{1}{2}\sigma_{j-1,j}{}^2 Q_j Q_{j-1}\right) \\ &= \left(\frac{f_{j-1}-f_j}{f_{j-1}+f_j}\right)\exp\left(-\tfrac{1}{2}\sigma_{j-1,j}{}^2 Q_j Q_{j-1}\right) \end{aligned} \tag{4.16}$$

4.2.2.3 Diffuse scattering and self-affine surface/interface

By laterally averaging the electron density of rough surfaces/interfaces, the specular reflectivity can be calculated simply. However, because of the averaging, the two-dimensional interface structure was neglected except the RMS roughness. To reveal the true morphology of the interface, diffuse scattering has to be fitted simultaneously.

Self-affine fractals are widely used to describe the rough surface and have achieved remarkable success[12]. Unlike self-similar fractals with isotropic scaling behaviour, the self-affine fractal has an anisotropic scale transformation[30].

$$z(x) \sim b^{-\alpha} z(bx) \tag{4.17}$$

Here, z is the height of the surface/interface and α is the roughness exponent. The self-affine function is rescaled in a different way horizontally and vertically. The height difference correlation function follows a power law,

$$g(X,Y) \equiv \left\langle [z(R) - z(0)]^2 \right\rangle = AR^{2\alpha} \tag{4.18}$$

where $R = \sqrt{X^2 + Y^2}$ is the separation of the observation points.

Sinha et al.[10] extended this concept and introduced a more realistic form of the height difference correlation function with cut-off

$$g(X,Y)=g(R)=2\sigma^2\left[1-\exp\left(-\left(R/\xi\right)^{2h}\right)\right] \tag{4.19}$$

where σ is the RMS roughness of the surface/interface which shows the "width" of the interface. h is the fractal exponent which varies between 0 and 1, and is a measurement of how jagged or smooth a rough interface is: $h\approx 1$ denotes the interface is very smooth and $h\approx 0$ denotes a very jagged interface. ξ is the lateral correlation length of the roughness. The equation shows self-affine fractal behaviour for $R<<\xi$, but saturates to a special RMS roughness for $R>>\xi$. As a result, ξ gives a cut-off length between the regimes of self-affinity and saturation.

The height-height correlation function is

$$\begin{aligned} C(X,Y) &\equiv \langle z(X,Y)-z(0,0)\rangle \\ &= \sigma^2-\frac{1}{2}g(X,Y) \\ &= \sigma^2\exp\left[-\left(\frac{R}{\xi}\right)^{2h}\right] \end{aligned} \tag{4.20}$$

We define the power spectrum

$$S(\mathbf{q})=\frac{d\sigma}{d\Omega}\frac{1}{N^2b^2L_xL_y} \tag{4.21}$$

where $\frac{d\sigma}{d\Omega}$ is the differential cross section, N is the scattering particle density and b is the scattering length which is the Thompson scattering length of the electron ($b=e^2/mc^2$) for x-ray scattering experiments. The product L_xL_y is the area of illumination on the sample surface.

From the Born approximation, the power spectrum can be calculated[10]

$$S(\mathbf{q})=\frac{1}{q_z^{\,2}}e^{-q_z^{\,2}\sigma^2}\iint_{S_0}dXdYe^{q_z^{\,2}C(X,Y)}e^{-i(q_xX+q_yY)} \tag{4.22}$$

We further define

$$F(q_z, R) \equiv e^{q_z^2 C(X,Y)} - 1 \tag{4.23}$$

and note that when $R \to \infty$, $F \to 0$. The power spectrum can be separated into a specular and a diffuse part.

$$S(\mathbf{q}) = S_{spec}(\mathbf{q}) + S_{diff}(\mathbf{q}) \tag{4.24}$$

where

$$S_{spec}(\mathbf{q}) = \frac{4\pi^2}{q_z^2} e^{-q_z^2\sigma^2} \delta(x)\delta(y) \tag{4.25}$$

and

$$S_{diff}(\mathbf{q}) = \frac{2\pi^2}{q_z^2} e^{-q_z^2\sigma^2} \int_0^\infty dR R F(q_z, R) J_0(q_r, R) \tag{4.26}$$

$J_\nu(x)$ is the Bessel function.

The delta functions in equation (4.25) show that the specular part of scattering forms a very sharp ridge along the z direction which is the surface normal direction.

The power spectrum of the diffuse scattering in (4.26) was derived from the Born approximation which is not correct at small angles. To obtain the correct form of the differential cross section, the Distorted Wave Born Approximation should be applied.

$$\left.\frac{d\sigma}{d\Omega}\right|_{diff} = (L_x L_y) \frac{\left|k_0^2(1-n^2)\right|^2}{16\pi^2} |T(k_1)|^2 |T(k_2)|^2 S(q_t) \tag{4.27}$$

$$S(q_t) = \frac{\exp\left\{-\left(\sigma^2/2\right)\left[\left(q_z^{\,t}\right)^2 + \left(q_z^{\,t^*}\right)^2\right]\right\}}{\left|q_z^{\,t}\right|^2} \iint_{S_0} dX dY \left[e^{\left|q_z^{\,t}\right|^2 C(X,Y)} - 1\right] e^{i(q_x X + q_y Y)} \tag{4.28}$$

When the incident, or take-off, angle of the scattering matches the critical angle of the material, the differential cross section will reach a local maximum because either $|T(k_1)|$ or $|T(k_2)|$ reaches its local maximum. At this moment, the diffuse scattering will shows a peak which is the Yoneda wing.

4.2.2.4 Correlated and Un-correlated roughness in a multilayer system

For a multilayer system, the scattering from different interfaces interfere with each other. The height-height correlation function should be modified as

$$C_{l,l'}(X,Y) = \langle z_l(0,0) z_l(X,Y) \rangle \equiv \sigma_{l,l'}{}^2 \exp\left[-\left(\frac{\sqrt{X^2+Y^2}}{\xi} \right)^{2h} \right] \tag{4.29}$$

where $z_l(X,Y)$ is the height of the l-th interface of the system from the average location of the interface at the co-ordinate (X,Y). h is the fractal exponent of the system and ξ is its correlation length. To simplify the calculation, the surface and all interfaces were assumed to have similar fractal morphology which can be described by single set of fractal parameters.

The RMS roughness can be separated into two parts: uncorrelated roughness and correlated roughness.

$$\sigma_{l,l'}{}^2 \equiv (\sigma_l)_u (\sigma_{l'})_u \delta_{l,l'} + (\sigma_l)_c (\sigma_{l'})_c \tag{4.30}$$

$(\sigma_l)_u$ and $(\sigma_l)_c$ is the uncorrelated and correlated roughness of l-th interface respectively. $\delta_{l,l'}$ is the Kronecker delta function. The correlated roughness are replicated from layer to layer so they can interfere with each other. However, the uncorrelated roughness is not replicated. Under these definitions, the RMS roughness of l-th interface is

$$\sigma_l{}^2 \equiv (\sigma_l)_u{}^2 + (\sigma_l)_c{}^2 \tag{4.31}$$

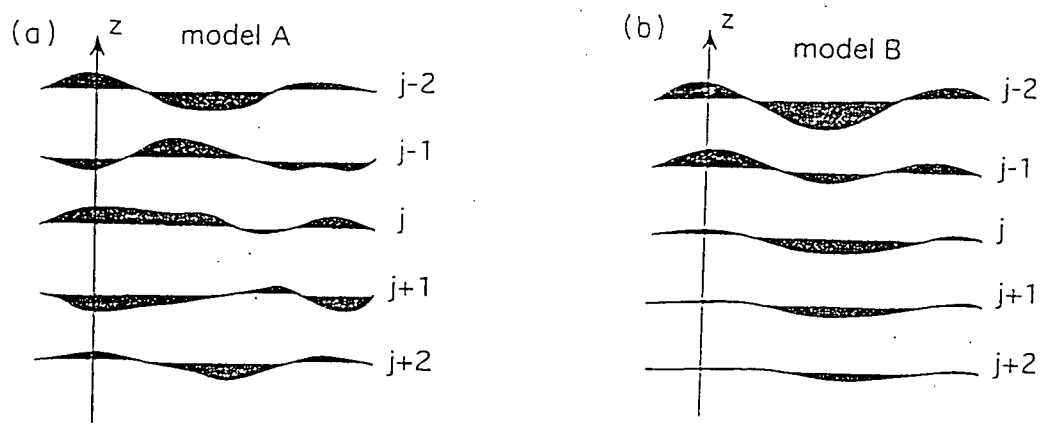

Figure 4.4 Model of (a) uncorrelated and (b) partially correlated interface roughness.

4.3 Experimental Results

4.3.1 Sample A: $Si/Ge_{0.1}Si_{0.9}/Si$ grown without surfactant

Figure 4.5 shows the specular reflectivity profile of sample A which was grown without any surfactant. The best fit of the simulation, by the GIXS program, gave the surface and interface roughness parameters shown in Table 4.1. The $Ge_{0.1}Si_{0.9}$ layer was found to be thicker than the growth prediction of 30Å, and with a lower density ($\rho=0.93\rho_0$) and the interface roughnesses above and below this layer are large (10Å). This is evidence that the layer is suffering from interface segregation and inter-diffusion. An oxide layer of 36Å was found on the top of the sample with very low density and high surface roughness which might be due to large dislocation density or even amorphous material. Because of the large roughness on the surface, the reflectivity drops very fast. At $\theta > 1.0°$, the reflectivity is close to the background, which causes a poor fit.

Table 4.1 The structure parameters of each layer of the best fit from GIXS simulation

Materials	Density[31]	Thickness	Roughness
SiO_2	0.58±0.02	36±1 Å	28±0.5 Å
Si	1.00±0.02	298±1 Å	12±0.5 Å
$Ge_{0.1}Si_{0.9}$	0.93±0.02	49±1 Å	10±1.0 Å
Si	1.00±0.02	Substrate	10±2.0 Å

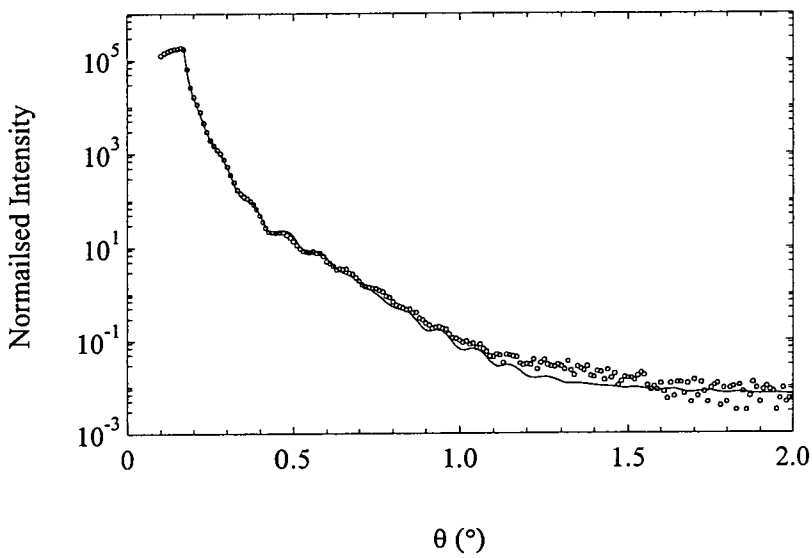

Figure 4.5 The specular reflectivity profile from sample A and the best fit of the simulation with the parameters shown in Table 4.1.

The transverse scan of this sample (Figure 4.6) was taken by performing a rocking-curve scan when 2θ was set to be 1.60°. The best fit of the simulation result gave the lateral correlation length and the fractal exponent of the surface/interfaces shown in Table 4.2. Figure 4.7 shows the longitudinal scan which was taken by performing an ω-2θ coupled scan with an offset angle δ=+0.1° added to ω angle. To achieve an adequate fit, the roughnesses had to be correlated with each other. The simulation result is also shown in Figure 4.7.The fits of transverse and offset longitudinal scans are found to be much poorer than specular reflectivity. This is possibly due to the over-simplified roughness model in the simulation. The surface and interface

Table 4.2 The surface/interface parameters for self-affine fractal model

Lateral correlation length	Fractal exponent
2800±300 Å	0.45±0.05

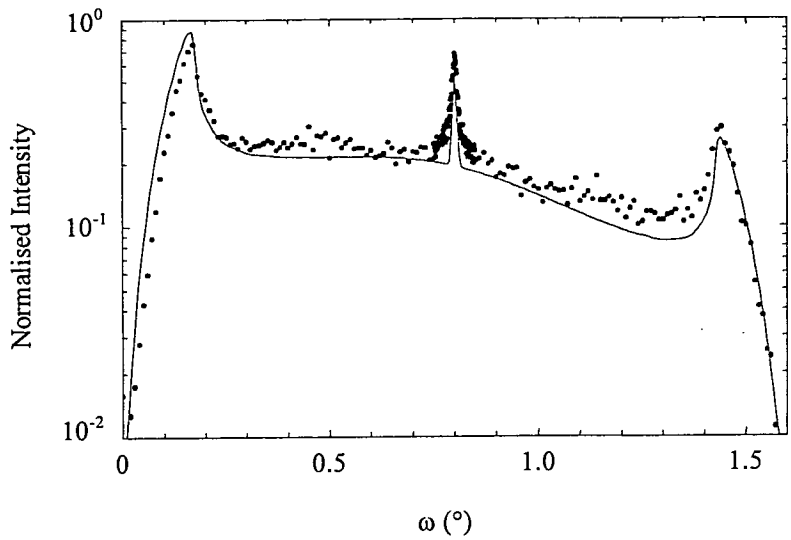

Figure 4.6 The transverse diffuse scan profile at 2θ=1.6° and the best fit of the simulation with the interfaces parameters given in both Table 4.1 and Table 4.2.

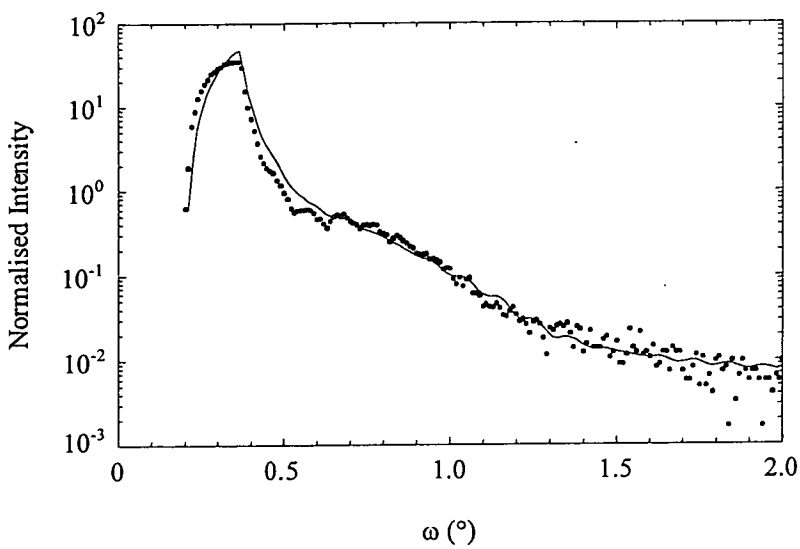

Figure 4.7 The longitudinal scan with offset angle δ=+0.1° and the best fit of the simulation.

The fits of transverse and offset longitudinal scans are to be found much poorer than the specular reflectivity. This is possibly due to the over-simplified roughness model in the simulation. This will be discussed further later.

4.3.2 Sample B: $Si/Ge_{0.1}Si_{0.9}/Si$ grown with antimony as a surfactant

Figure 4.8 shows the specular reflectivity profile of sample B which was grown with a 0.75 mono-layer of antimony on the substrate prior to the $Ge_{0.1}Si_{0.9}$ alloy growth. The reflectivity showed that the intensity contrast of the fringes was far more pronounced at all angles than the corresponding sample A (Figure 4.5). The best fit of the GIXS simulation gave the surface and interface roughnesses as given in Table 4.3. The $Ge_{0.1}Si_{0.9}$ layer was found to be closer to the growers estimated thickness of 30Å (32Å) and the density was very close to unity ($\rho=0.98\rho_0$). All of the interface roughnesses were found to be much smaller than the corresponding values for sample A. These facts demonstrate that the surfactant is efficiently smoothing the interface roughness. The low-density surface oxidation layer is also found with similar thickness and density as the one in sample A. However, the surface roughness is much smaller.

Table 4.3 The structure parameters of each layer of the best fit

Materials	Density	Thickness	Roughness
SiO_2	0.64±0.02	32±1 Å	8.5±0.5 Å
Si	1.00±0.02	296±1 Å	5±0.5 Å
$Ge_{0.1}Si_{0.9}$	0.98±0.02	32±1 Å	6±1.0 Å
Si	1.00±0.02	Substrate	4±3.0 Å

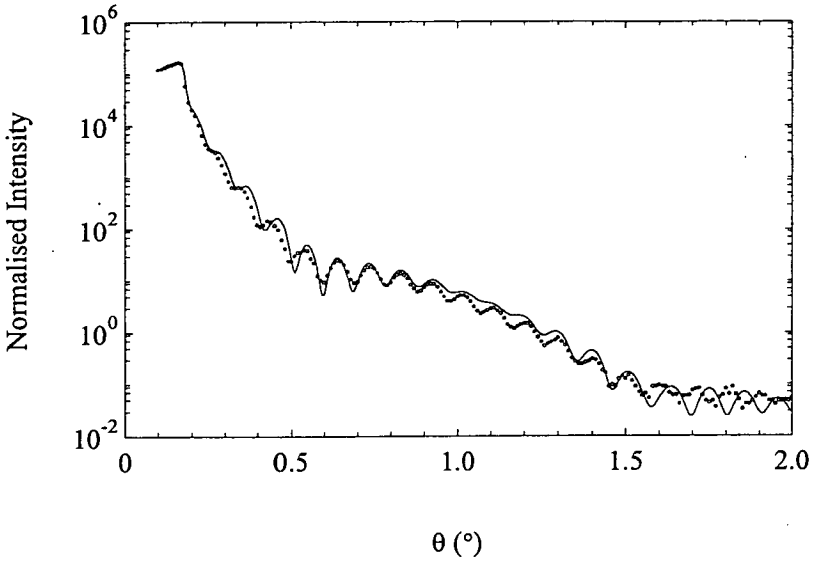

Figure 4.8 The specular reflectivity profile from sample A and the best fit of the simulation with the parameters shown in Table 4.3.

The transverse scan (Figure 4.9) was taken with 2θ=1.66°. The specular "ridge" is unclear and a huge diffuse scattering component was observed. The best fit of the simulation result gave an enormous lateral correlation length and a larger fractal exponent which are given in Table 4.4. This result shows that the effect of the surfactant is to not only to reduce the interface RMS roughness but also to smooth the interface. Generally speaking, the correlation length is the distance between successive crossings of the surface profile through some set level (for example, the zeroset of the average surface) regardless of the high-frequency fluctuation[32,33]. It is clear that the interfaces grown with surfactant become smooth at very small length scale but comparatively rough at a micron length scale.

Table 4.4 The surface/interface parameters for self-affine fractal model

Lateral correlation length	Fractal exponent
20000±2000 Å	0.58±0.05

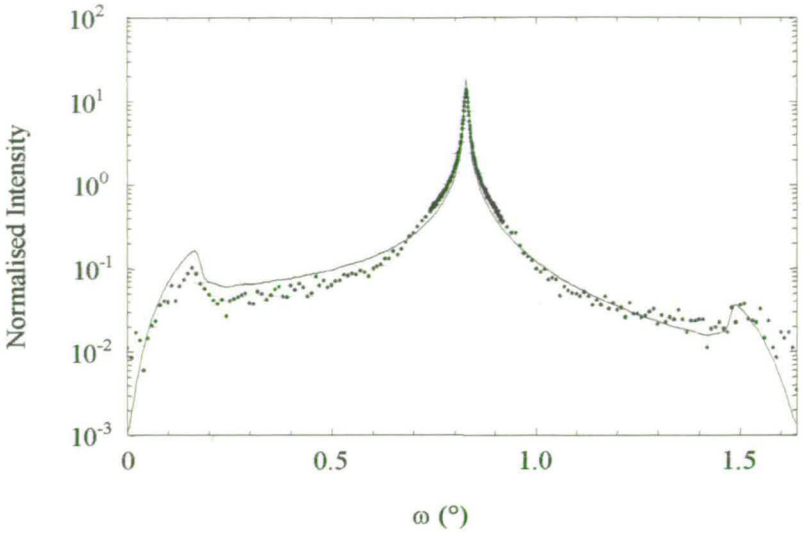

Figure 4.9 The transverse diffuse scan profile at 2θ=1.6° and the best fit of the simulation with the interfaces parameters in both Table 4.3 and Table 4.4.

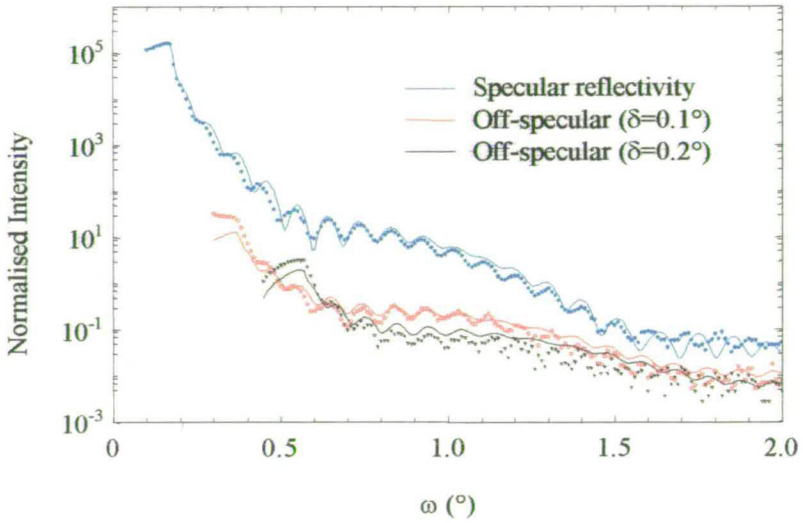

Figure 4.10 The longitudinal scans with offset angle δ=0° (specular reflectivity), 0.1° and 0.2°. The best fits of the simulations are also shown.

The longitudinal scans with offset angles 0.1° and 0.2° are shown in Figure 4.10. The specular reflectivity is also shown in the same figure for comparison. Kiessig fringes are clearly observed in both the specular and off-specular directions, with the same frequency, which shows that the interface roughnesses are replicated over layers and strongly correlated with each other. The best fits of the longitudinal scans are

presented in the Figure. The adequate fit confirms the structure parameters are substantially correct.

4.4 Discussion and Conclusion

The glancing-incidence x-ray scattering results reveal the completely different interface morphology of GeSi heterostructures grown with and without surfactant. When grown with 0.75 monolayer Sb prior to thin film growth, the roughnesses of the interfaces are dramatically reduced and the density of the $Ge_{0.1}Si_{0.9}$ layer is found to be close to unity. This is the direct evidence that the existence of surfactant effectively suppresses the segregation and the inter-diffusion on the interface and helps to form sharper interfaces.

When fitting the transverse or offset longitudinal scan profiles, we found that it is very difficult to reach perfect fits. This could be due to the individuality of the interfaces. In the simulation, the vertical correlation length is assumed to be large and, therefore, the lateral correlation length and the fractal exponent are set to be identical for all interfaces. When the vertical correlation is short, each interface should have individual parameters. At least, this is obvious that the surface of oxidation layer should have different morphology from other interface because of the different growth mechanism. In Figure 4.6, for example, the small shoulder on both side of the specular ridge suggests that part of the film might have longer lateral correlation length than others. However, this will dramatically increase the calculation time and it is impossible to resolve the structure within reasonable time.

By comparing our results to the ones reported by Cui et al. on GeSi superlattices[26], the magnitude of roughnesses and their exponents are close. However, the lateral correlation length is much larger in our samples, both grown with and without a surfactant. Perhaps, the smaller correlation length of superlattices is due to the averaging of non-identical interfaces. In other words, the vertical correlation might not be as good as that they expected.

The surfactant also changes the interface morphology. The existence of the Sb surfactant gives a micron-size correlation length and a larger fractal exponent which suggest the interface is very smooth at small lengthscale.

---

[1] A.H.Compton, Philos. Mag. **45**, 1121 (1923)

[2] H.Kiessig, Ann. Phys. **10**, 715 (1931)

[3] L.G.Parratt, Phys. Rev. **95**, 395 (1954)

[4] Y.Yoneda, Phys. Rev. **131**, 2010 (1963)

[5] P.Croce, L.Nevot, and B.Pardo, C. R. Hebd. Sean. Acad. Sci. B **274**, 803 (1972)

[6] P.Croce, and L.Nevot, Revue Phys. Appl. **11**, 113 (1976)

[7] L.Nevot, and P.Croce, Revue Phys. Appl. **15**, 761 (1980)

[8] L.H.Schwartz, and J.B.Cohen, *Diffraction from Material* (Spring-Verlag, Berlin, 1987)

[9] A.G.Michette, and C.J.Buckley, *X-ray Science and Technology* (Institute of Physics, Bristol, 1993)

[10] S.K.Sinha, E.B.Sirota, S.Garoff, and H.B.Stanley, Phys. Rev. B **38**, 2297 (1988)

[11] G.H.Vineyard, Phys. Rev. B **26**, 4146 (1982)

[12] B.B.Mandelbrot, *The Fractal Geometry of Nature* (Freeman, New York, 1982)

[13] V.Holy, J.Kubena, I.Ohlidal, K.Lischka, and W.Plotz, Phys. Rev. B **47**, 15896 (1993)

[14] V.Holy, and T.Baumbach, Phys. Rev. B **49**, 10668 (1994)

[15] H.Ibach, and H.Luth, *Solid-State Physics* (Springer-Verlag, Berlin, 1991)

[16] D.J.Eaglesham, and M.Cerullo, Phys. Rev. Lett. **64**, 1943 (1990)

[17] Y.-W.Mo, D.E.Savage, B.S.Swartzentruber, and M.G.Lagally, Phys. Rev. Lett. **65**, 1020 (1990)

[18] G.C.Osbourn, J. Vac. Sci. Technol. B **2**, 176 (1984)

[19] M.Copel, M.C.Reuter, E. Kaxiras, and R.M.Tromp, Phys. Rev. Lett. **63**, 632 (1989)

[20] M.Copel, M.C.Reuter, M. Horn von Hoegen, and R.M.Tromp, Phys. Rev. B **42**, 11682 (1990)

[21] J.M.C.Thornton, A.A.Williams, J.E.Macdonald, R.G.van Silfhout, J.F.van der Veen, M.Finney, and C.Norris, J. Vac. Sci. Technol. B **9**, 2146 (1991)

[22] A.A.Williams, J.M.C.Thornton, J.E.Macdonald, R.G.van Silfhout, J.F.van der Veen, M.Finney, A.D.Johnson, and C.Norris, Phys. Rev. B **43**, 5001 (1991)

[23] S.Hasegawa, R.G.Ryland, and E.D.Williams, Appl. Phys. Lett. **65**, 2609 (1994)

[24] C.W.Oh, E.Kim, and Y.H.Lee, Phys. Rev. Lett. **76**, 776 (1996)

[25] M.Li, Q.Cui, S.F.Cui, L.Zhang, J.M.Zhou, Z.M.Mai, C.Dong, H.Chen, and F.Wu, J. Appl. Phys. **78**, 1681 (1995)

[26] S.F.Cui, G.M.Luo, M.Li, Z.H.Mai, Q.Cui, J.M.Zhou, X.M.Jiang, and W.L.Zhang, J. Phys.: Condens. Matter **9**, 2891 (1997)

[27] R.J.Cernik, P.K.Murray, P.Pattison, and A.N.Fitch, J. Appl. Cryst. **23**, 292 (1990)

[28] S.P.Collins, R.J.Cernik, P.Pattison, A.M.T.Bell, and A.N.Fitch, Rev. Sci. Instrum. **63**, 1013 (1992)

[29] Bede Scientific Instruments Ltd., *Grazing Incidence X-ray Scattering Software* (1995)

[30] A.-L.Barabási, H.E.Stanley, *Fractal Concepts in Surface Growth* (Cambridge University Press, 1995)

[31] The density here means the relative mass density to the corresponding material in first column.

[32] E.L.Church, Proc. SPIE **680**, 102 (1986)

[33] J.C.Russ, *Fractal Surfaces* (Plenum Press, New York, 1994)

Chapter 5

High-Resolution X-ray Scattering Studies of $YBa_2Cu_3O_{7-\delta}$ Thin Film High-T_c Superconductors

5.1 Introduction

The discovery of high-T_c superconductivity in the late 1980's redirected the interest of much scientific research. After a decade's study, however, its nature is still undetermined. One of the major problems encountered was the complexity of the materials. This complexity often caused specimens to be extremely sensitive to small variations in their composition with resultant effects on their quality, making the fabrication of high-T_c superconductors problematic. Therefore, it is important to control the fabrication processes to ensure the properties of the material are mentioned. A proper testing technique, such as high-resolution x-ray scattering, is the first step to understanding and controlling of the fabrication process.

In this chapter, routine testing using high-resolution x-ray scattering will be performed on various $YBa_2Cu_3O_{7-\delta}$ thin films. The results give an overall indication on the quality of the samples. This measurement is widely employed in determining the sample structure.

5.2 High-T_c thin film superconductors

5.2.1 Superconductivity

Superconductivity was first discovered by a Dutch physicist, H. Kamerlingh-Onnes, in 1911, three years after he first liquefied helium. When Onnes tried to measure the electrical resistance of mercury at very low temperatures, he found that the resistance of pure mercury fell below 10^{-5} Ω (the experimental detection limit at that time) for temperatures below 4.15 K. Afterwards, new superconducting materials including pure elements and alloys were discovered. The highest superconducting transition temperature (T_c), until the recent discovery of high temperature superconductors, was Nb_3Ge with T_c=23.2 K[1].

One of the most important aspects about superconductivity is absence of resistivity. When a material is in superconducting state, the DC electric resistance is zero. The resistance is so low that it is impossible to measure it using Ohm's law, or by current-voltage measurement. File and Mills studied the decay of the current in a superconducting solenoid and concluded that the decay time of this supercurrent is not less than 100,000 years[2].

Another important phenomenon related to superconductivity is the *Meissner effect*. When a specimen is cooled down to its transition temperature and becomes superconducting, any constant, but not too strong, magnetic field will be forced out of it. This effect was first observed and reported in 1933 by two German physicists, W. Meissner and R. Ochsenfeld[3]. When external magnetic fields are applied to a superconducting sample, supercurrents are induced in a thin layer under the sample surface. The supercurrents screen the interior of the sample against external fields. Therefore, the fields decay with depth exponentially with a characteristic length, known as the *London penetration depth*, named after F. London and H. London who first gave the theoretical explanation of the Meissner effect in 1935[4]. In 1950, L. D. Landau and V. L. Ginzburg gave a more general theory of superconductivity.

By then, the London equations and the Landau-Ginzburg equations were both phenomenological equations. In 1957, a successful quantum theory of superconductivity, which explained the mechanism of superconductivity, was given by three American physicists, J. Bardeen, L. Cooper, and J. R. Schrieffer[5]. This theory is now generally referred to as the BCS theory. In this theory, it is assumed that the electron pairs bound by the electron-phonon interaction carry the supercurrent and an energy gap between the normal and superconducting states is then created. The paired electrons are known as *Cooper pairs* since the idea was suggested by Cooper. The mean distance between coupled electrons in a pair is called the *correlation length.* Table 5.1 shows the superconducting transition temperature (T_c), London penetration depth (λ) and coherence length (ξ) of some superconductors. The BCS theory has been well accepted in explaining conventional superconductivity (T_c below ~30K).

Table 5.1 Superconducting transition temperature (T_c), London penetration depth (λ) and coherence length (ξ) of various superconductors[1]

Materials	T_c (K)	λ(Å)	ξ(Å)
Sn	3.72	420	1800
Pb	7.20	390	820
Nb	9.25	500	390
Nb_3Sn	18	650	30
Nb_3Ge	23.2	900	30
$YBa_2Cu_3O_{7-\delta}$ (a-b)	89	260	34
$YBa_2Cu_3O_{7-\delta}$ (c)	89	1250	7

5.2.2 $YBa_2Cu_3O_{7-\delta}$ high-T_c superconductors

Since 1930, the element niobium and its compounds dominated the field of superconductivity for the next 56 years. These materials have not only the highest T_c values but also have high critical magnetic fields. In 1986, there was a dramatic breakthrough when J. G. Bednorz and K. A. Muller discovered a new class of so-called high-temperature superconducting substances[6]. They found that $La_{2-x}Ba_xCuO_4$

had a T_c of about 35 K for $x \approx 0.15$. They described their samples as "metallic, oxygen-deficient, perovskite-like mixed-valence copper compounds". This discovery made a new record of the highest T_c and initiated the "Copper Oxide Era of superconductivity" [1].

After the discovery by Bednorz and Mullers, new superconducting compounds were quickly found one after another and the highest T_c of the new superconductors climbed ever higher. In 1987, Chu et al.[7] reported their discovery of $YBa_2Cu_3O_{7-\delta}$ with $T_c \approx 92$ K. This was another important breakthrough because it was the first time that the superconducting transition temperature (T_c) was higher than 77 K, the boiling temperature of liquid nitrogen. This would have profound consequences on the economics of employing superconducting materials. In 1988, BiSrCaCuO compounds were found with $T_c \approx 110$ K by many different groups. The T_c of TlBaCaCuO compounds were found to be even higher, about 120-125 K. Researchers continue to look for new high-T_c superconducting materials with higher transition temperatures.

The compound $YBa_2Cu_3O_7$, sometimes refers to as the 123 compound, has an orthorhombic or tetragonal structure as shown in Figure 5.1. Its unit cell can be derived from the perovskite structure ABO_3 by tripling one cell axis concurrent with the cation ordering –Y–Ba–Ba–Y–Ba–Ba– on an A site (hence the name "triple perovskite" structure) and by removing three (out of nine) oxygen atoms. Oxygen deficiency is often found in $YBa_2Cu_3O_7$ and therefore the compounds are written as $YBa_2Cu_3O_{7-\delta}$. For $0<\delta<0.6$, $YBa_2Cu_3O_{7-\delta}$ is orthorhombic and superconducting at low temperature, and for $0.6<\delta<1$, it is tetragonal. The T_c also depends on the oxygen deficiency and the highest T_c of these compounds is about 90 K when $0<\delta<0.2$. The structural data for $YBa_2Cu_3O_{6.91}$ is listed in Table 5.2[8,9].

Figure 5.2 shows the diffraction pattern of $YBa_2Cu_3O_{6.91}$ along *a-b* plane and the major diffraction maxima are listed in Table 5.3. The diffraction pattern of $YBa_2Cu_3O_{6.91}$ was calculated using the commercial Cerius program[10] with the structural data of Table 5.2.

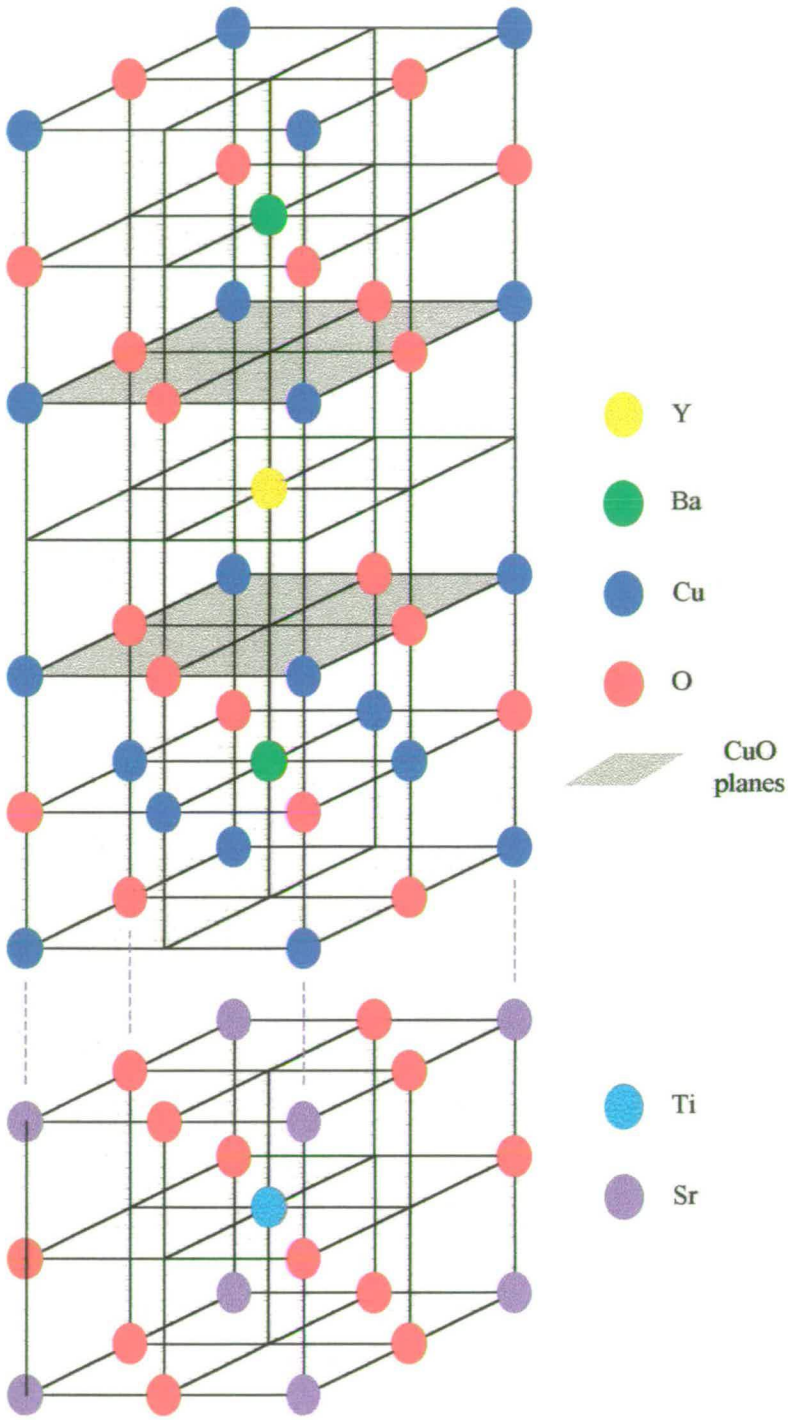

Figure 5.1 A *c*-oriented $YBa_2Cu_3O_7$ unit cell and a $SrTiO_3$ substrate unit cell. The dotted lines show how the $YBa_2Cu_3O_7$ film epitaxial grows on a typical perovskite substrate such as $SrTiO_3$.

Table 5.2 Structure data for $YBa_2Cu_3O_{6.91}$[9]

Space group : *Pmmm* (No. 47) T_c=95K

Lattice parameters : *a=3.8177*Å *b=3.8836*Å *c=11.6827*Å

$\alpha=\beta=\gamma=90°$

Element	Wyckoff position	x	y	z	Debye Waller factor	Occupancy
Y	(1h)	0.5	0.5	0.5	0.49	1.00
Ba	(2t)	0.5	0.5	0.1844	0.64	1.00
Cu (1)	(1a)	0	0	0	0.51	1.00
Cu (2)	(2q)	0	0	0.3552	0.52	1.00
O (1)	(2q)	0	0	0.1588	0.75	1.00
O (2)	(2s)	0.5	0	0.3779	0.62	1.00
O (3)	(2r)	0	0.5	0.3780	0.64	1.00
O (4)	(1e)	0	0.5	0	1.12	0.91

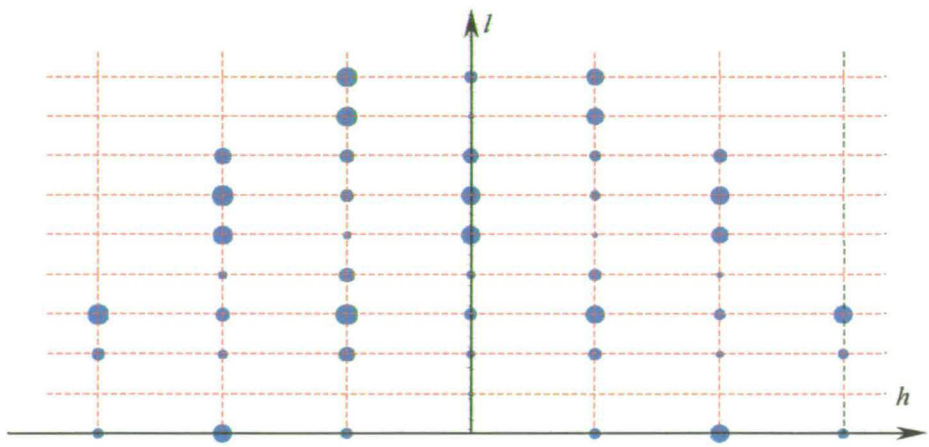

Figure 5.2 The x-ray diffraction pattern (a-b plane) of $YBa_2Cu_3O_{6.91}$ from the Cerius simulation[10]. The size of the spots is proportional to the integrated intensity of the Bragg reflections.

Table 5.3 The major diffraction maxima of $YBa_2Cu_3O_{6.91}$ obtained from a Cerius simulation. The on-axis reflections (along [001] direction) are highlighted.

h	k	l	d-spacing	2θ	Integrated Intensity	
2	0	0	1.9089	47.598	42121.4	98.40%
1	0	3	2.7262	32.825	32291.4	75.44%
0	0	6	1.9471	46.607	23841.2	55.70%
4	0	0	0.9544	107.620	17642.6	41.22%
2	0	6	1.3631	68.818	16586.7	38.75%
3	0	3	1.2096	79.107	16383.5	38.27%
0	0	5	2.3365	38.497	10404.9	24.31%
4	0	6	0.8570	128.003	8806.70	20.57%
0	0	11	1.0621	92.982	7429.34	17.36%
1	0	8	1.3640	68.769	7140.05	16.68%
1	0	9	1.2290	77.624	6931.83	16.19%
2	0	5	1.4783	62.809	6485.14	15.15%
2	0	11	0.9281	112.191	6014.69	14.05%
1	0	10	1.1171	87.184	5299.40	12.38%
3	0	9	0.9087	115.914	4689.33	10.96%
3	0	8	0.9594	106.811	4464.30	10.43%
0	0	7	1.6690	54.972	4335.41	10.13%
1	0	13	0.8748	123.421	3921.18	9.16%
3	0	10	0.8606	127.029	3737.24	8.73%
0	0	13	0.8987	117.993	3239.94	7.57%
2	0	7	1.2564	75.623	3222.08	7.53%
4	0	5	0.8836	121.336	3076.80	7.19%
0	0	9	1.2981	72.797	2070.85	4.84%
1	0	2	3.1957	27.895	2037.40	4.76%
0	0	10	1.1683	82.498	1978.33	4.62%
4	0	7	0.8285	136.780	1846.18	4.31%
1	0	4	2.3197	38.788	1829.14	4.27%

0	0	3	3.8942	22.817	1766.13	4.13%
0	0	12	0.9736	104.596	1763.71	4.12%
2	0	10	0.9965	101.252	1706.55	3.99%
2	0	9	1.0734	91.715	1693.31	3.96%
2	0	12	0.8673	125.287	1505.58	3.52%
2	0	3	1.7140	53.411	1347.31	3.15%
1	0	7	1.5292	60.491	1205.48	2.82%
1	0	0	3.8177	23.280	1161.54	2.71%
4	0	3	0.9270	112.393	1149.39	2.69%
3	0	0	1.2726	74.500	1050.15	2.45%
3	0	2	1.2434	76.558	987.78	2.31%
3	0	4	1.1666	82.639	907.841	2.12%
1	0	6	1.7345	52.729	823.246	1.92%
3	0	6	1.0652	92.623	822.807	1.92%
3	0	7	1.0120	99.137	777.207	1.82%
0	0	4	2.9207	30.583	434.714	1.02%
0	0	2	5.8414	15.155	356.526	0.83%
1	0	12	0.9434	109.476	271.900	0.64%
2	0	2	1.8144	50.242	231.609	0.54%
4	0	2	0.9419	109.723	154.779	0.36%
2	0	4	1.5979	57.642	140.831	0.33%
3	0	5	1.1176	87.142	114.921	0.27%
1	0	5	1.9929	45.475	78.7597	0.18%
0	0	8	1.4603	63.669	61.7144	0.14%
0	0	1	11.6827	7.561	59.6101	0.14%
2	0	1	1.8839	48.269	18.1570	0.04%
4	0	4	0.9072	116.22	15.2812	0.04%
2	0	8	1.1598	83.23	9.51361	0.02%
1	0	1	3.6289	24.51	3.68249	0.01%
3	0	1	1.2651	75.017	3.17492	0.01%
4	0	1	0.9513	108.143	2.15504	0.01%

Like conventional (low T_c) superconductors, most experimental results have showed that the charge carriers in high-T_c superconductors are pairing electrons. According to the BCS theory, the attractive electron-pairing interaction is due to electron-phonon coupling. In the high-T_c superconductors, however, the electron-phonon-coupling interaction is not strong enough to account for the high transition temperatures. So far, the mechanism of high temperature superconductivity is still unclear.

5.2.3 Superconducting thin films

Soon after the discovery of superconducting behaviour above liquid-nitrogen temperature in $YBa_2Cu_3O_{7-\delta}$, the growth of this material in thin film form was reported. Generally speaking, due to the highly anisotropic structure and the very short coherence length of the oxide superconductors, superconducting properties of thin film samples is normally superior to that of polycrystalline bulk samples. However, there are problems that make the growth of good-quality, reproducible thin films difficult. The composition of high-T_c materials is complex. All high-T_c compounds consist of at least four elements that must be deposited within close tolerance of the correct ratio in order to obtain optimised films. The role of oxygen is critical in determining the superconductivity. However, The control of most of the deposition techniques is difficult. Furthermore, the structure of high-T_c superconducting material is highly anisotropic. As a result, the crystallographic alignment in the film is critical, and that makes the growth unpredictable.

One of the most important factors to obtain good quality films is the substrate. Several different materials such as $SrTiO_3$, $LaAlO_3$, MgO, and yttria-stablised ZrO_2 (YSZ), etc. were reported as the substrates of high quality $YBa_2Cu_3O_{7-\delta}$ thin films[11,12]. In this chapter, the structure of $YBa_2Cu_3O_{7-\delta}$ thin films on $SrTiO_3$ and $LaAlO_3$ substrates from various growers will be examined in this chapter.

$SrTiO_3$ was one of the first materials which was successfully used as a substrate for $YBa_2Cu_3O_{7-\delta}$ thin films. It has a cubic perovskite structure as shown in Figure 5.1. Its

lattice constant is a=3.905Å which gives a lattice mismatch $\frac{\Delta a}{a} = +2.0\%$, $\frac{\Delta b}{b} = +0.7\%$ and $\frac{\Delta c}{c} = +0.1\%$ [12,13]. Because of the small lattice mismatch, $SrTiO_3$ is able to support high quality $YBa_2Cu_3O_{7-\delta}$ thin films with $T_c \approx 90K$ and $J_c \sim 10^6$ A/cm^2 at 77K. However, the prohibitively large dielectric constant of this material, (ε=277 at room temperature[12]) makes microwave applications impossible. In addition, although single crystal $SrTiO_3$ is ready available, large sized crystals are unavailable which severely limits research and applications. For these reasons, other alternatives must be found. Figure 5.3 shows the diffraction pattern of a $YBa_2Cu_3O_{7-\delta}$–$SrTiO_3$ thin film. The diffraction patterns from both $YBa_2Cu_3O_{7-\delta}$ and $SrTiO_3$ are convoluted together. In this chapter, the Miller indexes of the $SrTiO_3$ substrates are used as a reference of reciprocal space because of its well-defined lattice.

Like $SrTiO_3$, $LaAlO_3$ also offers only a small lattice mismatch with $YBa_2Cu_3O_{7-\delta}$. At room temperature, the primitive unit cell is rhombohedral[13,14]. It is possible to relate the rhombohedral primitive unit cell to a monoclinic unit cell containing eight molecules. Because $\beta \approx 90°$, the monoclinic unit cell is very close to cubic and the pseudocubic primitive unit cell has been used to index the Bragg reflection for consistency with $SrTiO_3$. The relationship between different unit cell systems and their lattice parameters is shown in Figure 5.4 and Table 5.4. The dielectric constant of $LaAlO_3$ is 24 which make $LaAlO_3$ more suitable as a substrate for microwave applications. However, a second-order rhombohedral-cubic phase transition occurs at 520°C which leads to substrate twinning[15,16]. Because the transition temperature is within the film-processing regime, it is impossible to avoid the phase transition and the substrates are always twinned. The dielectric properties of the twinning substrates vary from point to point in the manner that can not be controlled or predicted. Therefore, the fabrication of complex microwave devices is not yet possible. Even so, twinning has not prevented the growth of high-quality films with high T_c (≈90K) and J_c (≈ 5×10^6 A/cm^2 at 77K).

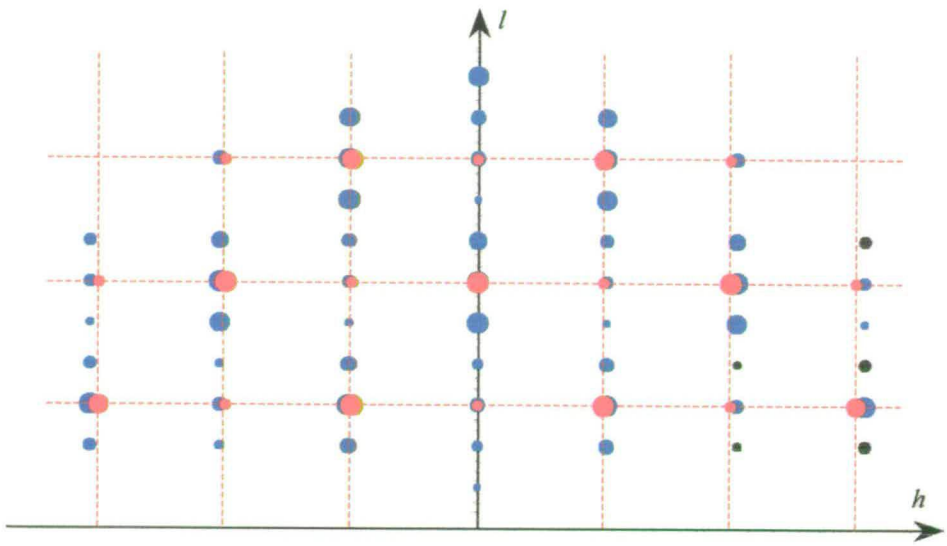

Figure 5.3 The diffraction pattern of a $YBa_2Cu_3O_{7-\delta}$–$SrTiO_3$ sample in reciprocal space. The Bragg reflections from both $YBa_2Cu_3O_{7-\delta}$ (blue dots) and $SrTiO_3$ (red dots) are shown. The reciprocal space is indexed by the $SrTiO_3$ substrate system.

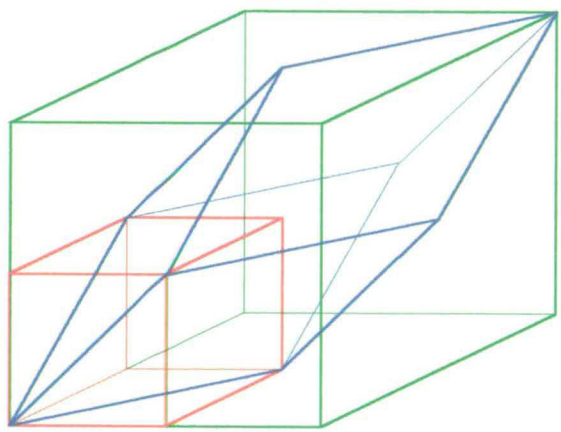

Figure 5.4 Three different definitions of the $LaAlO_3$ unit cell. The detail of cell parameters are presented in Table 5.4.

Table 5.4 Various definition of $LaAlO_3$ unit cell and their cell parameters

Unit cell type	Lattice parameters	# of mole. in a unit cell	Draw colour in Figure 5.4
primitive rhombohedral	a=5.357Å α=60°6′	1	blue
monoclinic	a=7.580Å β=90°5′	8	green
pseudocubic	a= 3.790Å	1	red

5.3 Experiments

Various $YBa_2Cu_3O_{7-\delta}$ thin film superconductors grown on $LaAlO_3$ and $SrTiO_3$ substrates were studied by high-resolution x-ray scattering and the results are presented in this section. The samples were grown by various growers using either pulsed laser deposition or sputtering deposition. The x-ray scattering experiments were performed at the University of Edinburgh using the CPEX diffractometer system, details of which were given in Chapter 3.

5.3.1 $YBa_2Cu_3O_{7-\delta}$–$LaAlO_3$ samples — Institute of Physics, Chinese Academy of Science, Beijing

5.3.1.1 Sample descriptions

$YBa_2Cu_3O_{7-\delta}$ thin film superconductors were grown on $LaAlO_3$ (LAO) by pulsed laser ablation in the Institute of Physics, Chinese Academy of Science, Beijing, China. An XeCl excimer laser with a wavelength 308 nm was employed for sample growth. The pulse width and the energy density of the laser were set to be 40ns and 3–5 J/cm^2. Before the deposition, 600 mTorr oxygen was passed through the deposition chamber and the flux remained constant during the whole process. The temperature of the substrate surface was maintained at 770°C through the deposition. The substrates used were commercial $LaAlO_3$ single crystal wafers which had been

mechanically polished already and had been chemically cleaned prior to the film deposition. Two samples were produced with different thicknesses which were estimated to be 3000Å (sample L3000) and 1000Å (sample L1000). Both samples have a sharp superconducting transition temperature $T_c \approx 90K$ and a critical current density, J_c, in the range of $4.0–6.5\times10^6$ A/cm^2. Details of the sample growth can be found elsewhere[17].

5.3.1.2 Results and discussions

A reciprocal space map around the $(002)_s$ Bragg reflection from the L3000 sample is shown in Figure 5.5 using a logarithmic intensity contour plot. Two peaks are clearly observed in this map: the intense $(002)_s$ substrate reflection and a weaker peak at (0,0,1.944) which is the $(006)_f$ reflection from the $YBa_2Cu_3O_{7-\delta}$ film. This indicates that the YBCO film is well crystallised with a *c* lattice axis approximately parallel to the *c* lattice axis of the LAO substrate. The tilt angle between the YBCO film lattice and the LAO substrate axis is about 0.045°. To estimate the quality of the film, the longitudinal (θ-2θ) and transverse (rocking curve) scans of the $(005)_f$ Bragg reflection were measured and are shown in Figure 5.6. Figure 5.6(a) presents the θ-2θ scan profile. The maximum position gives the *c* lattice parameter to be 11.686±0.002Å and the FWHM of the peak gives the vertical grain size of the YBCO to be 1031±12Å (obtained using the Sherrer formula). The FWHM of the rocking curve of the $(005)_f$ (Figure 5.6(b)) gives a mosaic spread width of 0.378±0.005° which is the average tilting angle of the grain boundaries. These results suggest that the film is highly oriented with excellent quality. In Figure 5.5, it is found that the $(002)_s$ reflection of the LAO substrate is split into two peaks. The splitting comes from the twinning structure associated with the cubic-rhombohedral phase transition at 520°C[15,16].

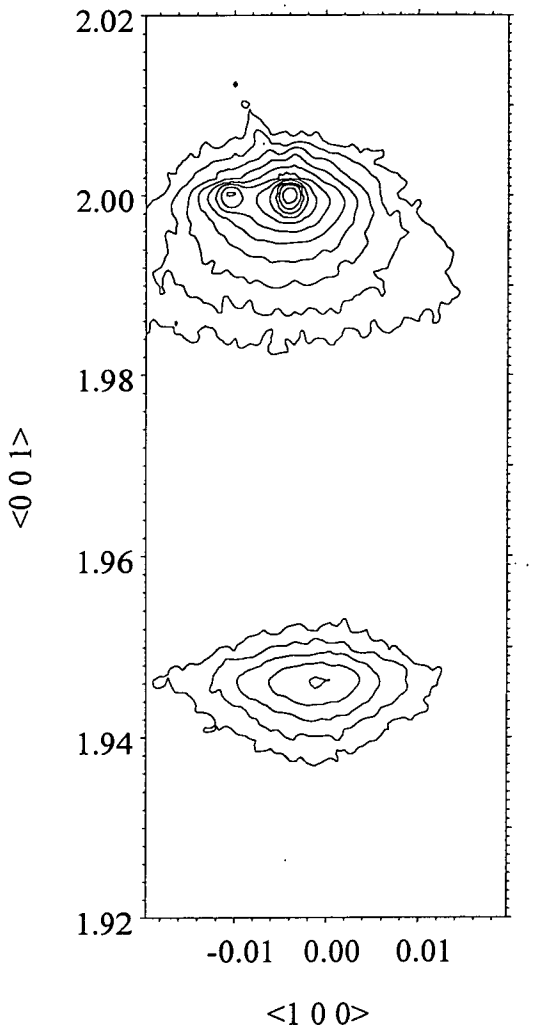

Figure 5.5 Reciprocal space map around the $(002)_s$ Bragg reflection of the L3000 sample.

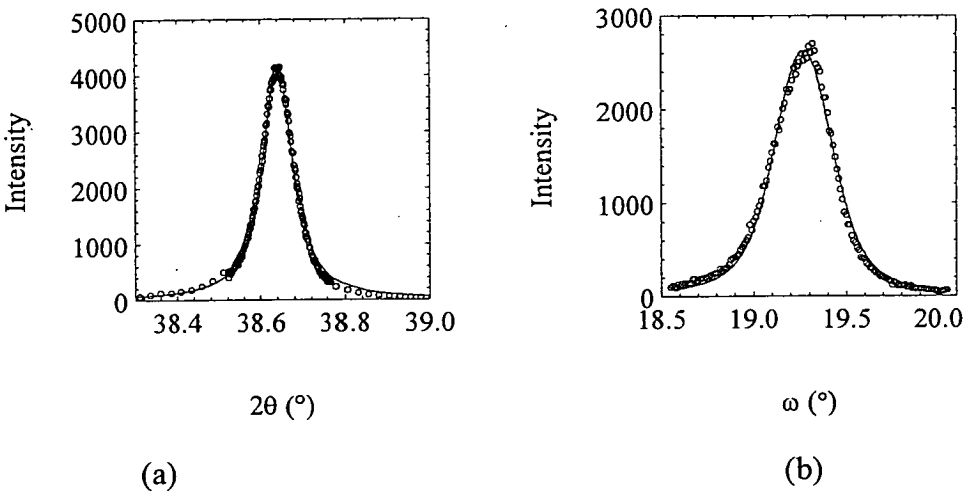

Figure 5.6 (a) Longitudinal scan and (b) rocking curve of the $(005)_f$ Bragg reflection of the L3000 sample

Figure 5.7 shows the θ-2θ scan profile of the $(002)_s$ and the $(006)_f$ reflections of the sample L3000. As previously reported in similar samples by Li et al.[18] and Cox et al.[19] , an extra peak around the $(200)_f$ Bragg reflection from *a/b* oriented grains is found in the θ-2θ scan profile between $(006)_f$ and $(002)_s$. This indicates a mixture of *c* oriented film with *a/b* oriented grains. In sample L3000, there is no evidence of this peak on the θ-2θ scan.

Part of the sample was sent for SEM measurement to reveal the surface morphology and a SEM photograph is shown in Figure 5.8. To reveal the surface morphology of the $YBa_2Cu_3O_{7-\delta}$–$LaAlO_3$ samples, scanning electron microscopy (SEM) was also employed. The SEM experiments utilised a Cambridge S250 SEM operating at 5–10 KV accelerating voltage at the Department of Electrical Engineering, University of Edinburgh. Surprisingly, some of rectangular *a/b* grains were observed on the surface as reported by Carim et al.[20]. The *a/b* oriented grains cover about 3% of the surface. The existence of the *a/b* oriented grains should be observed by x-ray scattering if 3% of the total volume were occupied by them. The inconsistency between the results of x-ray scattering and SEM indicates that the *a/b* oriented grains are concentrated close to the sample surface and only a very few grains can be found inside the film. This will be discussed further later.

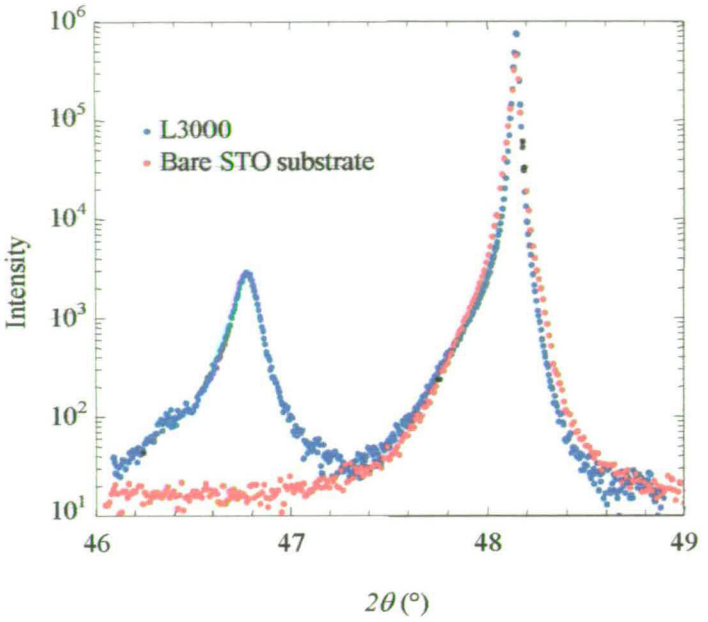

Figure 5.7 The θ-2θ scan profile of the $(002)_s$ and the $(006)_f$ reflections of sample L3000 and a bare LAO substrate prior film growth.

The other noticeable feature in Figure 5.7 is the asymmetry of the $(002)_s$ reflection. To seek an explanation for the asymmetry, the same θ-2θ scan was measured on a bare LAO substrate prior to film growth. The results show great consistency with YBCO-LAO sample which indicates that the asymmetry is not related to the film growth. One of the possible reasons for the asymmetry is the mechanical polishing prior to film growth. Chemical etching of any damaged surface is therefore recommended.

Figure 5.9 shows the reciprocal space map around the $(303)_s$ asymmetric Bragg reflection. The low-resolution mode (graphite monochromator and analyser) was used in this measurement to obtain reasonable intensity. Three peaks are observed in this plot which are recognised to be the $(303)_s$ of the LAO substrate and the $(309)_f$ and $(039)_f$ of twined YBCO thin film. The detailed linear scan in reciprocal space which through of the peak maxima of both the $(309)_f$ and $(039)_f$ reflections is shown in Figure 5.10. From the measurement of the peak positions, the in-plane lattice parameters can be calculated as $a=3.83\pm0.01$Å and $b=3.90\pm0.01$Å.

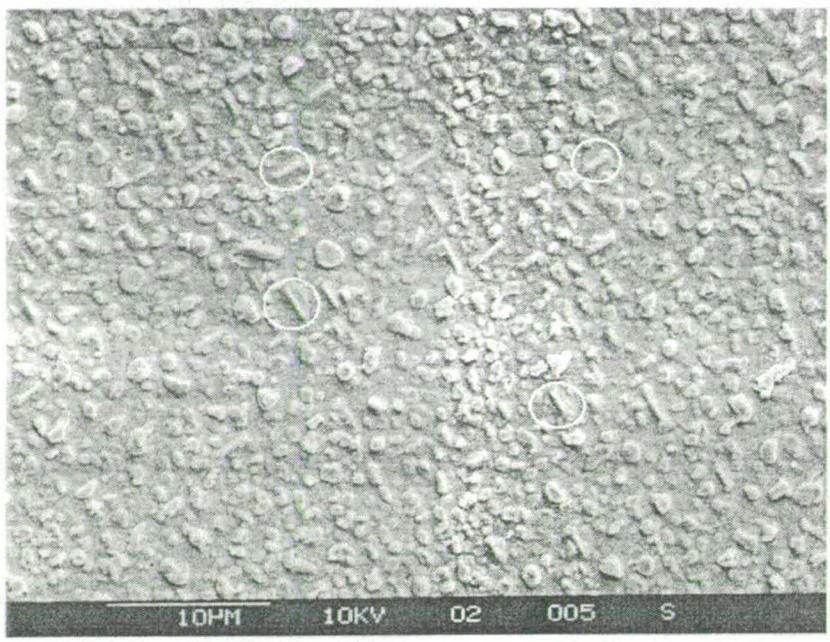

Figure 5.8 The SEM surface micrograph of the L3000 sample. Some of the *a/b* grains observed on the surface are circled.

Figure 5.11 shows the reciprocal space map of the L1000 sample around the $(002)_s$ Bragg reflection. The plot is found similar to the one of the L3000 shown in Figure 5.5. However, there are two significant differences between them. First, the $(006)_f$ YBCO thin film reflection is much wider and weaker. The lattice parameter of the YBCO thin film is calculated to be 11.694±0.002Å which is slightly larger than the one of the sample L3000. The quality of the film as determined by the FWHM of the $(005)_f$ reflection has a grain size of 835±12Å and a mosaic spread width of 0.760±0.005°. Secondly, there is no tilting angle between the YBCO film and the LAO substrate. These results suggest that, in comparison to the L3000 sample, the L1000 thin film is epitaxial to the LAO substrate but with more dislocation and defects.

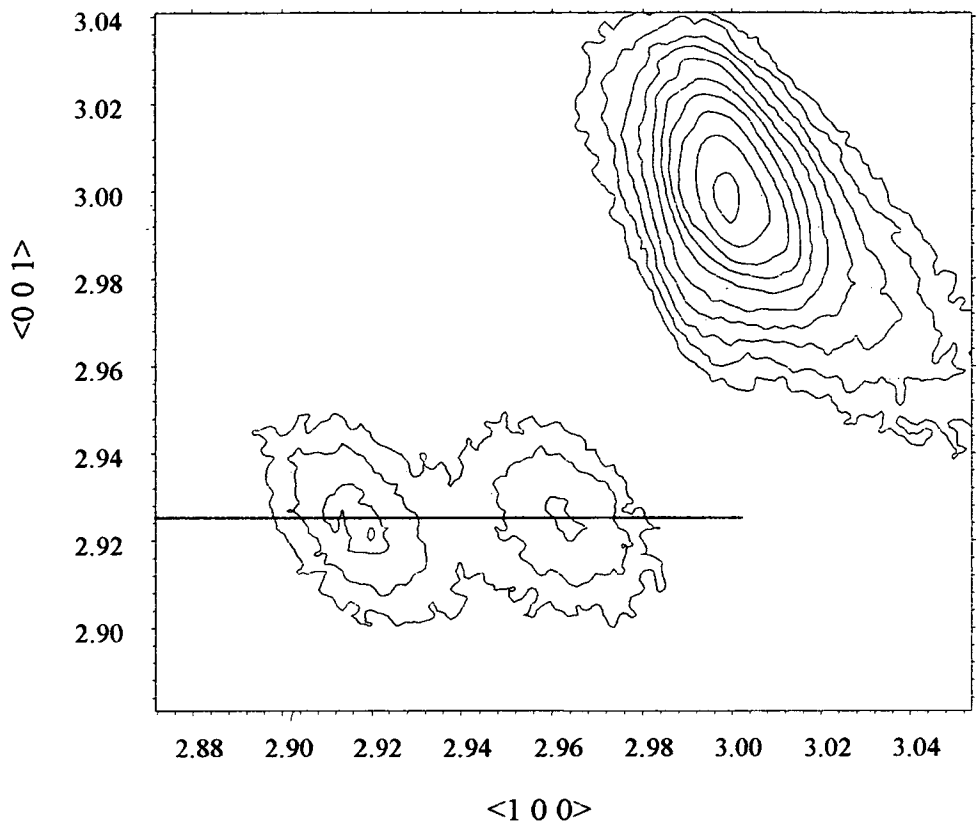

Figure 5.9 Reciprocal space map around the $(303)_s$ Bragg reflection of the L3000 sample. The blue line shows the scan trance through the $(309)_f$ and $(039)_f$ and the profile is shown in Figure 5.10.

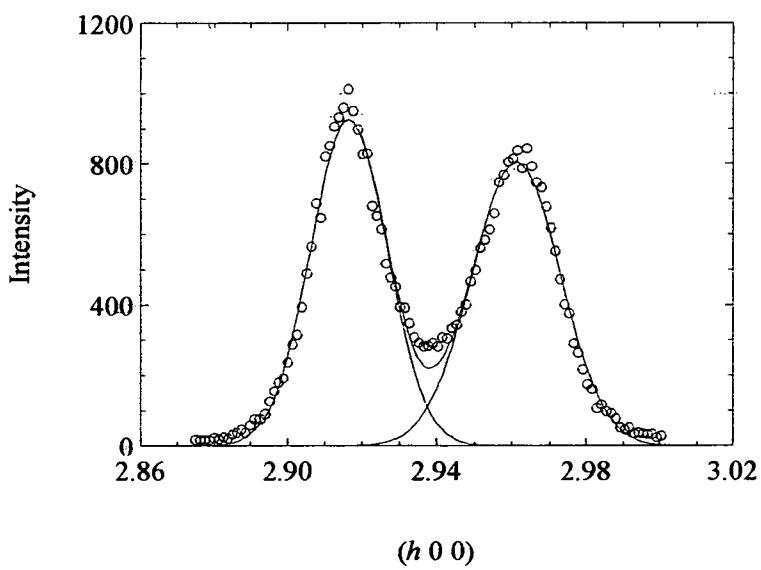

Figure 5.10 The transverse scan along the $(309)_f$ and $(039)_f$ reflections of the L3000 sample.

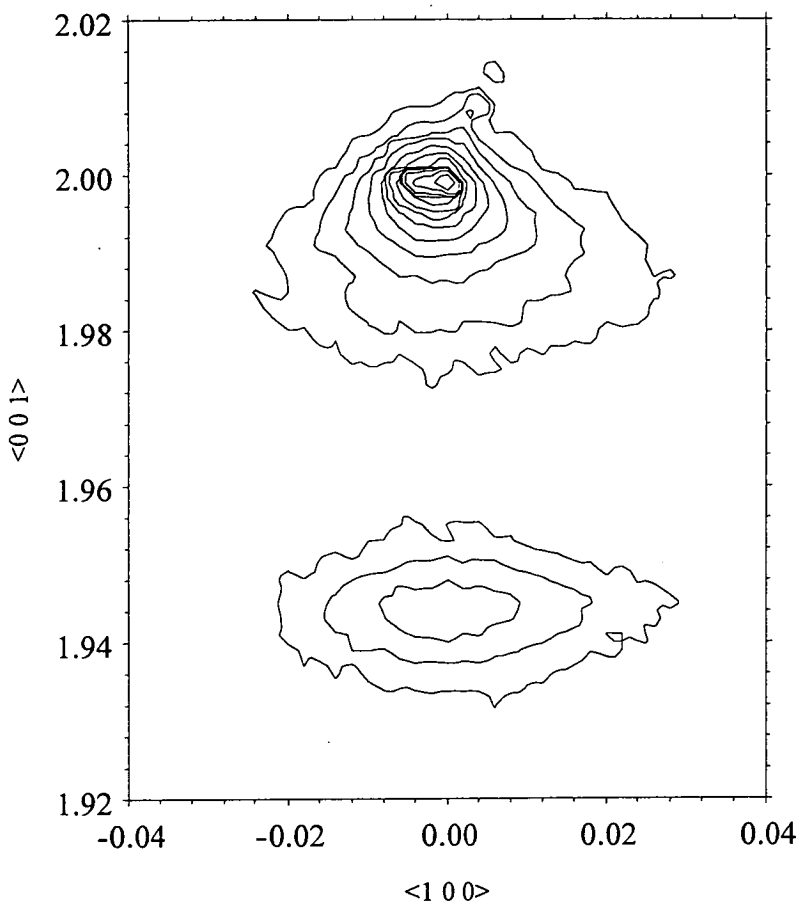

Figure 5.11 Reciprocal space map around the $(002)_S$ Bragg reflection of the L1000 sample.

As in the L3000 sample, there is no evidence for the existence of *a/b* oriented grain in the L1000 sample from the x-ray scattering profile. However, the surface morphology of the L1000 sample is different from the one of L3000 sample. Figure 5.12 shows the SEM of the surface of the L1000 sample. It is clear that rectangular *a/b* grains are not to be found on the surface. As reported by Nieh et al.[21] and Bhatt et al.[22], the density of *a/b* grains is a function of the film thickness, or depth. At the initial stage of film growth, all the film is *c* oriented. As the film gets thicker and thicker, *a/b* grains occur and mix with the *c* oriented grains. Our results are certainly agree with this.

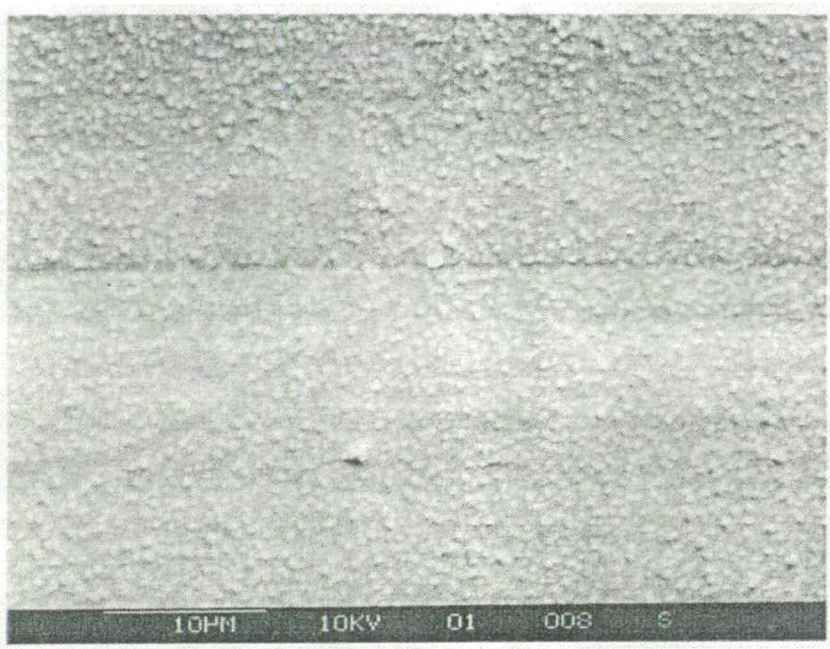

Figure 5.12 The SEM surface micrograph of the L1000 sample.

Figure 5.13 shows a reciprocal space map of the $(303)_s$ reflection of the L1000 sample. This plot is similar to the one of the L3000 sample in Figure 5.9. The $(309)_f$ and $(039)_f$ reflections are much weaker this time, but still clear. The linear transverse scan through these reflections is shown in Figure 5.14. The lattice parameter of YBCO thin film was measured to be $a=3.84\pm0.01$Å and $b=3.89\pm0.01$Å. These results are close to the ones for the L3000 sample. However, the difference between a and b is smaller which suggests that the film lattice is strained by the cubic LAO substrate caused by epitaxial growth. All the experimental results of L3000 and L1000 YBCO-LAO thin films are summarised in Table 5.5.

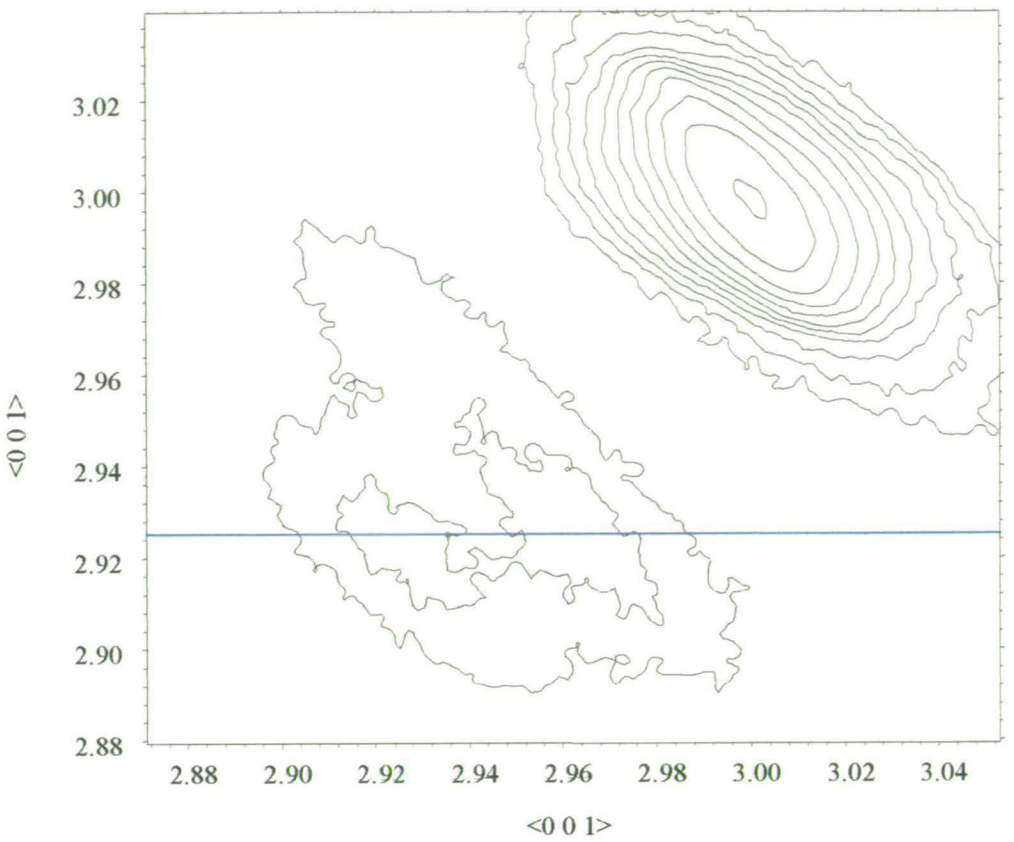

Figure 5.13 Reciprocal space map around the $(303)_s$ Bragg reflection of the L1000 sample. The blue line shows the scan trance shown in Figure 5.14.

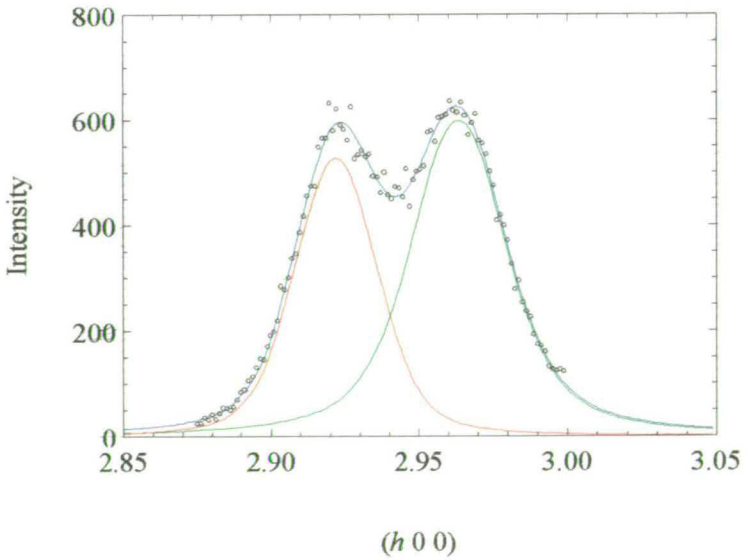

Figure 5.14 The transverse scan through the $(309)_f$ and $(039)_f$ reflections of the L1000 sample.

Table 5.5 The derived parameters of the L3000 and L1000 samples obtained by x-ray scattering

	L3000	L1000
Thickness	3000Å	1000Å
c	11.686±0.002Å	11.694±0.002Å
Grain size	1031±12Å	835±12Å
Mosaic spread width	0.378±0.005°	0.760±0.005°
a	3.83±0.01Å	3.84±0.01Å
b	3.90±0.01Å	3.89±0.01Å

5.3.2 $YBa_2Cu_3O_{7-\delta}$–$LaAlO_3$ and $SrTiO_3$ samples — Cambridge IRC (sputtering)

5.3.2.1 Sample descriptions

A series of $YBa_2Cu_3O_{7-\delta}$ samples grown on $SrTiO_3$ or $LaAlO_3$ substrates with various thicknesses by the DC sputtering deposition technique were grown by the sputtering deposition group, IRC Cambridge. During film growth, the oxygen pressure was 260 Pa and the substrate temperature was 780°C. The details of the deposition equipment can be found in reference [23].

5.3.2.2 Results and discussions

Table 5.6 lists all the samples from Cambridge IRC using DC sputtering deposition techniques. The *c* lattice parameter was calculated from the 2θ value of the $(005)_f$ Bragg reflection. The grain size is derived from the FWHM of the θ-2θ scan of the $(005)_f$ reflection using the Sherrer formula. This grain size directly relates to the reliability of the *c* lattice parameter. The mosaic spread width is determined by the FWHM of the rocking curve through the $(005)_f$ reflection. This measurement directly reflects the average tilting angle between different grains. All these examinations are standard procedures in the determination of films quality.

Table 5.6 List of thickness of the $YBa_2Cu_3O_{7-\delta}$–$SrTiO_3$ and $LaAlO_3$ samples grown by DC sputtering deposition

Sample #	Substrate	Thickness(Å)	c (Å)	Grain size (Å)	Mosaic width (°)
6720-3	LAO	1000	11.680	589.8	0.489
6734-1	LAO	2000	11.682	1056.3	0.149
7805-2	STO	500	11.697	369.6	0.352
7806-2	STO	1000	11.671	1081.1	0.236
7808-2	STO	1500	11.688	979.9	0.249
7799-2	STO	2000	11.699	1145.0	0.134

From the experimental results, no obvious evidence is obtained which suggests that the lattice parameter and the film thickness are dependent upon each other. In fact, the variation of the lattice parameter is less than ±0.15% regardless of the substrate material. This suggests that the growth is controlled well. According to Jorgensen's report[8], all samples we examined have $\delta < 0.2$ and T_c close to 90K. Figure 5.15 shows the temperature dependence of the resistively of YBCO-STO samples.

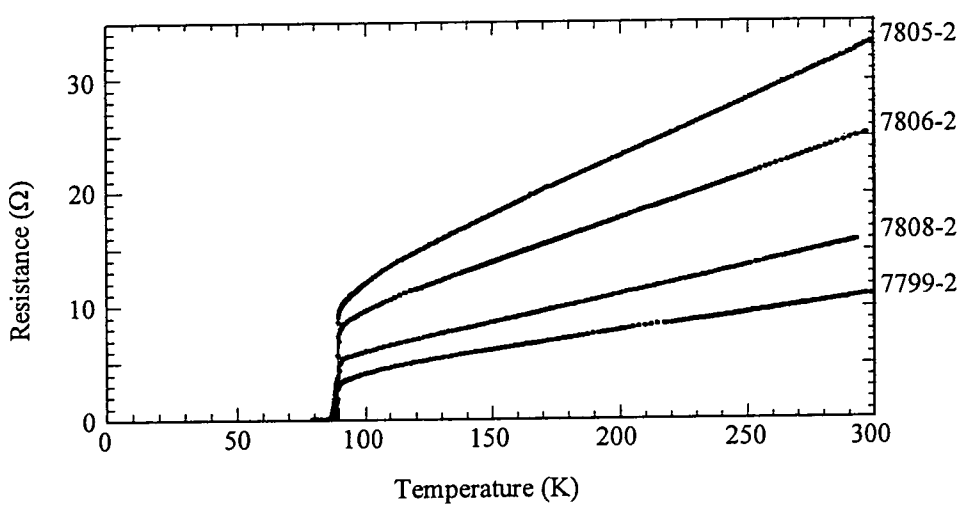

Figure 5.15 The temperature dependence of the resistivity of YBCO-STO samples (provide by Dr R. E. Somekh of Cambridge IRC)

Table 5.6 also gives the quality of YBCO films quantitatively by measuring the grain size and the mosaic spread width. The results show that the grain size and the mosaic width are dependent: the larger the grain size is, the smaller the mosaic width and,

therefore, the better quality the film is. For thin samples (6720-3 and 7805-2), the film quality is very poor. As the film thickness increases, the grain size increases as well. However, after the thickness has reached 1000Å, the grain size seems saturated for YBCO-STO films. The results lead to the following conclusion. The YBCO film grows epitaxially with a large strain and a lot of defects at an early stage. Therefore, the quality of the film with a small thickness is poor. However, after a certain critical thickness, the film is relaxed and behaves like a single crystal. Beyond this critical thickness, the film is relaxed from the substrate and the quality is independent on its thickness. In the YBCO-STO system, the critical thickness is between 500Å and 1000Å. For YBCO-LAO case, the critical thickness is between 1000Å and 2000Å.

5.4 Conclusions

For the examination of the microstructure, x-ray scattering is an excellent and quick non-destructive technique. In this chapter, I have demonstrated the ability of high-resolution x-ray scattering studies in the quality determination of YBCO high-T_c superconducting thin films. YBCO thin films grown on STO and LAO substrates by either laser ablation or DC sputtering were examined and their qualities were measured quantitatively. The results suggest that the YBCO films are grown epitaxially at an early stage. The strain between the film lattice and substrate lattice induces defects. Therefore, the grain size is small and mosaic spread is large, which directly reflects the poor quality of thinner films. As the thickness increases, the films are relaxed from the substrates and they behave like highly oriented polycrystalline films. The critical thickness of the relaxation depends on the lattice mismatch and varies from one substrate to another. The measurement of the YBCO lattice parameter shows considerable uniformity, which suggests that the growth processes are well controlled. Therefore, the quality of the films seems to be limited by the intrinsic properties of the materials.

During the experiments, the structure of the specimen is determined by measuring just a few Bragg reflections. Although this demonstrates the efficiency of x-ray scattering, many features are ignored because of the incomplete measurement. In the

next chapter, one of the best YBCO-STO samples will be fully studied by x-ray scattering and new and important features are revealed in the sample.

---

[1] C.P.Poole, H.A.Farach, and R.J.Creswick, *Superconductivity* (Academic Press, 1995)

[2] J.File, and R.G.Mills, Phys. Rev. Lett. **10**, 93 (1963)

[3] W.Meissner, and R.Ochsenfeld, Naturwissenschaft **21**, 787 (1933)

[4] F.London, and H.London, Proc. Roy. Soc. (London) A **141**,71 (1935)

[5] J.Bardeen, L.N.Cooper, and J.R.Schrieffer, Phys. Rev. **108**, 1175 (1957)

[6] J.G.Bednorz, and K.A.Muller, Z. Phys. B **64**, 189 (1986)

[7] C.W.Chu, J.Bechtold, L.Gao, P.H.Hor, Z.J.Huang, R.L.Meng, Y.Y.Sun, Y.Q.Wang, and Y.Y.Xue, Phys. Rev. Lett. **60**, 941 (1988)

[8] J.D.Jorgensen, B.W.Veal, A.P.Paulikas, L.J.Nowicki, G.W.Crabtree, H.Claus, and W.K.Kwok, Phys. Rev. B **41**, 1863 (1990)

[9] K.Yvon, and M.Francois, Z. Phys. B **76**, 413 (1989)

[10]

[11] E.K.Hollmann, O.G.Vendik, A.G.Zaitsev, and B.T.Melekh, Supercond. Sci. Technol. **7**, 609 (1994)

[12] J.M.Phillips, J. Appl. Phys. **79**, 1829 (1996)

[13] R.W.G.Wyckoff, *Crystal Structure*, Vol.2 (Interscience Publishers, John Wiley & Sons, 1964)

[14] S.Geller, and V.B.Bala, Acta Cryst. **9**, 1019 (1956)

[15] H.Fay, and C.D.Brandle, J. Phys. Chem. Solids, Suppl. **1**, 51 (1967)

[16] H.M.O'Bryan, P.K.Gallagher, G.W.Berkstresser, and C.D.Brandle, J. Mater. Res. **5**, 183 (1990)

[17] Q.X.Su, S.F.Xu, D.F.Cui, H.B.Lu, Y.J.Tian, Y.Z.Zhang, Z.H.Chen, L.Li, and G.Z.Yang, Morden Phys. Lett. B **6**, 477 (1992)

[18] C.R.Li, Z.H.Mai, P.D.Hatton, and C.H.Du, Acta Phys. Sinica **42**, 1479 (1993)

[19] U.J.Cox, J.Crain, P.D.Hatton, G.S.Green, and D.Y.Dai, J. Appl. Phys. **75**, 7966 (1994)

[20] A.H.Carim, S.N.Basu, and R.E.Muenchausen, Appl. Phys. Lett. **58**, 871 (1991)

[21] C.W.Nieh, L.Anthony, J.Y.Josefowicz, and F.G.Kajenbrink, Appl. Phys. Lett. **56**, 2138 (1990)

[22] D.Bhatt, S.N.Basu, A.C.Westerheim, and A.C.Anderson, Physica C **222**, 283 (1994)

[23] R.E.Somekh, and Z.H.Barber, J. Phys. E: Sci. Instrum. **21**, 1029 (1988)

Chapter 6

Observation of an Ultra-High-Quality $YBa_2Cu_3O_{7-\delta}$ Thin Film on $SrTiO_3$ Substrate

6.1 Introduction

The ability to understand and control the morphology of high-T_c oxide thin film superconductors is important both for technological applications and for fundamental studies. To explore the structure of thin films, especially the buried interfaces, grazing incidence x-ray reflectivity (GIXR) has been employed most frequently, and it has achieved great success with semiconducting epitaxial thin films[1,2,3,4]. Recently, GIXR has been applied to the study of surface and interface structures of high-T_c thin film superconductors and reasonable results have been obtained[5,6,7,8,9]. For example, Asami et al.[7] and Ichinose et al.[9] have both applied GIXR to ultra-thin $YBa_2Cu_3O_x$ (YBCO) thin films. They measured the surface and interface roughness and proposed film growth models for different substrates such as $SrTiO_3$ (STO) and MgO. Gau et al.[8] have applied GIXR and grazing incidence x-ray diffraction (GIXD) to study the layer structure of YBCO thin films. Their results show that a mosaic layer, a tetragonal layer, an orthorhombic layer and a surface contamination layer are sequentially stacked above the substrate. All of these reports demonstrate that GIXR is a useful technique for studying thin film structure and its growth mechanism. However, GIXR is sensitive only to the electron density depth profile of the film but not to the crystallographic structure. In this case, the low-angle specular reflectivity

profiles of GIXR from a strained crystal and amorphous layer will be the same if their electron density distributions are identical. Unless other complementary techniques are performed, GIXR gives only the electron density structure along the surface normal direction.

An other x-ray scattering technique available for this type of study is on-axis crystal-truncation-rod (CTR) analysis, sometimes referred as high-angle specular reflectivity[10,11]. Unlike GIXR, the on-axis x-ray scattering intensity profiles near Bragg reflections are extremely sensitive to the lattice distortion, crystal thickness, the surface, and the interface roughness morphology. Terashma, Kamigaki and their colleagues have published a series of reports which have routinely used the Laue finite size fringes of the CTR profiles to precisely determine the thickness of various YBCO samples grown by activated reactive evaporation deposition[12,13,14]. Along with reflection high-energy electron diffraction (RHEED) analyses, the critical thickness of the strain relaxation was measured to within the resolution of single unit cell. Nakamura et al. took a similar approach to the study of the interface roughness of $GdBa_2Cu_3O_{7-\delta}$ thin films on STO substrates grown by magnetron sputtering[15]. They used the frequency of the Laue fringes of the finite size crystal to calculate the thickness. The uncertainty of the thickness was interpreted as the roughness of the films. Their results demonstrated the ability of applying the CTR analyses to study the film thickness and the surface and interface roughness. Amongst all of these reports, however, the CTR profiles have not been properly analysed. Because of over-simplification of the CTR calculation, only the thickness of the film could be resolved by simply measuring the frequency of the Laue fringes. However, further information such as the strain field of the lattice can be accessed by properly fitting the profiles. Nevertheless, due to the relatively poor crystal quality, strong x-ray absorption and the existence of interfacial disorder, it is more problematic to study thicker superconducting films using either GIXR or CTR techniques. So far, no study has been reported on YBCO thin films with thickness over 500Å to date. This limit is substantially below that of commercial high-T_c superconducting thin films used in microwave and other applications.

In this chapter, a YBCO thin film with a thickness of about 1800Å grown on a STO substrate was studied by high-resolution x-ray scattering. GIXR was first used to study the depth profile and determine the thickness of the film. An amorphous surface oxidation layer was found on top of the film. Traditional x-ray diffraction techniques including θ-2θ scans, rocking curves and reciprocal space mapping, were then applied to examine the crystallographic structure of the sample. The low-index Bragg reflections were found to have very different features from the high index ones. Three different components, which come from the epitaxial YBCO buffer layer, ultra-high-quality YBCO film and mosaic YBCO inclusions were observed. The details of each component were studied in detail and are described below.

6.2 Experiment

6.2.1 Experimental details

The YBCO thin film was grown on (001) $SrTiO_3$ (STO) substrates by off-axis pulsed laser ablation at the Interdisciplinary Research Centre in Superconductivity, University of Cambridge. A KrF laser with a wavelength 248nm was employed for the film growth, and the energy density was about 1.5 J/cm^2. During the deposition, the oxygen pressure was maintained at 0.3 mbar and the temperature of the $SrTiO_3$ substrate was 780°C. After growth, the samples were cooled to room temperature under 1 atm oxygen flow. The superconducting transition temperature of the sample was measured to be about 88K and the critical current was over 10^6 A/cm^2 at 77K. The film is eptaxially grown on the substrate with c_f[16] parallel to surface normal (c-oriented) or c_s axis. The other two axes (a_f and b_f) are lying on the surface plane and parallel to the substrate axes (a_s and b_s). The lattice parameters of the bulk crystals are shown in Table 6.1. The sample studied has a thickness of about 1800Å.

Table 6.1 The lattice parameters of the bulk YBCO and STO crystals

	Material	Structure	a	b	c
Thin film	$YBa_2Cu_3O_{7-\delta}$	Orthorhombic	3.82 Å	3.89 Å	11.68 Å
Substrate	$SrTiO_3$	Cubic	3.905 Å	3.905 Å	3.905 Å

The x-ray scattering experiments were performed using Station 2.3 at the Daresbury Laboratory, Synchrotron Radiation Source. The equipment configuration was described in Chapter 3. The wavelength was chosen to be 1.200Å to maximise the x-ray intensity. The beam size and the pre-detector silt were both set as 100μm. Under these conditions, the angular resolution is on the order of 0.001°.

6.2.2 On-axis crystal-truncation-rod profiles of single crystal films with inhomogeneous strain field

The scattering amplitude of a thin film system can be calculated as

$$A = A_0 \int_r e^{-i(q\cdot r)+\mu r_z} dr = A_0 \sum_{n=0}^{N-1} e^{-(2\pi i q_z - \mu)z_n} \tag{6.1}$$

Here, we assume that the z direction is parallel to the surface normal. The origin of the z-axis is put at the interface between the film and the substrate with positive z upwards. We also assume that the x and y directions are completely independent from the z direction and the summations along x and y are treated as a constant, and included in the normalisation factor, A_0. So, the calculation is simplified to a one-dimensional problem. N is the number of unit cells within the film along the z direction. q_z is the momentum transfer vector which is defined as

$$q_z = 2\frac{1}{\lambda}\sin\theta = lc^* \tag{6.2}$$

where λ is the x-ray wavelength, and θ is the scattering angle. The momentum transfer vector can also be represented in reciprocal space unit as l times the reciprocal lattice parameter, c^*. Finally, μ is the absorption coefficient which is associated with the linear absorption coefficient, μ_l

$$\mu = \frac{\mu_l}{\sin\theta}$$

For a film with an associated strain field, this can be modelled by assuming a small displacement is added to the position of the unit cell

$$z_n = z_{n,0} + n\Delta_n c_0 = nc_0(1+\Delta_n) \tag{6.3}$$

Where $z_{n,0}$ is the position of the n-th unit cell without a strain field and $n\Delta_n c_0$ is a small additional strain field displacement. The lattice parameter of the n-th unit cell can then be described as

$$c(n) = z_n - z_{n-1} \approx c_0(1+\Delta_n) \tag{6.4}$$

Here, we assume the strain field is small, and varies slowly and smoothly with z. So, the strain field can be changed to a continuous form.

$$\Delta(z) = \Delta_n \tag{6.5}$$

where $z = nc_0$

The scattering amplitude of the strained system becomes

$$A = A_0 \sum_{n=0}^{N-1} e^{-(2\pi i q_z - \mu) z_n} = A_0 \sum_{n=0}^{N-1} e^{-(2\pi i l - \mu) n(1+\Delta_n)} \tag{6.6}$$

The scattered intensity is the square modulus of the scattering amplitude,

$$I(l) = |A(l)|^2 = \left| A_0 \sum_{n=0}^{N-1} e^{-(2\pi i l - \mu) n(1+\Delta_n)} \right|^2 \tag{6.7}$$

In fitting the experiment results, the scattered intensity has been assumed to be of the following form

$$I(l) = I_0 R \left| \sum_{n=0}^{N-1} e^{-(2\pi i l - \mu) n(1+\Delta_n)} \right|^2 \tag{6.8}$$

where I_0 is the normalisation factor and R is the factor due to the roughness[2],

$$R = e^{-\sigma_n^2 \sin^2\left(\frac{q_z c_0}{2}\right)} = e^{-\sigma_n^2 \sin^2(\pi l)} \tag{6.9}$$

in Equation (6.9), σ_n is the variance of the Poisson random variables used to model the random surface crystalline roughness[17]. For the reflection close to the Bragg reflection, σ_n is directly related to the surface roughness, σ

$$\sigma^2 = \frac{c_0^{\,2}\sigma_n^{\,2}}{2} \tag{6.10}$$

By minimising least square of the deviation, χ^2, the function of the strain field of the film can be determined.

$$\chi^2 = \sum \left| \frac{\log(I_{exp}) - \log(I_{cal})}{\log(I_{exp}) + \log(I_{cal})} \right|^2 \tag{6.11}$$

The thickness of the film can also be calculated precisely by

$$H = \sum_{n=0}^{N-1} c_n = \sum_{n=0}^{N-1} c_0(1+\Delta_n) \tag{6.12}$$

6.3 Results and discussion

6.3.1 Grazing Incidence X-ray Reflectivity (GIXR) measurements

Grazing incidence x-ray reflectivity has long been used for analysing the crystal structure near the surface of semiconducting materials[1,2,3] and high-T_c oxide superconducting thin films[12,13,14,15]. Figure 6.1(a) shows the GIXR measurement of the YBCO-STO sample. Keissig fringes are observed at $\theta \approx 0.55°$, which are due to the interference between the surface and the interface scattering. Using the distorted-wave born approximation (DWBA)[3], the best fit of GIXR result gives a structure of the film as depicted in Figure 6.1(b). The film thickness was found to be 1930±10Å. A thin layer of lower density ($\rho = 0.95 \cdot \rho_0$) was also found on the top of the film with a thickness of 78±1Å and a large surface roughness (σ = 27±1Å). This layer is probably an oxidation layer with a high dislocation density. The existence of such an oxidation layer has also been observed previously in some reports[8,18]. The transverse scan at $\theta = 0.62°$ is shown in Figure 6.2. This shows simply the specular ridge and two Yoneda wings. No evidence of any correlation between the surface and the interface was found.

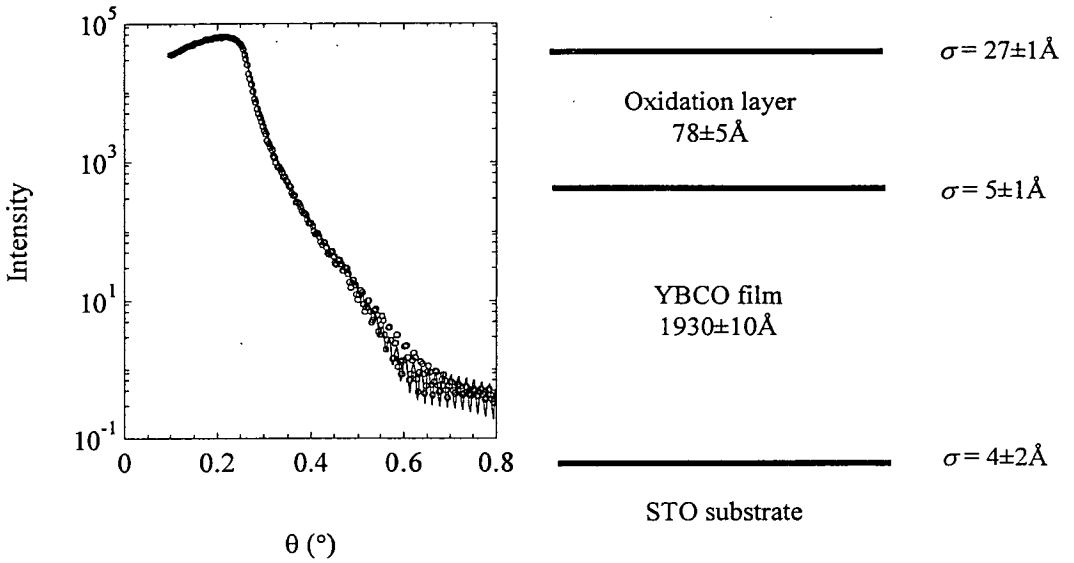

(a) (b)

Figure 6.1 (a) The GIXR result of the YBCO-STO sample (b) structure model used for the best fit.

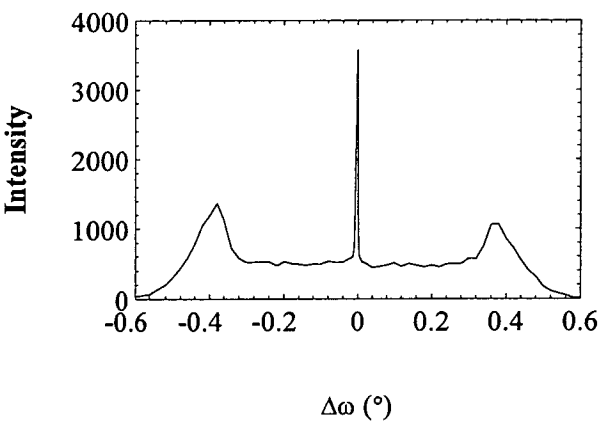

Figure 6.2 The transverse scan at $\theta = 0.62°$.

6.3.2 High-resolution x-ray diffraction measurements

The on-axis Bragg reflections of the YBCO thin film were observed as high as the (0,0,16) reflection, which indicates that the film is highly oriented. Figure 6.3 shows the peak profiles of the (005) Bragg reflection. Because of the strong intensity and reasonable 2θ angle, the FWHM of this peak are generally utilised for quantitatively determining the quality of the films. Figure 6.3(a) shows the reciprocal space map of

the (005) Bragg reflection. Figure 6.3(b) and Figure 6.3(c) are the longitudinal (θ-2θ) scan and the transverse (rocking curve) scan through the centre of the Bragg reflection and their best fits using Lorentzian profiles. From the rocking curve, the mosaic width of the YBCO thin film is 0.115° which shows the excellent quality of the film. This result is much better than the other samples that we have published separately[19].

To characterise the lattice parameter of the YBCO in detail, the positions and the widths of the Bragg reflections were measured, and are shown in Figure 6.4. Figure 6.4(a) shows the dependence of the Bragg angle on the diffraction order, l, from (005) to (0,0,16). The best fit to Bragg's law gives a c lattice parameter of 11.696±0.001Å. The average size of the crystal grains along the surface normal direction is given by fitting the dependence of the FWHM of the θ-2θ scans (Figure 6.4(b)) with Sherrer's formula[20,21]

$$\Delta_{2\theta} = \frac{0.94\lambda}{L\cos\theta} \tag{6.13}$$

The broadening of the θ-2θ scan due to the residual strain is also considered in the fitting

$$\Delta_{2\theta} = 2\frac{\Delta c}{c}\tan\theta \tag{6.14}$$

The fitting result gives a grain size of 106.7±3.8Å and the residual strain, $\frac{\Delta c}{c}$, of 10^{-5}, which shows no residual strain in the YBCO grain. These results are close to the values reported by Argunova et al.[21]

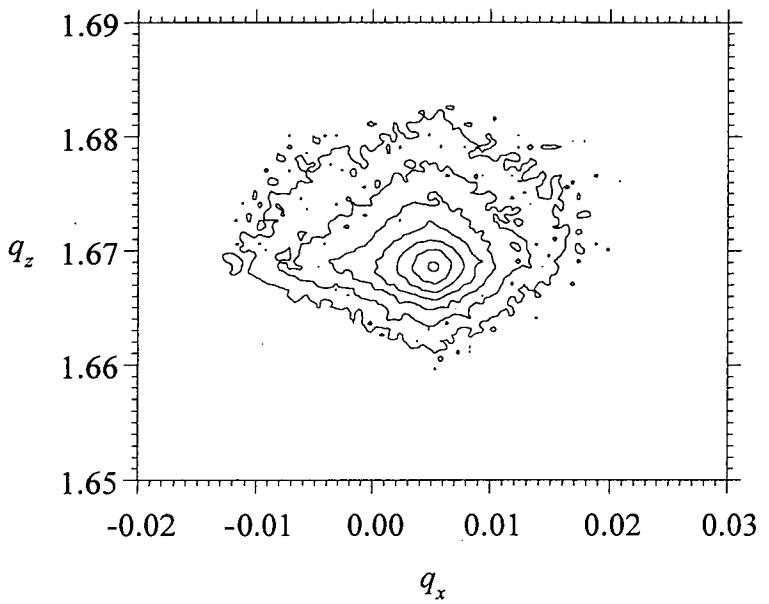

(a)

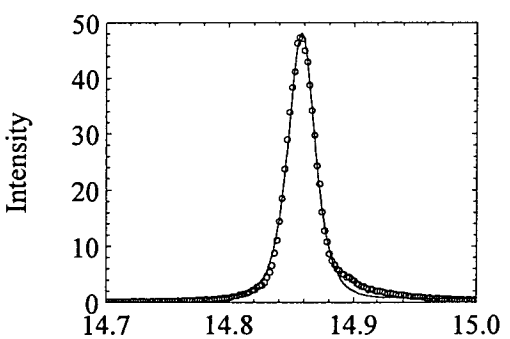

(b)

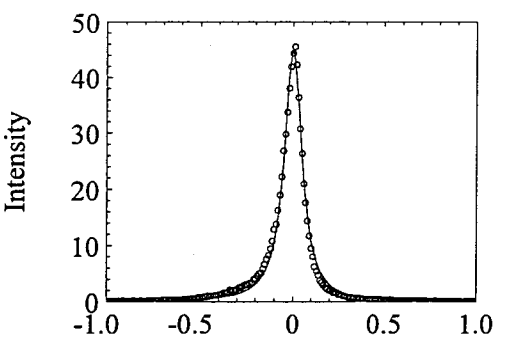

(c)

Figure 6.3 The peak profile of the (005) Bragg reflection of the YBCO thin film. (a) The associated reciprocal-space-map. The contours levels are 0.9, $\frac{1}{2}$, $\frac{1}{4}$, $\frac{1}{8}$, $\frac{1}{16}$, $\frac{1}{32}$, $\frac{1}{64}$ of the peak intensity. (b) the θ-2θ scan and (c) the rocking curve. The Lorentzian profile is employed in both fits.

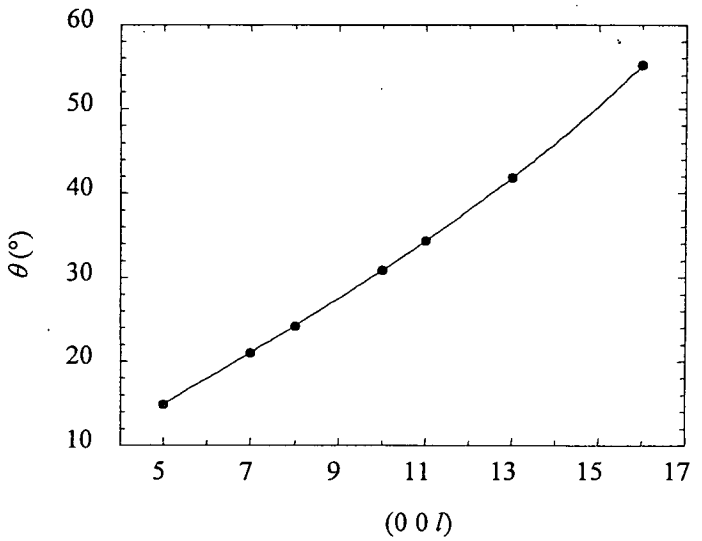

(a)

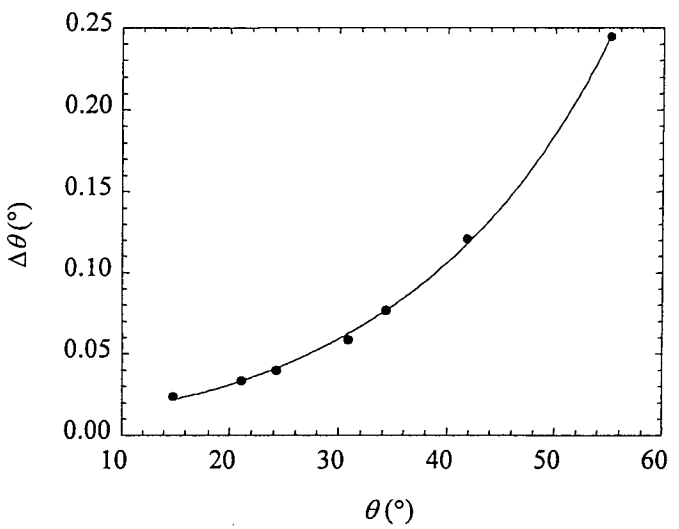

(b)

Figure 6.4 (a) the Bragg angles and (b) the FWHM for the (00*l*) YBCO Bragg reflections ($l = 5 - 16$).

Figure 6.5 presents the FWHM of rocking curve vs. Bragg angle of the (00*l*) reflections. The angular spread is mainly contributed by two factors: the lateral grain size and the mosaicity (the orientation distribution of grains). The peak breadth caused by lateral grain size in reciprocal space is roughly inversely proportional to the grain size and the angular spread can be expressed as

$$\Delta_\omega = \frac{\Delta_{q_x}}{q_z} = \frac{\lambda}{2W \sin\theta} \tag{6.15}$$

where W is the average lateral grain size. The angular spread caused by the mosaicity depends only on the orientation distribution function of the grains. Therefore, the angular width is a constant. As shown in Figure 6.5, the best fit gives the lateral grain size to be 2459±10Å and the mosaic spread angle to be 0.053±0.005°. These results represent that the excellent quality of this sample in comparison to those examined in Chapter 5 and elsewhere[21,22].

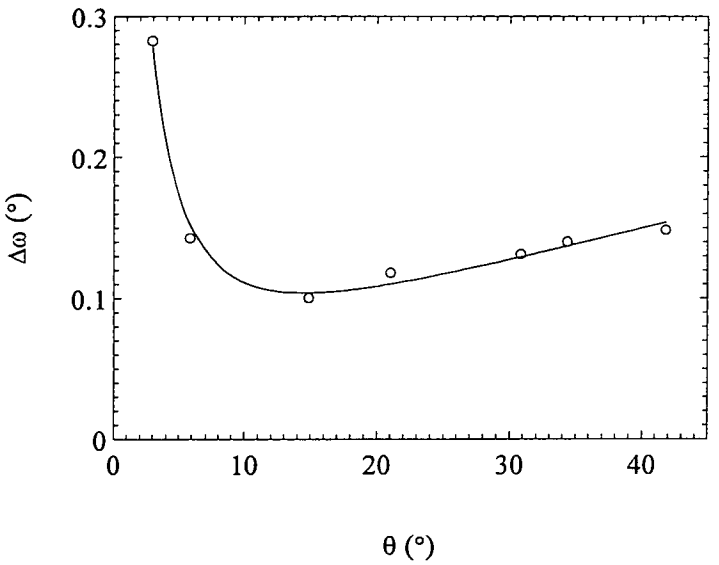

Figure 6.5 Rocking curve width vs. Bragg angle

It must be mentioned, however, that the low index Bragg reflections (l=1,2) showed a completely different profile in both longitudinal and transverse directions which are much more complex and contain more detailed information about the crystal structure. These will be discussed further in later.

Figure 6.6 shows the reciprocal space map of the (002) STO and the (006) YBCO Bragg reflections. In this semi-log contour intensity map, it was found that the sharp (002) STO reflection and broad (006) YBCO are not in the same crystallographic direction. This indicates the lattice planes of YBCO and STO are not parallel. From the shift, the wedge angle was measured to be ~0.2°. The streak associated with the (002) STO reflection is the monochromator streak which demonstrates the superior quality of the STO substrate.

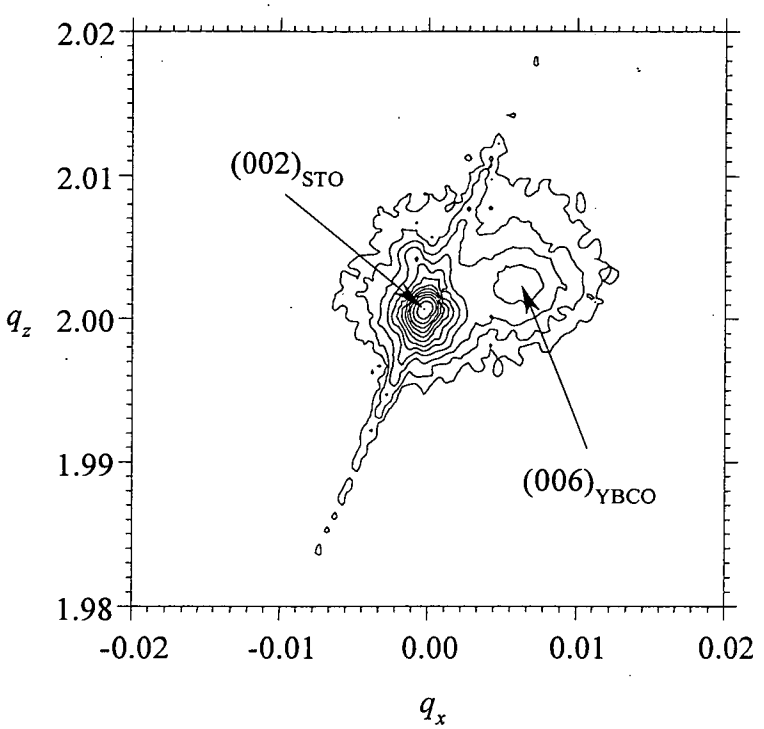

Figure 6.6 The reciprocal space map of the (002) STO and the (006) YBCO Bragg reflections.

6.3.3 Low index Bragg reflections and the observation of the ultra-high-quality single crystal YBCO thin film

The low-index Bragg reflections of the YBCO film, such as (001) and (002), were demonstrated to show rather complicated profiles. Figure 6.7 shows the full range θ-2θ scan from $\theta \approx 0.2°$ to 4° along the surface normal direction. The specular GIXR profile is clear below $\theta = 1°$ with Keissig interference fringes. An additional peak was found at $\theta \approx 2.95°$ with many associated satellites which was recognised to be the YBCO (001) Bragg reflection. A reciprocal space map around the (001) Bragg reflection is shown in Figure 6.8. In addition, as shown in Figure 6.10, a similar reflection with satellites was also observed at $\theta \approx 5.89°$ consistent with the YBCO (002) Bragg reflection. These reflections are associated with a lattice parameter, c of about 11.69Å, which is the lattice parameter of the YBCO crystal derived by the high-order reflections in Section 6.3.2. The satellites of the YBCO Bragg reflections are caused by Laue finite size fringes from the CTR (or high-angle reflectivities) and the frequency of these fringes gives the thickness of the film, around 1800Å. The

same Laue fringes have been reported on YBCO thin films with thickness far less than 500Å but have never been observed on thicker films[14,15].

To reveal the film structure in detail, least square fitting was applied on the (002) reflection. The film thickness was first estimated to be 1800Å by using the frequency of the Laue fringes. Then, the diffraction profile was generated. By tuning the scaling factor and the roughness of the film, reduced the error, χ^2, between the experimental results and the calculation. The best fit obtained is shown in Figure 6.10. χ^2 is defined as

$$\chi^2 = \sum_i \left| \frac{\log(I_{\exp}) - \log(I_{cal})}{\log(I_{\exp}) + \log(I_{cal})} \right|^2 \tag{6.16}$$

According to the kinematical theory, the scattered intensity is proportional to the multiplication of the square modulus of the geometry factor, $|G(q)|^2$, and the square modulus of the structure factor $|F(q)|^2$.

$$I(q) \propto |F(q)|^2 |G(q)|^2 \tag{6.17}$$

In most cases, the scattering intensity is only appreciable near where the Bragg condition is fulfilled. In other words, $G(q)$ has none-zero value only when q is very close to the reciprocal lattice point. Under this condition, because the structure factor was varied slowly in comparison to the geometry factor. It is assumed that the structure factor is approximately constant and is combined into the scaling constant when analysing the intensity profile of a single Bragg reflection. However, because of the complexity of the YBCO unit cell, and the large lattice parameter, the unit-cell structure factor varies severely over the angular range of the CTR profiles. Figure 6.9 shows the variation of structure factor of YBCO crystal. The positions of the red lines are the (001) and the (002) Bragg reflections and the green shadowed areas are the angular range within which the CTR profiles were taken.

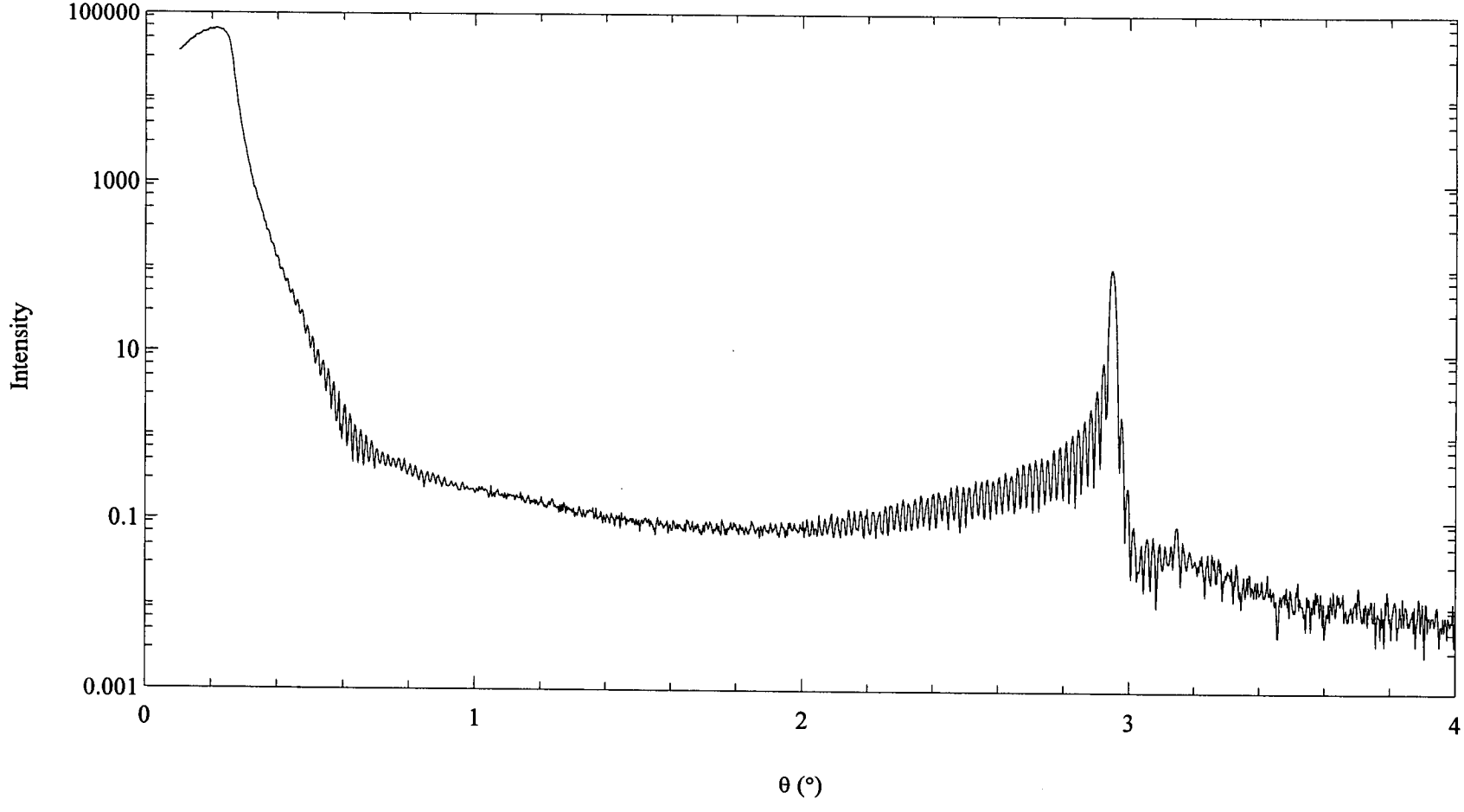

Figure 6.7 The specular reflection profile. An extra reflection was found at $\theta \approx 2.95°$ with lots of related satellites. This peak was found to be the (001) Bragg reflection from the ultra-high-quality YBCO crystal. The existence of the satellites shows the quality of the crystal is perfectly coherent over a large volume.

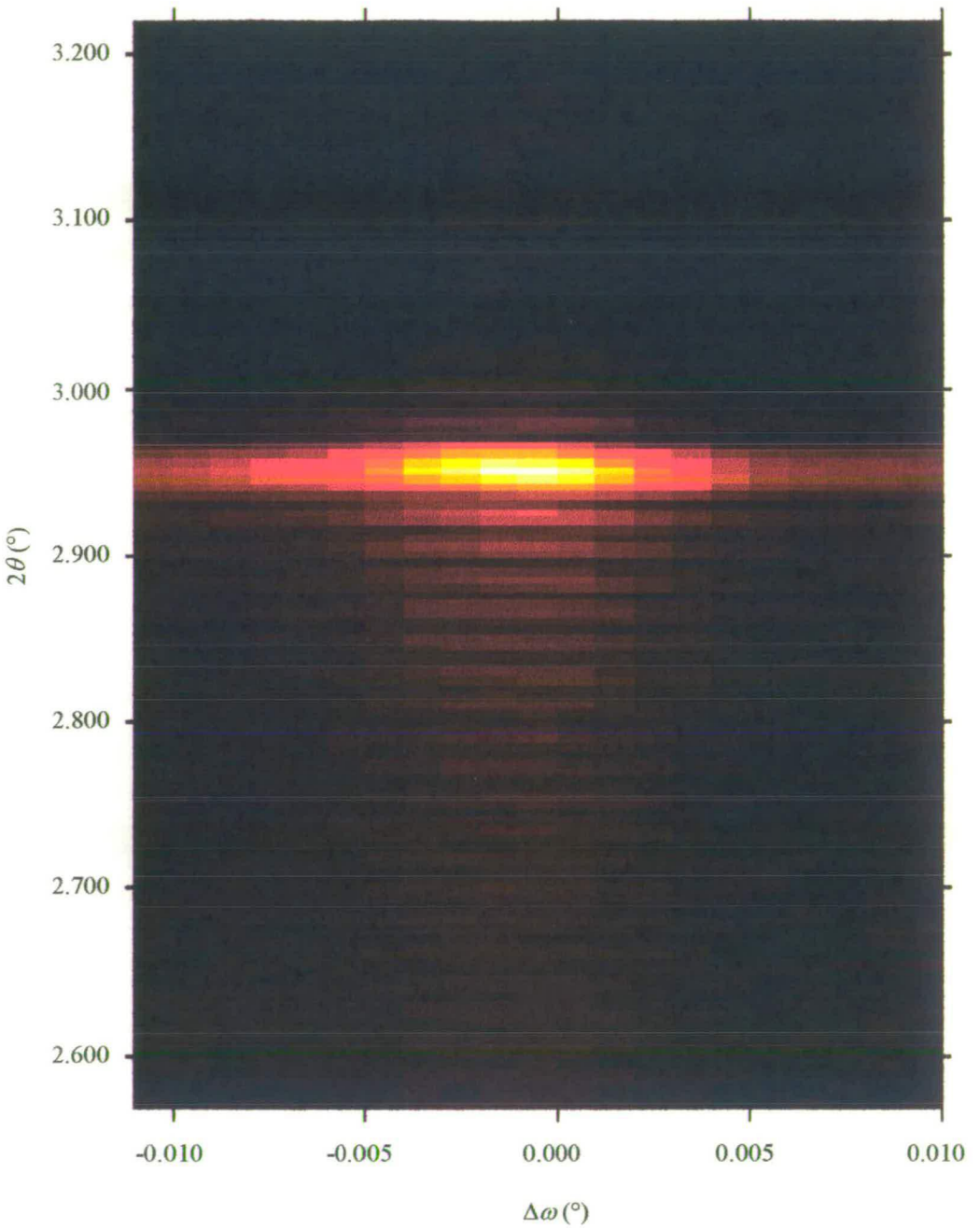

Figure 6.8 The reciprocal-space-map of the (001) Bragg reflection used to demonstrate the Laue fringes are on the specular reflection ridge.

During the fitting, a linear intensity background was assumed, and the resolution of the diffractometer was set to 0.001° [23]. It is noticed that the intensity contrast of the satellites is not asymmetrically distributed around the central Bragg reflection, as clearly observed in the data. To explain the asymmetry, an exponential strain field was considered. Figure 6.11(a) shows the diffraction profile from a film with exponential strain close to the interface as presented in Figure 6.11(b). The strain field can be described by

$$c_n = c_0\left(1 + \Delta \cdot e^{-\alpha(N-n)}\right) \tag{6.18}$$

where c_n is the lattice parameter of the n-th unit cell from the film surface. Δ is the magnitude of the strain and $\alpha = \frac{\ln 2}{n_{1/2}}$ is the relaxation distance of the strain. Similar strain fields have been observed in many semiconductor thin films[24,25,26]. Gusso et al. theoretically calculated the strain in epitaxial YBCO thin films and concluded that the interfacial strain in (001) oriented thin films is the smallest. The incorporation of a small strain field close to the interface causes the intensity contrast of the Laue fringes to be much stronger on the low angle side of the central Bragg reflection, which is observed in the experimental data. Similar results were observed by He et al. in GaInP/GaAs superlattice[25]. To confirm the location of the strain, a simulation profile from a film with a strain field with the same parameters but close to the surface is shown in Figure 6.12. The intensity contrast of the Laue fringes is then stronger on the high angle side. This result suggests the existence of a strain field near the interface, and this strain field could be caused by the lattice mismatch between the YBCO film and the STO substrate. However, the average profile does still not fitting well. The only way to achieve a better fit is to add an extra weak and broad reflection as shown in Figure 6.13. Because the peak is buried beneath the CTR profile, it is very difficult to estimate the parameters describing it, these are the position, width, and intensity which define the lattice parameter and direct space size. The source of this peak is still unclear. However, since the scattering angle is slightly higher than the (002) Bragg reflection, which implies a shorter lattice parameter, it is likely that the extra peak comes from a strained interface layer. The parameters of the best fit in Figure 6.13 are listed in Table 6.2. Similar extra weak reflections were also

observed in other YBCO-STO samples but the parameters describing them varied from sample to sample. This observation indicates that the weak reflection might be caused by a distorted YBCO crystal which is strongly dependent on the small variation due to uncontrollable sample preparation or experimental conditions.

Figure 6.14 shows the θ-2θ scan of the (002) Bragg reflection of the same sample obtained using the in-house CPEX system (Chapter 3). Because of the use of a conventional rotating-anode x-ray source, the interference fringes can only be observed up to fourth order. By using a synchrotron radiation source, as shown in Figure 6.10, the fringes can be observed up to tenth order which makes our studies much more accurate. The synchrotron radiation provides an intense source of highly collimated x-rays allowing for high-resolution measurement of even weak features situated around low index Bragg reflections. Furthermore, as the film thickness increase so the angular separation of the satellites decreases. The high-resolution and high-intensity obtainable using synchrotron radiation is required for the observation of strains in micron thick films.

The rocking curve measurements of the (001) and (002) Bragg reflections at $\theta \approx 2.95°$ and $\theta \approx 5.89°$ respectively were performed. Figure 6.15 shows the rocking curve of the (002) YBCO Bragg reflection. The best fit of the profile consists of three distinct peaks: a strong Lorentzian peak with resolution-limited width along the direction of the GIXR specular ridge (peak I), a weak reflection along the direction of YBCO high-order Bragg reflections (peak II) and another even weaker one along the direction of STO lattice axis (peak III). Table 6.3 lists the parameters of these reflections including amplitude, position, width and the integrated intensity. The same result is also observed near the (001) YBCO Bragg reflection. Because peak II is along the same direction with those high-index Bragg reflections, it indicates that they are from the same mosaic YBCO grains. As a result, the FWHM of the (001) and (002) Bragg reflections in Figure 6.5 are obtained by measuring the FWHM from the best fit of this component.

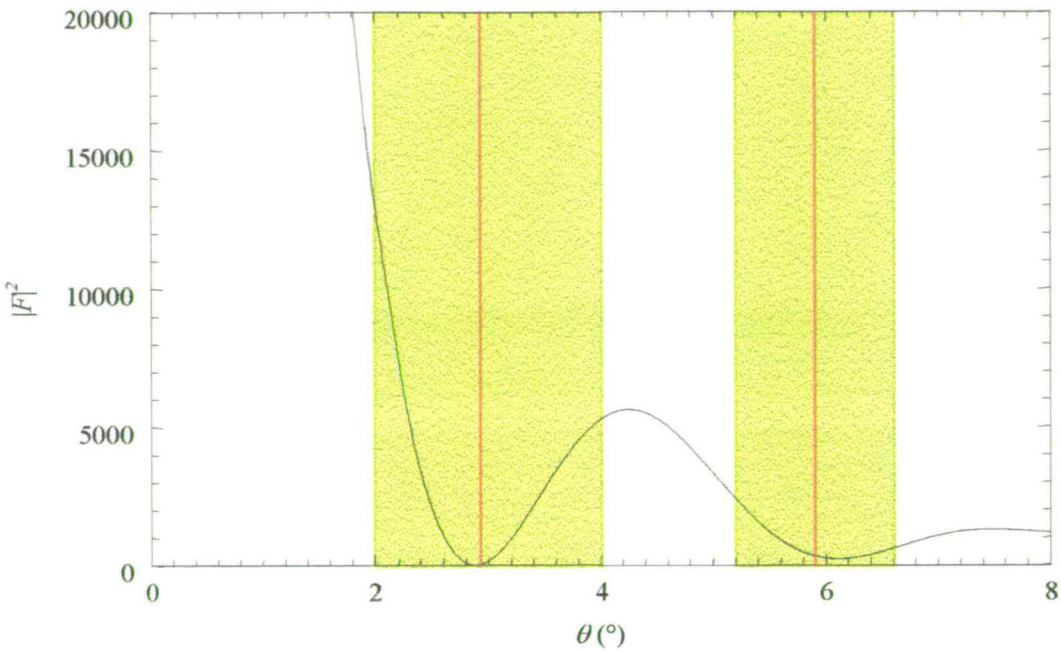

(a)

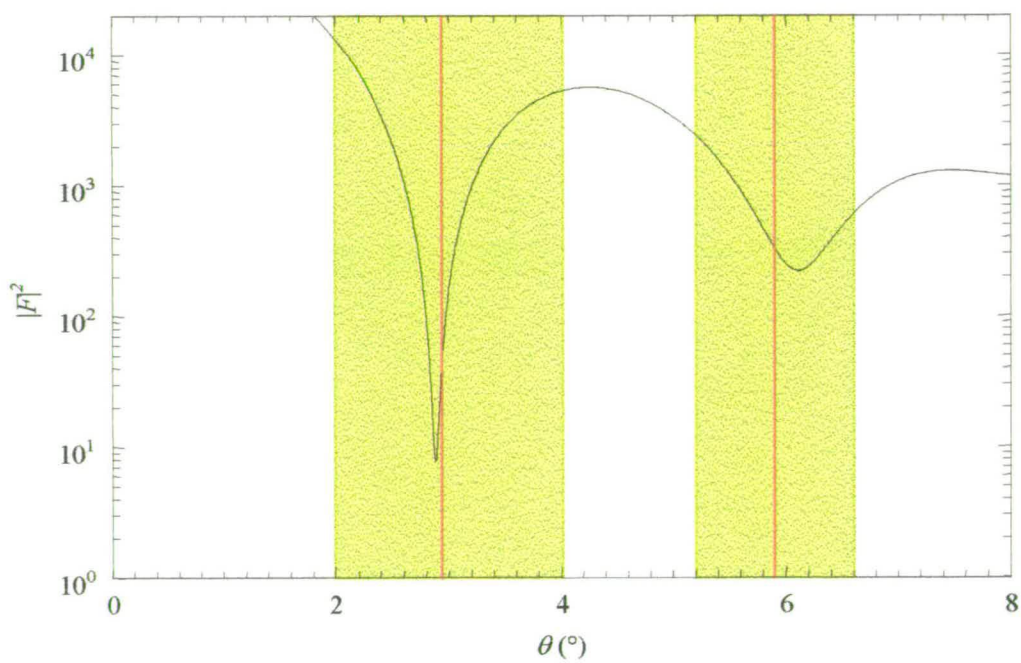

(b)

Figure 6.9 The variation of the squared structure factor for a YBCO crystal (a) in linear scale and (b) in logarithmic scale. The red lines point out the (001) and the (002) Bragg reflection positions and the green areas present the angular range of the CTR profiles.

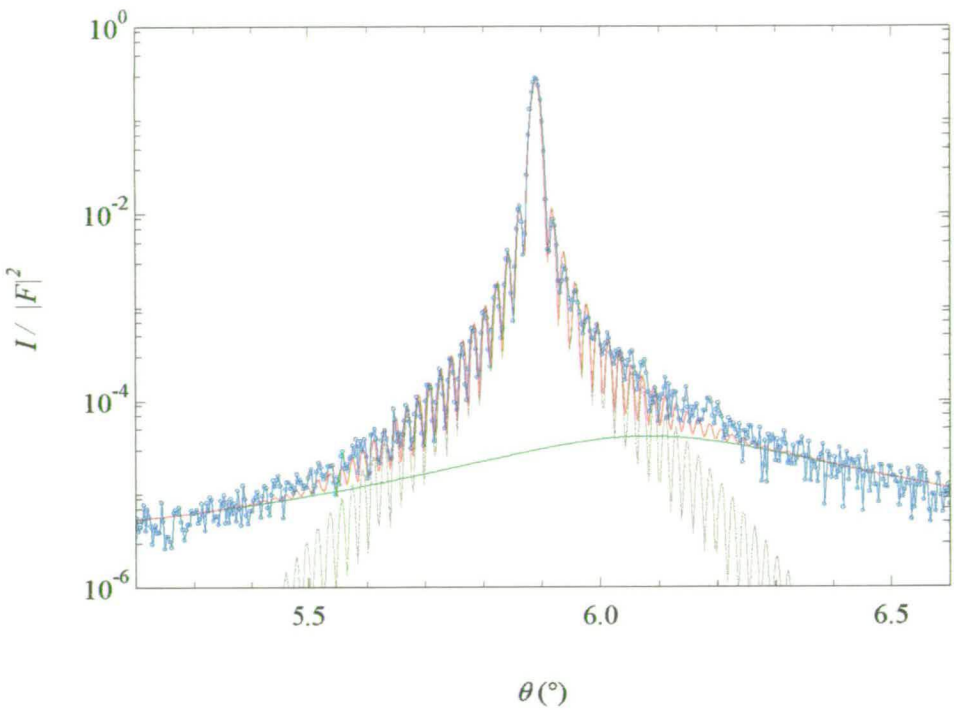

Figure 6.10 The best fit of the θ-2θ scan of the (002) Bragg reflection. No strain is assumed in this fit. The blue dots/line is the experimental data corrected by the structure factor variation. The red line is the best fitting result. The grey and green lines are the true diffraction profile and the background intensity respectively.

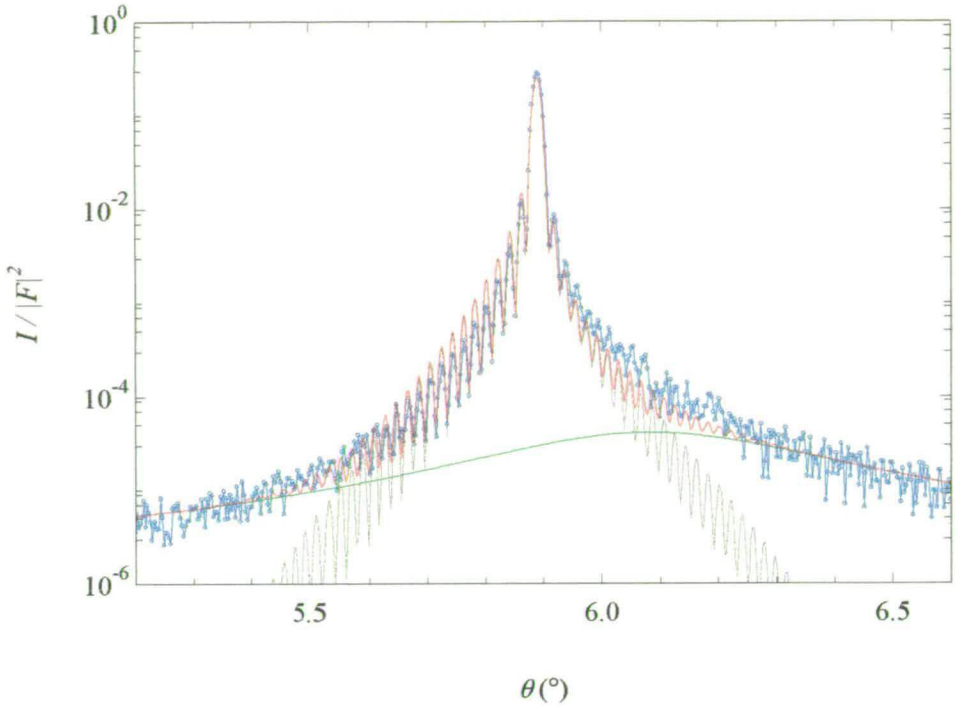

(a)

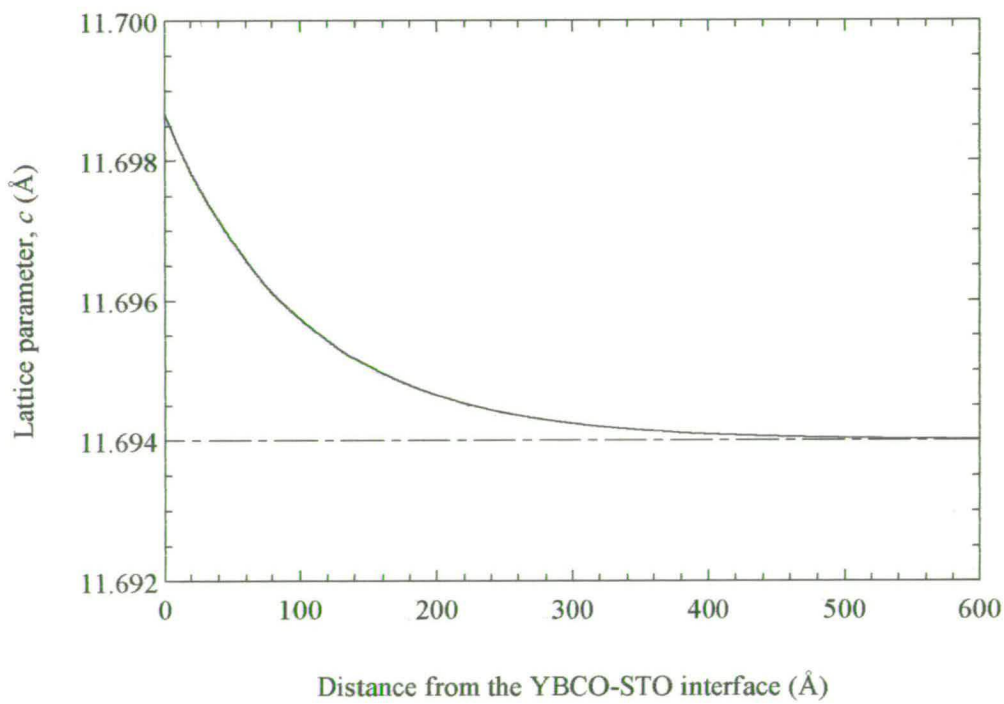

(b)

Figure 6.11 (a) the best fit from the sample with a strain field close to the interface. The blue dots/line is the experiment data. The red line is the best fit. The grey and green lines are the true CTR profile and the linear intensity background. (b) the bottom strain field as revealed by the parameters obtained from the fit shown above.

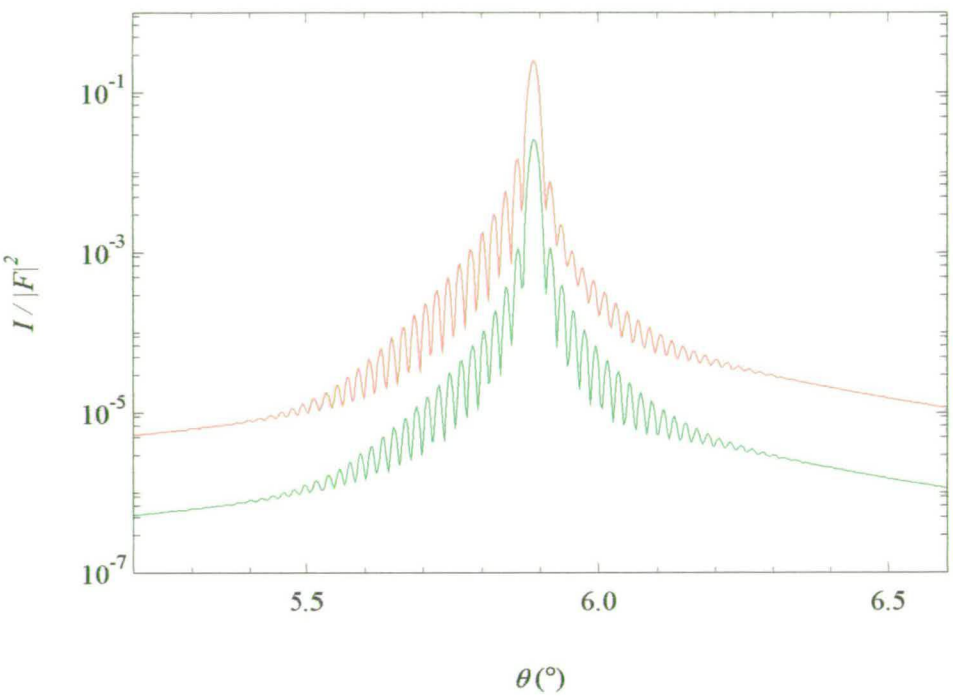

Figure 6.12 Simulation results of the (002) Bragg reflection profiles with the strain close to the interface (red line) and close to the surface (green line) using identical parameters. The simulation from the surface-strain sample has been divided by a factor of 10.

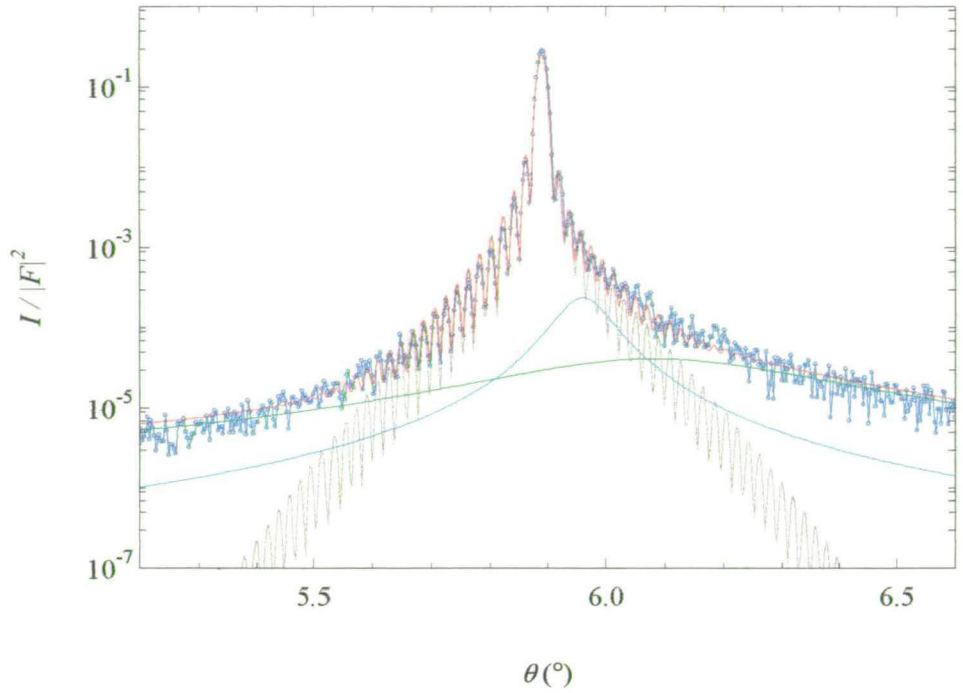

(a)

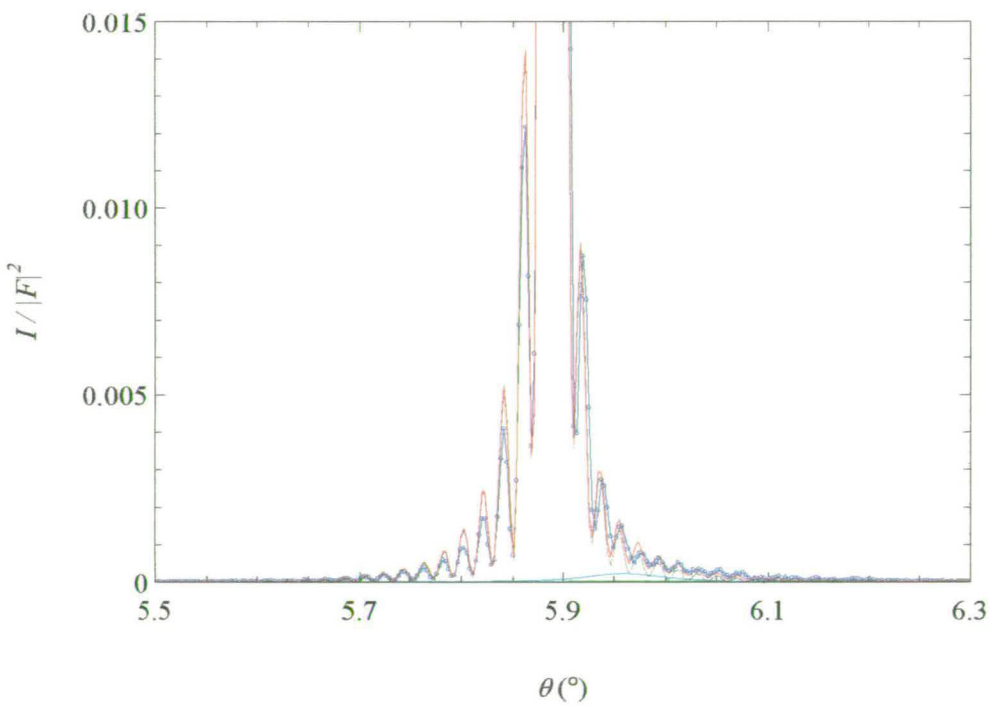

(b)

Figure 6.13 The best fit with an interface strain field and an extra layer (a) logarithmic scale and (b) linear scale (enlarged). The blue dots/line is the experimental data. The red line is the best fit. The grey, light blue and the green lines are the true CTR profile, the weak extra reflection and the linear intensity background respectively.

Table 6.2 The best fitting parameters obtained from the θ-2θ scan around the (002) Bragg reflection

Thickness	H	1801±1Å
Penetration depth	ξ	6000Å
Roughness	σ	27±2Å
Strain magnitude	$\Delta = \frac{\Delta c}{c}$	0.04±0.01%
Relaxation distance	$n_{1/2}$	6±1 layers
Scattering angle of extra reflection	θ_{extra}	5.96±0.05°
FWHM of the extra reflection	B_{extra}	0.1±0.05°
Error	χ^2	0.2058

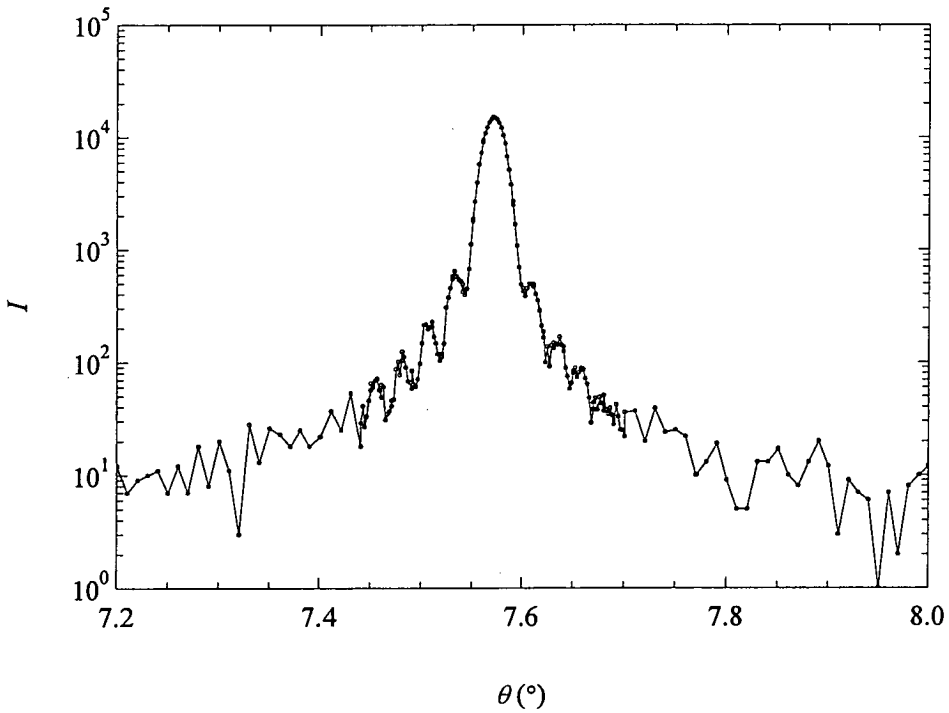

Figure 6.14 The CTR profile of the (002) Bragg reflection of the same YBCO-STO sample using CPEX system.

The resolution-limited peak indicates that part of the YBCO thin film is highly coherent along the surface parallel direction and the *c*-axis of the component is parallel to surface/interface normal. Their width indicates that the coherence length of these components is compatible with the coherence length of the x-ray source, on the order of a few microns. It is also found that the Laue finite size fringes are

associated with this peak, indicating that the film is highly perfect in all three dimensions. Similar features, in which both short-range and long-range correlation coexisting in a film, has been reported by many groups[27,28,29,30,31,32,33]. Reimer et al. found two different components with different correlation lengths in niobium thin films grown on sapphire substrates[30]. The lateral correlation length of the high quality film was to be 29000Å and coupled to the substrates while the broad reflections come from some "bulk like" portion. However, this two-component phenomenon is only observed in "out-of plane" reflections (along the Q_z direction), not in the "in-plane" reflections (using GIXD experiments). They concluded that "the narrow component of the out-of-plane (110) peak is due to the parallel alignment of the (110) *planes* over a much larger length scale than the position correlation of the Nb atoms *within* the (110) planes"[30]. The Laue finite size fringes were not observed in this report. Gibaud et al. also reported the two-component mixture phase in niobium thin films grown on sapphire[32]. The lateral correlation of the high quality film is measured to be 65000Å. In their model, the surface/interface roughness was considered by multiplying the Laue function, $\frac{\sin^2(nx)}{\sin^2(x)}$, with the roughness factor, $\exp\left(-q^2\sigma^2\right)$ [10]. However, the results showed that there was no roughness in their sample. They found that the high quality films were coupled with the sapphire substrates and that the large correlation length (65000Å) was related to the size of the surface terrace. They also examined the broad reflection and found the profiles were consistent with the Lorentzian square peak shape. Therefore, they concluded that "the broad diffuse transverse peak arises from deviations of the niobium planes away from their average structure"[32]. Miceli et al. employed a different model to study the two-component phase in ErAs/GaAs thin films[29]. They adopted the partial correlated roughness model for superlattice material from the GIXR analysis. Like the correlated roughness in superlattices, the surface roughness of the substrate replicates through the lattice plane in high-quality single-crystal films or interfaces of a superlattice. The scattering cross section is automatically separated into specular and diffuse components. The roughness factor is now $\exp(-Q^2\sigma^2)$ which suppresses the intensity of the CTR ridge. This result is different from the one of Gibaud et al. because it is the *reduced wave vector*, q, used in their roughness factor. The variation

of the roughness factor directly leads to a conclusion that "the sharp feature is not observed at high-order Bragg reflections"[29]. The existence of the roughness also affects the diffuse component because the energy in specular reflection is scattered into the diffuse component. In the report by Reimer et al., they reported that the volume of the high-quality film is estimated to be about 10% of the total volume. This is arguable since the effect of roughness was not included, which reduces the observed intensity of the reflections from the high-quality films. The volume fraction of high-quality film would thus be much higher than 10%.

Figure 6.16 shows the intensity decay of the sharp component of the (001) and (002) reflections and their best fit. The intensity is normalised by the integrated intensity of components II because peak II comes from mosaic grains which are not affected from the roughness. The fit indicates that the ratio between the integrated intensity of peak I and the integrated intensity of peak II is about $3.5:0.2$. This is obtained by extrapolation of the intensities to $\theta = 0°$, to avoid the effects of roughness which will cause the intensity of peak I to reduce quickly. Since the integrated intensity of different components is proportional to their volume, the results indicate that the ultra-high-quality YBCO film caused by the sharp reflection occupies nearly 95% of the thin film volume. Nevertheless, due to the roughness effect, the reflection intensity reduces very fast which prevents the observation of this ultra-high-quality film at higher angles. The scattering from this ultra-high-quality film can not be observed around the (003) Bragg reflection because of the presence of intense scattering from the (001) substrate Bragg reflection. For YBCO, the structure of the (004) reflection is extremely small rendering observation impossible. For higher angles, the intensity reduction caused by the high roughness precludes observation and only the broad component (peak II) is observed. Thus, the peaks associated with this ultra high quality phase are only observable at the (001) and (002) reflection. The roughness causing the intensity decay is measured to be about 11Å. Because of the few measurement results, the fit is very unreliable. However, the RMS roughness is close to the lattice parameter of YBCO crystal surface which suggests that the film is grown on YBCO and the surface disorder terrace of YBCO the layer is replicated to this ultra-high-quality YBCO film.

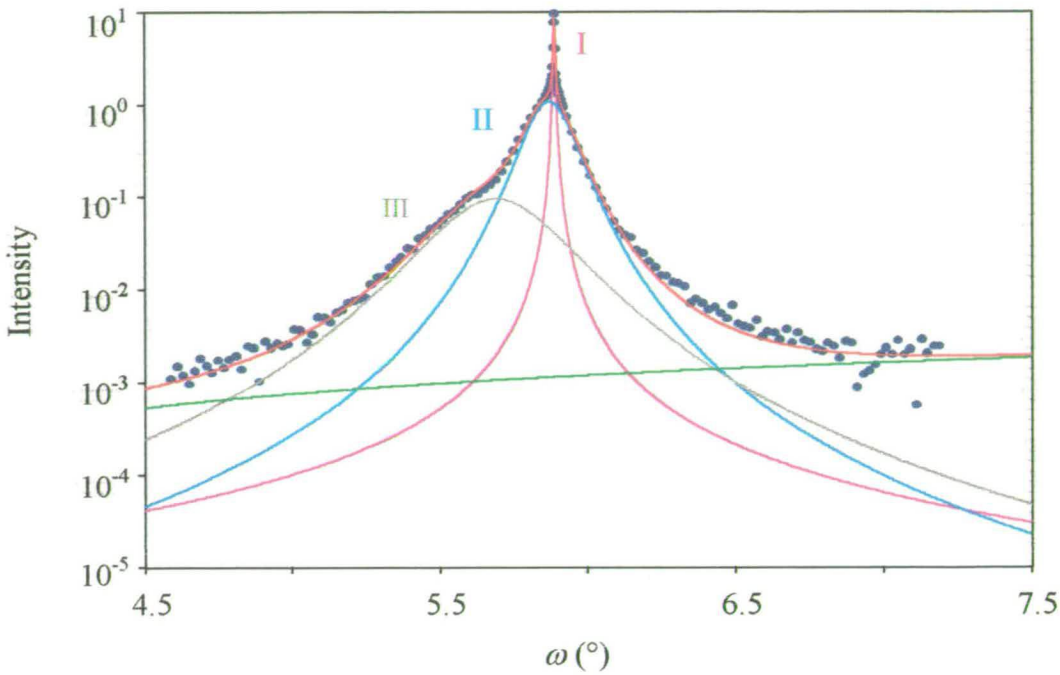

(a)

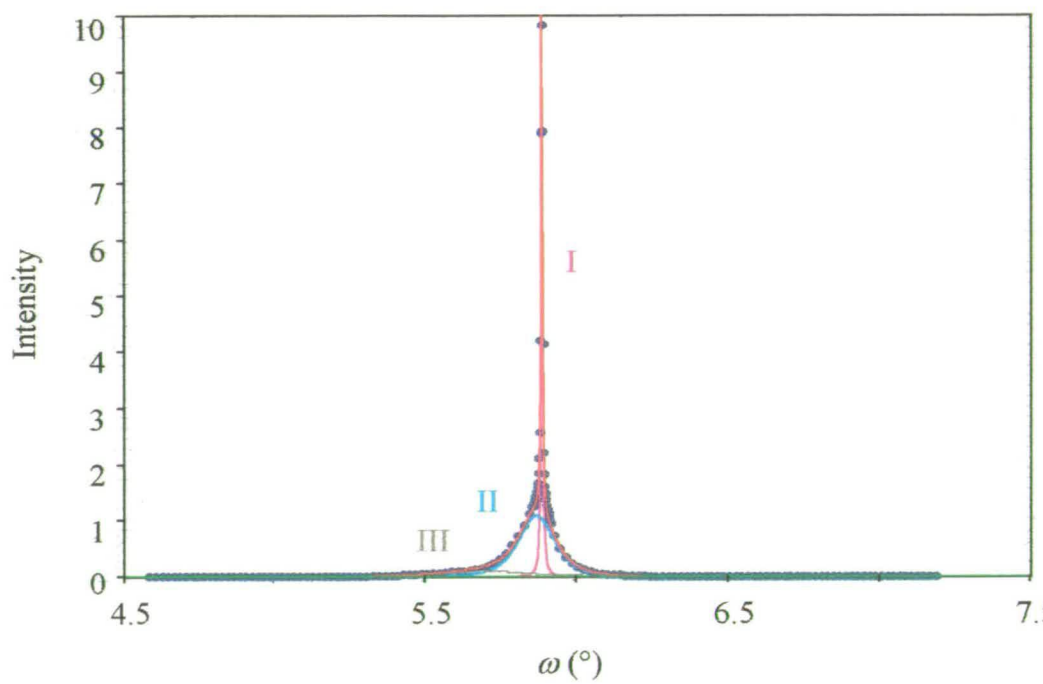

(b)

Figure 6.15 The rocking curve of the (002) YBCO Bragg reflection. The blue dots represent the experimental data. The red line is the best fitting result. The pink, light blue, grey lines are the three peaks observed labelled by I, II and III. A linear background was assumed in the fit and represented by the green line.

Table 6.3 The best fit parameters of the (002) Bragg reflection rocking curve.

	Amplitude (I_0)	Position (θ_0)	FWHM	Integrated intensity
Peak I	9.212	5.888°	0.0059°	0.0852
Peak II	1.093	5.870°	0.1428°	0.1904
Peak III	0.096	5.689°	0.3526°	0.0411

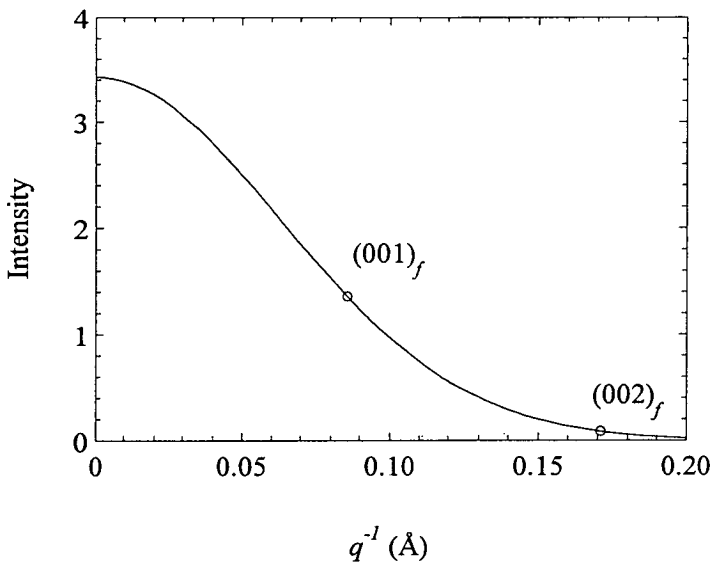

Figure 6.16 The diffracted intensity of the ultra-high-quality YBCO thin film.

The third peak of YBCO thin film observed, as shown in Figure 6.15 on the low angle shoulder of peak II is much weaker than the previous two peaks. Its reciprocal space vector is along the substrate lattice axis, which suggests that the film is epitaxial to the substrate. The larger width suggests poor quality or an extremely thin layer. It can be concluded that a thin layer of mosaic epitaxial film is grown firstly above the STO substrate as a buffer layer. It is likely that this peak is associated with the weak broad peak found in the θ-2θ scans around the (002) reflection. The parameters obtained from both scans profiles are different, probably because of the large error associated with fitting such a broad weak peak close to other strong reflections. The ultra-high-quality film (peak I) is grown afterwards, together with some mosaic inclusions (peak II). From the variation of the thickness derived from different measurements shown in Table 6.4, the thickness of this YBCO buffer layer is a few hundred Å or less. Slight inconsistency is found in that the film thickness is

different in the low angle reflectivity measurement than that from the Bragg reflection scans. For Bragg reflections with different order, those of lower order the low order reflection is much tolerant to the uncertainty of the lattice parameter, or the crystalline quality. Therefore, the thickness measured from low index Bragg reflections is larger. As the GIXR, because it measures the (000) Bragg reflection and is completely insensitive to the crystal structure, the thickness measured from GIXR is the largest. The same argument is applicable for roughness measurements[31]. A schematic drawing of the intensity distribution within low angle regime is shown in Figure 6.17. q_I , q_{II} and q_{III} are the directions of different diffraction maxima observed in Figure 6.15 denoted as peak I, II and III. For YBCO Bragg reflections of order 3 and after, only peak II can be found and no evidence of Laue fringes. The angle between q_I and q_{II} is 0.018° which is the surface terrace angle of the ultra-high-quality YBCO thin film. The angle between q_I and q_{III} is 0.199° which is the surface mis-cut angle of the STO substrate and this is consistent with the results of Section 6.3.2.

The evidence for the existence of the ultra-high-quality YBCO film has also been found in some YBCO-STO samples grown by DC sputtering deposition. However, they have never been observed at the YBCO thin film grown on $LaAlO_3$ or yittra stabilised zirconia (YSZ) substrates regardless of their growth techniques. This suggests the formation of the ultra-high-quality single crystal YBCO thin film is highly related to the lattice miss-match between the YBCO thin film and the substrates.

Table 6.4 The thickness of the YBCO thin film according to x-ray scattering measurement of Bragg reflections of different order

Reflection index	(000)	(001)	(002)
Measurement	GIXR	Laue fringes	Laue fringes
Thickness	1930Å	1836Å	1801Å

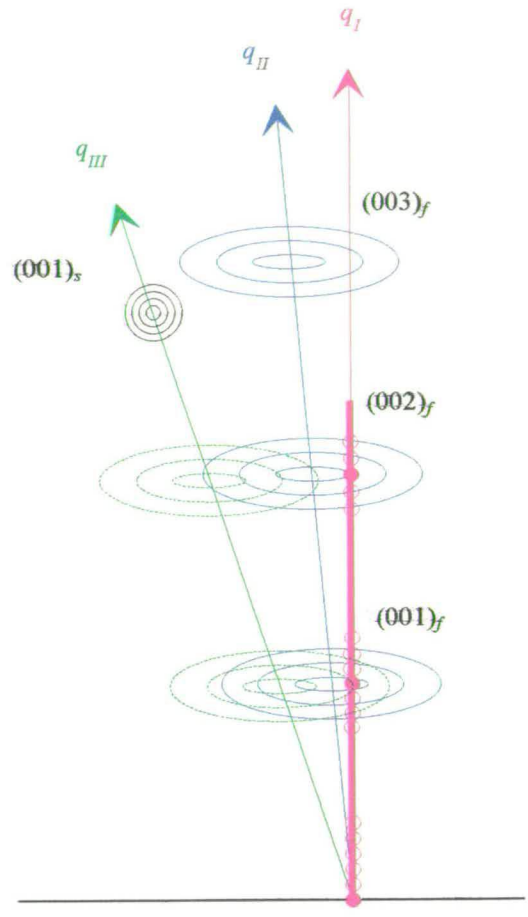

Figure 6.17 The schematic drawing of the reciprocal space map within the low angle regime. The Bragg reflections from the YBCO thin film and the STO substrate are represents by the contours. The pink arrow, denoted as q_I, is the direction of the surface and interface normal. The bold pink line shows the whole specular ridge (or CTR). The solid dots indicate the reflection maxima of the $(000)_f$ (the surface total reflection), $(001)_f$ and $(002)_f$ reflections. The empty dots represent the Keissig fringes and Laue fringes which relate to the thickness of the film. Blue contour maxima along direction q_{II} represent the YBCO Bragg reflection from the mosaic component of the film. The green arrow, denoted as q_{III}, represents the crystal axis of the STO substrate. The green contours on q_{III} represent the Bragg reflection of the YBCO buffer layer and the black contours represent the $(001)_s$ reflection.

6.4 Conclusion and further work

A schematic drawing of the crystal structure of the YBCO-STO thin film is shown in Figure 6.18. At the early stage of growth, because of the small lattice mis-match between YBCO and STO, a thin epitaxial YBCO layer (green layer) with a high dislocation density is formed. The thickness of this layer can be estimated by the difference of the thickness measured by GIXR and CTR and it is at most a few hundred Å thick. The large peak width of the Bragg reflections and inconsistency of the thickness derived from various Bragg reflections suggest that the crystal quality and orientation within this layer might be depth dependent. The major film consists of two different parts. Nearly 95% volume of the YBCO film is composed of the ultra-high-quality YBCO crystal (red layer) with a micron-size lateral correlation length and completely correlated vertically. This film is virtually a high-quality single crystal but has never been reported before principally because the correlated roughness cause the intensity of the Bragg reflections to reduce quickly with scattering angle. Thus, it can only be observed around the lowest angle reflections ((001) and (002) reflections). The second part of the YBCO film, with ~5% volume, consists of mosaic YBCO inclusion grains (blue cluster) with grain size of ~100Å vertically and ~2500Å laterally which randomly distribute within the ultra-high-quality YBCO film. On top of the YBCO film, a disordered oxidation layer (orange layer) is formed and was found in the GIXR measurements. There is no evidence to indicate that this oxidation layer is crystalline.

Surprisingly, the results of this experiment suggest that only ~5% volume of the YBCO film can be explored by measuring the high-order Bragg reflections, which is often the routine characterisation procedure. The true information concerning nearly 95% volume of the film is to be found only in the low index Bragg reflections. Although it is reasonable to assume that if the quality of YBCO inclusions is good then the quality of single crystal films is also good, it is difficult to find the relationship between its properties and this ill-defined crystal quality indicator.

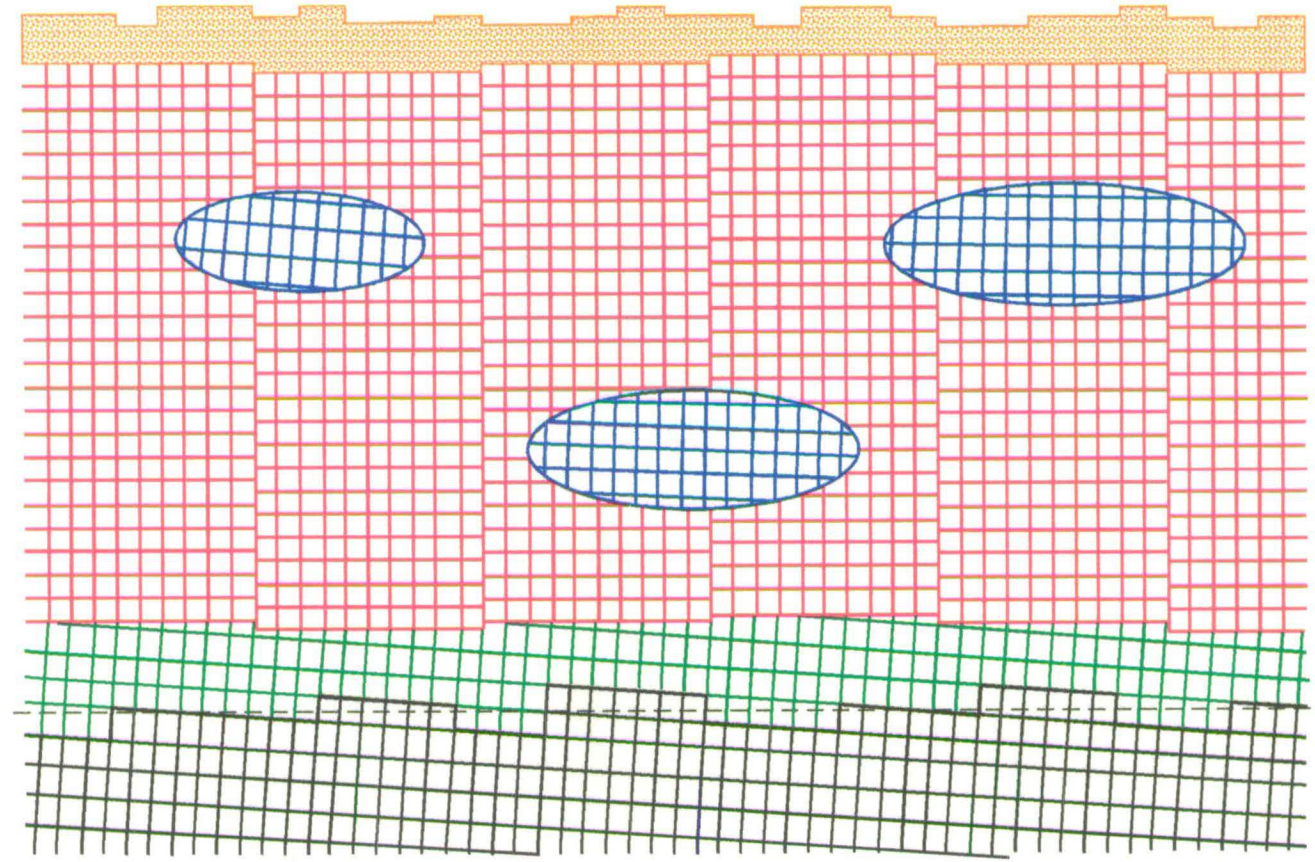

Figure 6.18 The schematic drawing of the crystal structure of the YBCO-STO thin film. The lines represent the lattice planes and the colours represent different crystal structure regime. black: STO substrate; green: YBCO buffer layer; red: ultra-high-quality YBCO film; blue: mosaic YBCO inclusion; brown: disordered surface oxidation layer.

Similar results of co-existence of the long-range and short-range order in thin film systems have been reported in many papers[27,28,29,30,31,32,33,34,35]. However, it has never been reported previously in high-T_c superconductors. There are two major difficulties which obscure the observation. Firstly, this phenomenon only occurs in perfect epitaxial films, which are not always been available in high-T_c superconductors. As mentioned before, we have only observed this phenomenon in the YBCO-STO system. Secondly, the observation of this phenomenon strongly depends on the roughness of the interface and the lattice planes. This is generally not a big problem for semiconducting systems[27,28,29,34,35]. However, for system with large roughness, such as the high-T_c superconductors, it is difficult to measure the diffraction intensity because the Debye-Waller like decay factor reduces the scattered intensity very fast. Even in our YBCO-STO sample, which is one of the best samples obtainable, the reflection from the ultra-high-quality film can only be observed at the (001) and (002) reflections.

Although this is only the first observation of ultra-high-quality YBCO thin film, it is obvious that the ultra-high-quality YBCO film should dominate the superconductivity rather than the mosaic inclusion. There might be some direct link between the structural parameters of this ultra-high-quality film and the superconductivity. Therefore, low-index Bragg reflection profiles need to be considered carefully on examining the quality of near perfect high-T_c thin film superconductors. Because this type of film is the best single crystal high-T_c superconductor, it will be the doorway to understanding high-T_c superconductivity. It is indeed possible that the very much higher critical currents obtainable with thin film maybe related to the presence of such high quality films, which is not obtainable in the bulk material. Furthermore, the control of the fabrication of this type of film will also help to advance industrial applications.

[1] S.K.Sinha, E.B.Sirota, S.Garoff, and H.B.Stanley, Phys. Rev. B **38**, 2297 (1988)

[2] C.A.Lucas, P.D.Hatton, S.Bates, T.W.Ryan, S.Miles, and B.K.Tanner, J. Appl. Phys. **63**, 1936 (1988)

[3] V.Holy, J.Kubena, I.Ohlida, K.Lischka, and W.Plotz, Phys. Rev. B **47**, 15896 (1996)

[4] S.F.Cui, G.M.Luo, M.Li, Z.H.Mai, Q.Cui, J.M.Zhou, X.M.Jiang, and W.L.Zhang, J. Phys.: Condens. Matter **9**, 2891 (1997)

[5] M.Y.Chern, A.Gupta, B.W.Hussey, Appl. Phys. Lett. **60**, 3045 (1992)

[6] S.Williams, J.Q.Zheng, M.C.Shih, X.K.Wang, S.J.Lee, E.D.Rippert, S.Maglic, T.Roberts, Y.Lin, R.T.Kampworth, and K.Gray, J. Appl. Phys. **72**, 4798 (1992)

[7] H.Asami, Y.Watanabe, Jpn. J. Appl. Phys. **33**, L1073 (1994)

[8] T.S.Gau, S.L.Chang, H.H.Hung, C.H.Lee, T.W.Huang, H.B.Lu, S.J.Yang, and S.E.Hsu, Appl. Phys. Lett. **65**, 1720 (1994)

[9] A.Ichinose, and A.Shirabe, Physica C **277**, 243 (1997)

[10] S.R.Andrews, and R.A.Cowley, J. Phys. C: Solid State Phys. **18**, 6427 (1985)

[11] I.K.Robinson, Phys. Rev. B **33**, 3830 (1986)

[12] T.Terashima, Y.Bando, K.Iijima, K.Yamamoto, K.Hirata, K.Kamigaki, and H.Terauchi, Physica C **162-164**, 615 (1989)

[13] T.Terashima, Y.Bando, K.Iijima, K.Yamamoto, K.Hirata, K.Hayashi, K.Kamigaki, and H.Terauchi, Phys. Rev. Lett. **65**, 2684 (1990)

[14] K.Kamigaki, H.Terauchi, T.Terashima, Y.Bando, K.Iijima, K.Yamamoto, K.Hirata, K.Hayashi, I.Nakagawa, and Y.Tomii, J. Appl. Phys. **69**, 3653 (1991)

[15] O.Nakamura, E.E.Fullerton, J.Guimpel, and I.K.Schuller, Appl. Phys. Lett. **60**, 120 (1992)

[16] The subscript letters specify the lattice system: "*f*" means thin film lattice system and "*s*" means substrate system.

[17] D.Chrzan, and P.Dutta, J. Appl. Phys. **59**, 1504 (1986)

[18] S.E.Russek, S.C.Sanders, A.Roshko, and J.W.Ekin, Appl. Phys. Lett. **64**, 3649 (1994)

[19] J.H.Li, W.J.Lin, P.D.Hatton, Z.M.Mai, and S.F.Xu, Physica C **245**, 139 (1995)

[20] B.E.Warren, *X-ray diffraction*, pp.251 (Dover, 1990)

[21] T.S.Argunova, R.N.Kyutt, M.P.Scheglov, and N.N.Faleev, J. Phys. D: Appl. Phys. **28**, A212 (1995)

[22] P.Y.Chu, R.C.Buchanan, F.Gao, J.W.Kruse, and M.Feng, Appl. Phys. Lett. **63**, 3512 (1993)

[23] From Figure 6.10 to Figure 6.13, the geometry factors, $I/|F|^2$, are obtained by correcting the scattered intensity measurement divided the square modulus of the structure factor at the same angle. Therefore, the backgrounds of the geometry factors are also corrected with the structure factors and this makes non-linear background of the geometry factors.

[24] P.F.Fewster, J. Appl. Cryst. **25**, 714 (1992)

[25] X.G.He, M.Erdtmann, R.Williams, S.Kim, and M.Razeghi, Appl. Phys. Lett. **65**, 2812 (1994)

[26] K.Asai, K.Kamei, and H.Katahama, Appl. Phys. Lett. **71**, 701 (1997)

[27] P.F.Miceli, C.J.Palmstrom, and K.W.Moyer, Appl. Phys. Lett. **58**, 1602 (1991)

[28] P.F.Miceli, C.J.Palmstrom, and K.W.Moyer, Appl. Phys. Lett. **61**, 2060 (1992)

[29] P.F.Miceli, and C.J.Palmstrom, Phys. Rev. B **51**, 5506 (1995)

[30] P.M.Reimer, H.Zabel, C.P.Flynn, and J.A.Dura, Phys. Rev. B **45**, 11426 (1992)

[31] A.Stierle, A.Abromeit, N.Metoki, and H.Zabel, J. Appl. Phys. **73**, 4804 (1993)

[32] A.Gibaud, R.A.Cowley, D.F.McMorrow, R.C.C.Ward, and M.R.Wells, Phys. Rev. B **48**, 14463 (1993)

[33] A.Gibaud, D.F.McMorrow, and R.A.Cowley, Physica B **198**, 63 (1994)

[34] P.Kidd, P.F.Fewster, N.L.Andrew and, D.J.Dunstan, Microsc. Semicond. Mater. **134**, 585 (1993)

[35] P.Kidd, P.F.Fewster, and N.L.Andrew, J. Phys. D: Appl. Phys. **28**, A133 (1995)

Appendix

Published Works

Reprinted from

PHYSICA C

Physica C 245 (1995) 139–142

Triple-axis X-ray diffraction analysis of highly oriented $YBa_2Cu_3O_7$ thin films on $LaAlO_3$ substrates

J.H. Li [a,*], W.-J. Lin [b], P.D. Hatton [b], Z.H. Mai [a], S.F. Xu [a]

[a] *Institute of Physics, Chinese Academy of Sciences, PO. Box 603, Beijing 100080, China*
[b] *Department of Physics, The University of Edinburgh, Edinburgh EH9 3JZ, UK*

Received 28 September 1994; revised manuscript received 7 February 1995

ELSEVIER

energy density of the laser was about 3–5 J/cm^2 and the spot size of the beam was 3 mm^2. The surface temperature of the substrate was maintained at 770°C during the deposition process. The substrate–target distance was 40 mm. Before starting the deposition, 600 mTorr oxygen was passed through the chamber and the flux remained constant during the whole process. The substrate used were commercial $LaAlO_3$ wafers which have been mechanically polished already and have been chemically cleaned prior to the film deposition. Both samples have a sharp superconducting transition temperature around 90 K and a critical current density, J_c, in the range of $4.0–6.5 \times 10^6$ A/cm^2.

X-ray measurements were carried out on a four-circle diffractometer based on a Huber 430/440 goniometer with Cu Kα_1 radiation. The incident and diffracted radiation were collimated by reflections from high-quality germanium (111) crystals which give an in-plane resolution of 5×10^{-5} nm^{-1}. Reciprocal space maps around the substrate (002) reciprocal lattice point (RLP) and rocking curves through both the substrate and the film RLPs were recorded.

3. Results and discussion

Fig. 1 shows a two-dimensional isointensity contour map around the substrate (002) RLP measured from sample 1. Two distinct reflection peaks are clearly observed, i.e. an intense substrate (002) reflection and a weaker reflection at (0 0 1.944) corresponding to the (006) reflection of the thin film. Similar results were observed around other reciprocal-lattice points. It is already known that the feature of a RLP contains the information of the crystal defects [6,7]. We noticed that the substrate (002) RLP is asymmetrical in the direction of the surface normal which, in general, is an indication that the substrate contains a gradually changed lattice plane spacing. The thin-film (006) RLP is broadened along the [100] direction suggesting that the film has a mosaic-like structure containing a lot of crystal grains with random orientation. As mentioned in Section 1, high-angle grain boundaries will degrade the electronic performance of the films and therefore we wish to reduce it. For this sample, the mean grain-boundary angle can be roughly estimated from the full width at half maximum (FWHM) of the rocking curve shown in Fig. 2 to be less than 0.3°. It is a bit larger compared with the value reported by Chu et al. [8], but may be caused by ignoring the broadening effect of a thinner film and by the reason discussed below. Even so, this value is still much smaller than that reported by Cukanskas et al. [9].

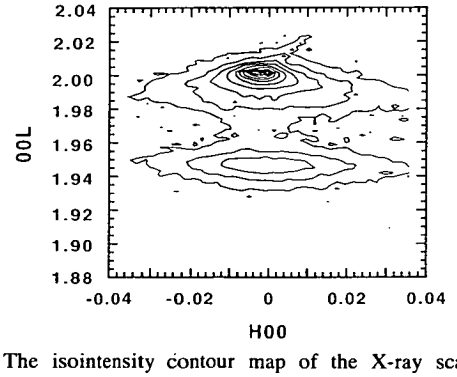

Fig. 1. The isointensity contour map of the X-ray scattering intensity around the substrate (002) reciprocal-lattice point of sample 1.

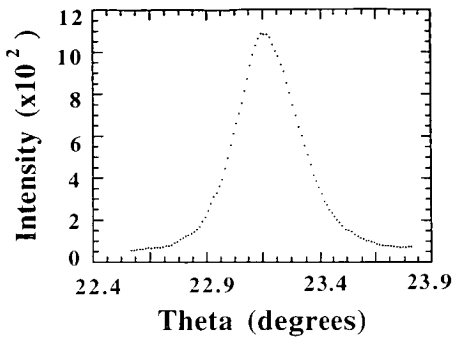

Fig. 2. The X-ray triple-axis diffraction rocking curve of sample 1 through the superconducting film (006) reciprocal-lattice point.

Fig. 3 shows a measured (002) reciprocal-space map of sample 2. The broadening of the substrate RLP in the [001] direction and the broadening of the film (006) RLP in the [100] direction are similar to that of sample 1, whereas the substrate RLP, contrary to sample 1, has split into two peaks, which indicates that the substrate is twinned. Such a twin structure has been known to be generated during a cubic–rhombohedral phase transition of $LaAlO_3$ at

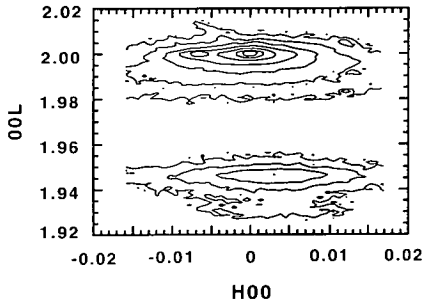

Fig. 3. The isointensity contour map of the X-ray scattering intensity around the substrate (002) reciprocal-lattice point of sample 2.

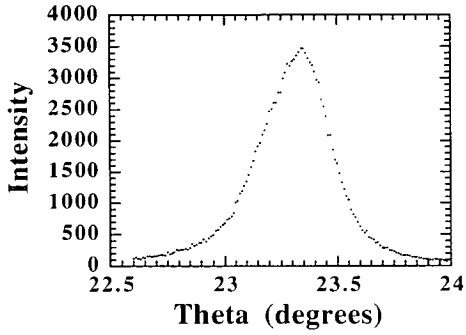

Fig. 5. The X-ray triple-axis diffraction rocking curve of sample 2 through the superconducting film (006) reciprocal-lattice point.

520°C [10]. It is also clear from the map that there exists a misorientation between the film and the substrate (indicated by the off-set of the film RLP with respect to that of the substrate). The rocking curves through the substrate and the film RLPs are shown in Figs. 4 and 5, respectively. The substrate rocking curve contains two peaks separated by 0.18° which is caused by the twinning structure. The film rocking curve, contrary to Fig. 2 of sample 1, is obviously asymmetrical due to the overlapping of the two peaks caused by the epitaxial growth of the film on the twinned substrate. The FWHM of this rocking curve is about 0.36° indicating that the mean grain-boundary angle for this sample is better than 0.18°. In Fig. 1, the substrate RLP is also a bit broadened along the [100] direction indicating a possible small-angle twin structure. This also causes the film rocking curve to be broadened and, consequently, the grain-boundary angle to be estimated a bit larger.

By comparison with our previous studies on YBCO thin films grown on $SrTiO_3$ and $LaAlO_3$ substrates by DC magnetron sputtering [11,12], where a third peak arising from a/b oriented grains was observed between the substrate (002) RLP and the film (006) RLP, we found that there is no evidence showing the existence of the a/b oriented grains in both samples studied in this work. To clarify this, a one-dimensional longitudinal scan about substrate (002) RLP of sample 2 was performed and the result is shown in Fig. 6. No distinguishable peak from a/b oriented grains can be observed as previously found at (0 0 1.9745) [11]. The possibility that the asymmetry of the substrate peak is caused by the existence of some a/b oriented grains can also be excluded by the corresponding scan of the $LaAlO_3$ substrate prior to the film deposition as shown in Fig. 7, which is exactly the same as the substrate peak in Fig. 6. The asymmetry of this peak is then an

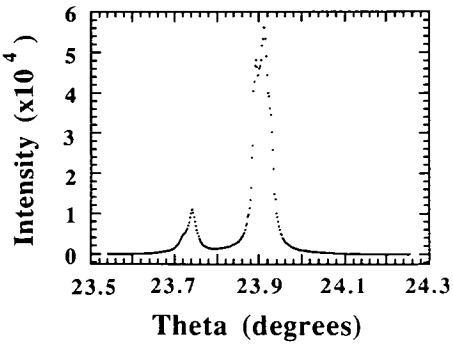

Fig. 4. The X-ray triple-axis diffraction rocking curve of sample 2 through the substrate (002) reciprocal-lattice point.

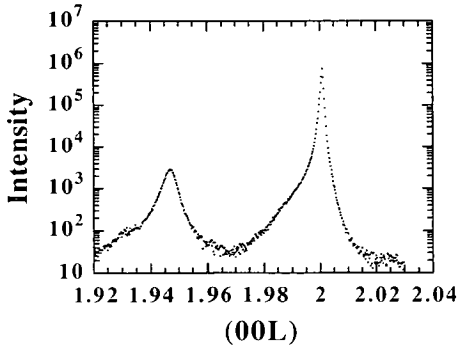

Fig. 6. The longitudinal scan profile about the substrate (002) reciprocal-lattice point of sample 2.

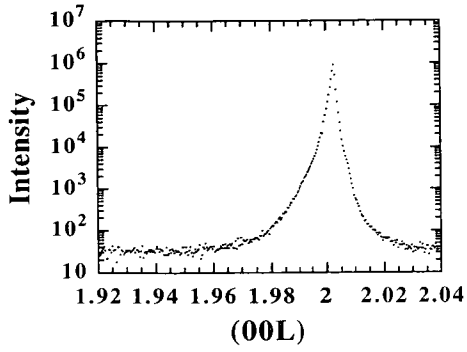

Fig. 7. The longitudinal scan profile about the (002) reciprocal-lattice point of the $LaAlO_3$ wafer without YBCO film having been deposited.

indication that considerable strains exist on the substrate surface caused by the mechanical polishing. Our result is inconsistent with Carim et al. who reported that for PLD deposited YBCO films there were only a few a/b oriented grains if the film thickness is under 400 nm [13]. However, some other studies showed that both c and a/b oriented grains may coexist in even thinner PLD deposited films on $SrTiO_3$ substrates [14–16]. Meanwhile, many studies on YBCO thin films deposited on $LaAlO_3$ and/or $SrTiO_3$ substrates by a DC magnetron sputtering technique demonstrated that the films are usually mixtures of c and a/b oriented grains [11,12,17,18]. Due to the lack of strain analysis in these works, we cannot exclude the possibility that the formation of nearly pure c oriented YBCO films on $LaAlO_3$ substrates is caused by the surface strain enhanced epitaxial. In other words, it seems more difficult for a/b oriented YBCO grains to nucleate on the surface of a $LaAlO_3$ substrate than on a $SrTiO_3$ substrate because there is a larger difference between the c-axis length of the YBCO unit cell and three times of the $LaAlO_3$ substrate lattice constant (about 0.3% for $SrTiO_3$ and 2.8% for $LaAlO_3$, respectively). The surface strain on the $LaAlO_3$ substrates enlarged this difference and probably resulted in the absence of a/b oriented grains in the films.

4. Conclusion

High-resolution X-ray reciprocal-space mapping has been used to study the YBCO thin films deposited on $LaAlO_3$ substrates by a pulsed laser deposition technique. We found that there are nearly no a/b oriented grains in the films, while the substrate suffers from a considerable surface strain. We doubt that the substrate surface strain played an important role in the formation of the highly c oriented films, but further experimental confirmations are required.

Acknowledgements

This project is partially financial supported by the Chinese Academy of Sciences and the Engineering Research Council, the Royal Society.

References

[1] W. Hartwig and C. Passcow, in: Applied Superconductivity, vol. II, ed. V.L. Newhouse (Academic Press, New York, 1975) p. 542.
[2] D. Dimos, P. Chaudhari, J. Mannhart and F.K. LeGoues, Phys. Rev. Lett. 61 (1988) 219.
[3] S.S. Laderman, R.C. Taber, R.D. Jacowitz, J.L. Moll, C.B. Eom, T.L. Hylton, A.F. Marshall, T.H. Geballe and M.R. Beasley, Phys. Rev. B 43 (1991) 2922.
[4] B.H. Moeckly, S.E. Russek, D.K. Lathrop, R.A. Buhrman, J. Li and J.W. Mayer, Appl. Phys. Lett. 57 (1990) 1687.
[5] J. Mannhart, P. Chaudhari, D. Dimos, C.C. Tsuei and T.R. McGuire, Phys. Rev. Lett. 61 (1988) 2476.
[6] A. Iida and K. Kohra, Phys. Status Solidi A 51 (1979) 533.
[7] E. Koppensteiner, P. Hamberger, G. Bauer, V. Holy and E. Kasper, Appl. Phys. Lett. 64 (1994) 172.
[8] P.-Y. Chu, R.C. Buchanan, F. Gao, J.W. Kruse and M. Feng, Appl. Phys. Lett. 63 (1993) 3512.
[9] E.J. Cukauskas, L.H. Allen, G.K. Sherrill, R.T. Holm and C. Vold, J. Appl. Phys. 74 (1993) 6780.
[10] H. Fay and C.D. Brandle, J. Phys. Chem. Solids, Suppl. 1 (1967) 51.
[11] U.J. Cox, J. Crain, P.D. Hatton, G.S. Green and D.Y. Dai, J. Appl. Phys. 75 (1994) 7966.
[12] C.R. Li, Z.H. Mai, P.D. Hatton and C.H. Du, Acta Phys. Sinica 42 (1993) 1479.
[13] A.H. Carim, S.N. Basu and R.E. Muenchausen, Appl. Phys. Lett. 58 (1991) 871.
[14] J.Z. Sun, W.J. Gallagher, A.C. Callegari, V. Foglietti and R.H. Koch, Appl. Phys. Lett. 63 (1991) 1561.
[15] E. Ollson, G. Brorssen, P.A. Nilsson and T. Claeson, Appl. Phys. Lett. 63 (1993) 1569.
[16] S.N. Basu, T. Roy, T.E. Mitchell, R.E. Muenchausen and M. Nastasi, in: Proc. Conf. on Science and Technology of Thin Film Superconductors, 30 April–4 May 1990.
[17] C.W. Nieh, L. Anthony, J.Y. Josefowicz and F.G. Krajenbrink, Appl. Phys. Lett. 56 (1990) 2138.
[18] D. Bhatt, S.N. Basu, A.C. Westerheim and A.C. Anderson, Physica C 222 (1994) 283.

1995 PHYSICS, MATERIALS SCIENCE AND RELATED ENGINEERING JOURNALS

APPLIED SURFACE SCIENCE ❶
Volumes 82-92 (in 44 issues) Price: Dfl. 4521.00 (US$2379.00)

ASTROPARTICLE PHYSICS
Volume 3 (in 4 issues) Price: Dfl. 363.00 (US$191.00)

COMPUTATIONAL MATERIALS SCIENCE
Volumes 3-4 (in 8 issues) Price: Dfl. 850.00 (US$447.00)

COMPUTER PHYSICS COMMUNICATIONS
Volumes 86-92 (in 21 issues) Price: Dfl. 4368.00 (US$2299.00)

FLUID DYNAMICS RESEARCH
Volumes 15-16 (in 12 issues) Price: Dfl. 936.00 (US$493.00)

FUSION ENGINEERING AND DESIGN ❻
Volumes 27-30 (in 16 issues) Price: Sfrs. 2120.00 (US$1472.00)

JOURNAL OF CRYSTAL GROWTH
Volumes 146-157 (in 48 issues) Price: Dfl. 10080.00 (US$5305.00)

JOURNAL OF GEOMETRY AND PHYSICS
Volumes 15-17 (in 12 issues) Price: Dfl. 1053.00 (US$554.00)

JOURNAL OF LUMINESCENCE
Volumes 63-66 (in 24 issues) Price: Dfl. 2120.00 (US$1116.00)

JOURNAL OF MAGNETISM AND MAGNETIC MATERIALS
Volumes 138-149 (in 36 issues) Price: Dfl. 6564.00 (US$3455.00)

JOURNAL OF NON-CRYSTALLINE SOLIDS
Volumes 177-191 (in 45 issues) Price: Dfl. 6915.00 (US$3639.00)

JOURNAL OF NUCLEAR MATERIALS
Volumes 217-227 (in 33 issues) Price: Dfl. 6061.00 (US$3190.00)

JOURNAL OF WIND ENGINEERING AND INDUSTRIAL AERODYNAMICS
Volumes 53-58 (in 18 issues) Price: Dfl. 2562.00 (US$1348.00)

MATERIALS LETTERS
Volumes 23-25 (in 18 issues) Price: Dfl. 1350.00 (US$711.00)

MECHANICS OF MATERIALS
Volumes 19-21 (in 12 issues) Price: Dfl. 1350.00 (US$711.00)

NUCLEAR ENGINEERING AND DESIGN ❻
Volumes 155-162 (in 24 issues) Price: Sfrs.4240.00 (US$2944.00)

NUCLEAR INSTRUMENTS AND METHODS IN PHYSICS RESEARCH ❷
Section A: Accelerators, Spectrometers, Detectors and Associated Equipment
Volumes 352-366 (in 45 issues) Price: Dfl. 10740.00 (US$5652.00)

NUCLEAR INSTRUMENTS AND METHODS IN PHYSICS RESEARCH ❷
Section B: Beam Interactions with Materials and Atoms
Volumes 95-107 (in 52 issues) Price: Dfl. 9308.00 (US$4899.00)

NUCLEAR PHYSICS A ❸
Volumes 581-595 (in 60 issues) Price: Dfl. 9435.00 (US$4966.00)

NUCLEAR PHYSICS B ❸
Volumes 433-457 (in 75 issues) Price: Dfl. 15400.00 (US$8105.00)

NUCLEAR PHYSICS B - PROCEEDINGS SUPPLEMENTS ❸
Volumes 39-44 (in 18 issues) Price: Dfl. 2082.00 (US$1096.00)

OPTICAL MATERIALS
Volume 4 (in 6 issues) Price: Dfl. 580.00 (US$314.00)

OPTICS COMMUNICATIONS
Volumes 112-121 (in 60 issues) Price: Dfl. 4530.00 (US$2384.00)

PHYSICA A ❹
Statistical and Theoretical Physics
Volumes 212-222 (in 44 issues) Price: Dfl. 4851.00 (US$2553.00)

PHYSICA B ❹
Physics of Condensed Matter
Volumes 203-214 (in 48 issues) Price: Dfl. 5292.00 (US$2785.00)

PHYSICA C ❹
Superconductivity
Volumes 237-255 (in 76 issues) Price: Dfl. 8379.00 (US$4410.00)

PHYSICA D ❹
Nonlinear Phenomena
Volumes 79-88 (in 40 issues) Price: Dfl. 4410.00 (US$2321.00)

PHYSICS LETTERS A ❺
Volumes 198-210 (in 78 issues) Price: Dfl. 5005.00 (US$2634.00)

PHYSICS LETTERS B ❺
Volumes 341-364 (in 96 issues) Price: Dfl. 9240.00 (US$4863.00)

PHYSICS REPORTS ❺
Volumes 252-263 (in 72 issues) Price: Dfl. 4620.00 (US$2432.00)

SOLID STATE IONICS
Volumes 77-85 (in 36 issues) Price: Dfl. 3564.00 (US$1876.00)

SURFACE SCIENCE ❶
(Including Surface Science Letters)
Volumes 319-342 (in 72 issues) Price: Dfl. 12408.00 (US$6530.00)

SURFACE SCIENCE REPORTS ❶
Volumes 21-23 (in 24 issues) Price: Dfl. 1224.00 (US$644.00)

THEORETICAL AND APPLIED FRACTURE MECHANICS
Volumes 23-24 (in 6 issues) Price: Dfl. 902.00 (US$475.00)

ULTRAMICROSCOPY
Volumes 57-61 (in 20 issues) Price: Dfl. 2305.00 (US$1213.00)

WAVE MOTION
Volumes 21-22 (in 8 issues) Price: Dfl. 932.00 (US$491.00)

WEAR
Volumes 181-190 (in 20 issues) Price: Sfrs. 4050.00 (US$2812.00)

❶ - ❻ REDUCED RATES ARE AVAILABLE FOR COMBINED SUBSCRIPTIONS TO SETS OF THESE JOURNALS; PLEASE CONTACT THE PUBLISHER FOR DETAILS.

Dutch Guilder and Sfrs. price(s) quoted apply worldwide, except in the Americas (North, Central and South America). US Dollar price(s) quoted applies in the Americas only. Journals are sent by Surface Mail to all countries except to the following where Air Delivery via SAL mail is ensured at no extra cost to the subscriber: Argentina, Australia/New Zealand, Brazil, Hong Kong, India, Israel, Japan, Malaysia, Mexico, Pakistan, P.R. China, Singapore, S. Africa, S. Korea, Taiwan, Thailand, USA & Canada. Customers in the European Union should add the appropriate VAT rate applicable in their country to the price(s).

ELSEVIER SCIENCE B.V.

P.O. Box 103
1000 AC Amsterdam,
The Netherlands
Tel: (020) 4852320
Fax: (020) 4852580

In the USA & Canada:
Elsevier Science Inc.
Journals Fulfilment Department
P.O. Box 882, New York, NY 10159-0882
Tel:(212) 633 3950. Fax: (212) 633 3990

N·H

CHINESE JOURNAL OF PHYSICS VOL. 34, NO. 2-II APRIL 1996

Morphology and Interface Structure of Pulsed Laser Deposited $YBa_2Cu_3O_7$ Thin Films on $LaAlO_3$ Substrates†

W. J. Lin[1], J. H. Li[2], P. D. Hatton[1], and Z. H. Mai[2]

[1] *Department of Physics and Astronomy, The University of Edinburgh, Mayfield Road, Edinburgh, EH9 3JZ, UK*

[2] *Institute of Physics, Chinese Academy of Science, Beijing 10080, China*

(Received September 1, 1995)

The morphology of $YBa_2Cu_3O_7$ high-T_c superconducting thin films grown on $LaAlO_3$ substrates by pulsed laser deposition method have been studied by high resolution x-ray scattering and scanning electron microscopy. The results demonstrated that the thin films are almost complete c-oriented crystallised and twin in a-b plane, which is due to the orthorhombic structure. However, there are some a/b-oriented grains in the surface region of the thicker films. The interfacial strain were found in both the thin films and the substrates. The strain in the films, which is due to the lattice mismatch between the film and substrate, increases the dislocation density and makes the surface-parallel coherent length shorter. In the other hand, the strain in the substrates, which due to the mechanical polishing prior the growth, induces the inhomogeneous distortion on the substrates.

PACS. 61.50.Jr – Crystal morphology and orientation.
PACS. 68.60.-p – Physical properties of thin films, nonelectronic.
PACS. 74.76.Bz – High-T_c cuprate films.

Highly oriented thin-film high-T_c superconductors have been reported with improved superconducting properties than bulk materials. Amongst different superconducting material, $YBa_2Cu_3O_7$ (YBCO) thin films grown on $LaAlO_3$ (LAO) substrates by a variety of techniques such as pulsed laser ablation, sputtering, chemical co-evaporation, etc. have been intensely studied because they are excellent for microwave applications. It have been found that the superconductivity of the superconducting thin films is strongly related to their morphology and structure such as the film orientations, crystallising quality, grain boundaries and film/substrate interface. In this paper, a detail structural characterisation of YBCO-LAO thin film superconductors grown by pulsed laser deposition (PLD) method was reported and it shows that this technique can be used to fabricate high quality superconducting thin films.

YBCO-LAO thin film superconductors were grown by PLD method in the Institute of Physics, Chinese Academy of Science, Beijing, China. An XeCl excimer laser (308 nm,

† Refereed version of the contributed paper presented at the 1995 Taiwan International Conference on Superconductivity, August 8-11, 1995, Hualien, Taiwan, R.O.C.

40 ns) was employed for sample growth. The energy density of the laser was 3-5 J/cm^2. During the deposition, the temperature of the substrate surface was maintained at 770 °C and the oxygen pressure was 600 mTorr. The substrates used were commercial LAO wafers which have been mechanically polished already and have been chemically cleaned prior to the film deposition. Two samples were produced with different thickness which are estimated 3000 Å(sample 1) and 1000 Å(sample 2) respectively. Both samples have a sharp superconducting transition temperature around $T_c = 90K$ and a critical current density, J_c, in the range of $4.0\text{–}6.5 \times 10^6 A/cm^2$. The detail of the deposition process can be found in previous paper [1,2].

The samples were then investigated by high resolution triple-crystal x-ray diffraction (XRD). The diffractometer is based on a four-circle goniometer which mounted on a rotating anode x-ray generator operating at 2.7 KW with a copper target. $CuK_{\alpha 1}$ radiation ($\lambda = 1.54051$ Å, $\Delta\lambda = 0.00058$ Å) was employed in XRD experiments. Two different resolution modes were used by change both the monochromator and analyer. Pyrolytic graphite crystals were used in low resolution mode and the resolution is about $2 \times 10^{-2}\text{Å}^{-1}$. In high resolution mode, perfect germanium crystals were employed and the resolution was approximately $2 \times 10^{-4}\text{Å}^{-1}$ [3]. To obtain the surface morphology, the samples were also analysed by scanning electron microscopy (SEM). The SEM measurements utilised a Cambridge S250 SEM operating at $5 - 10KV$ accelerating voltage.

The observation of the scattered x-ray intensity around the LAO $(002)_s$ reciprocal lattice point (The subscripts of the coordinate indicate the index system. "s" means the substrate system which follow the pseudo-cubic system. "f" means the thin film system.) of sample 1 is shown in Fig. 1. Two peaks are clearly observed: the intense $(002)_s$ reflection and a weaker peak at (0,0,1.944) which comes from the $(006)_f$ reflection from the films. From this figure, it is easy to find that the film is well crystallised. The Full-Width-Half-Maxima (FWHM) of $(006)_f$ reflection both along surface-parallel and surface-normal directions from both sample 1 and 2 are shown in Table I. The associated coherent-length are also calculated which is closely related to the dislocation density or "grain size" in the direction (The term "grain size" is used in powder diffraction for nearly spherical grains.

TABLE I. The quality factors of $YBa_2Cu_3O_7$–$LaAlO_3$ thin films. Where RLU means the Reciprocal Lattice Unit.

		Surface normal		Surface parallel	
Sample #	Thickness (Å)	FWHM (RLU)	Coherent Length(Å)	FWHM (RLU)	Coherent Length(Å)
#1	3000	0.0044	807 ± 69	0.0123	289 ± 9
#2	1000	0.0101	352 ± 13	0.0239	149 ± 3

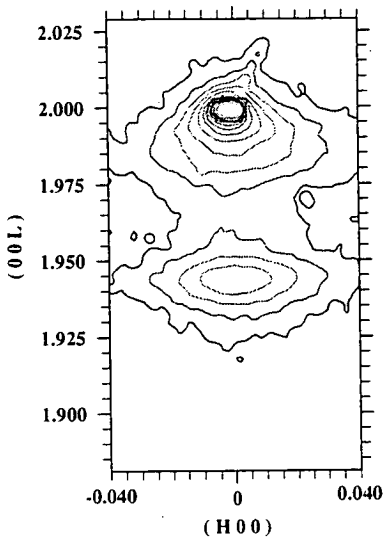

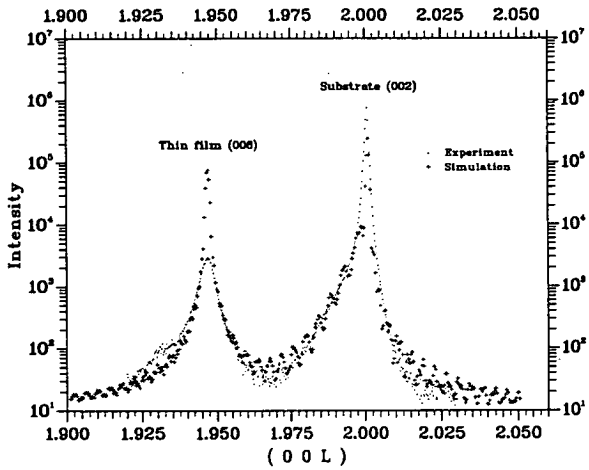

FIG. 1. The isointensity contour plot of the x-ray scattering intensity around the (002) substrate reciprocal lattice point of sample 1 showing the additional scattering centred around (0 0 1.944) which is the (006) Bragg peak from the $YBa_2Cu_3O_7$ thin film. The contour levels have been chosen to accentuate the weaker features.

FIG. 2. The longitudinal scan around the (002) substrate reflection from the sample 1. The simulation which involves a strain field existing in the substrate is also included.

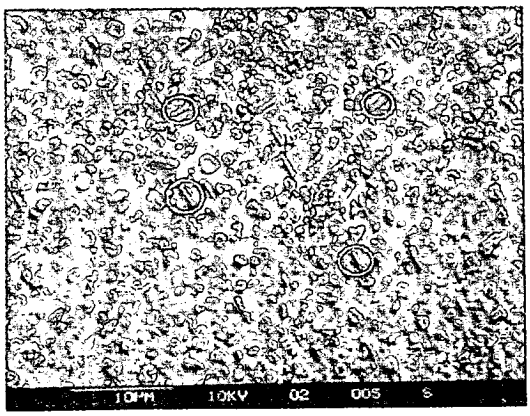

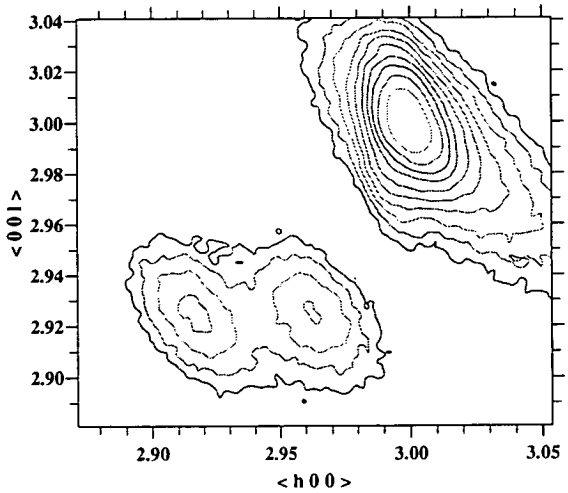

FIG. 3. The SEM surface micrograph of sample 1. The large majority of the crystallites are c-axis oriented, but a few (circled) are a/b-oriented grains.

FIG. 4. The isointensity contour map of the x-ray scattering intensity around the (303) substrate reciprocal lattice point of sample 1, showing two weaker reflections centred at (2.964 0 2.926) and (2.914 0 2.926) which are the (309) and (039) Bragg peaks from the $YBa_2Cu_3O_7$ thin film.

However, YBCO grains are an-isotropic. For this reason, "coherent length" are used in this paper, rather than "grain size".). The results present that the thicker film has better quality. This might be due to larger dislocation density around the interface area which is caused by the interfacial strain. Shorter coherent length along surface parallel direction presents that the films have denser defects on the surface direction although the surface normal direction is much better epitaxied.

The one-dimensional longitudinal scan about $(002)_s$ is shown in Fig. 2 under semi-log plot. Both the $(002)_s$ substrate and the $(006)_f$ thin-film reflection peaks are still clearly observed. However, there is not any significant indication of the scattering which comes from a/b-oriented grains as found previously at (0,0,1.9745) [4]. To verify the absence of a/b-oriented crystallites, we examined the surface morphology of the samples with SEM. Fig. 3 shows the surface micrograph of sample 1. It is composed primarily of c-oriented grains but there are also a few rectangular elongated grains which are a/b-oriented. These grains (examples of which are circled in Fig. 3) comprise about 3% area of the surface. Simulations of the x-ray scattering using such an orientational ratio strongly suggests that they would be observable in our experiments. We, therefore, conclude that the proportion of the a/b-oriented grains is far less buried within the thin-film but that they preferentially exist at the surface. The other SEM result of sample 2 presents a clear surface without a/b-oriented grains. This is the other evidence that the a/b-oriented grains only exist far away from interface.

Another noticeable feature in Fig. 2 is that the asymmetry peak shape of the substrate peak with an extended tail at lower l in the $(00l)$ direction. Initially, we investigated whether the asymmetry could be caused by interference effects between the substrate reflection and an a/b-oriented thin film reflection. This was examined by computer simulations which were performed based on crystal truncation rod scattering expressions [5]. All such attempts provided a poor fit to the observed data and hence we confirm that there is no evidence for an appreciable number of the a/b-oriented grains. However, the simulation results suggest, surprisingly, that a modification of the substrate lattice parameter was required, which was consistent with interfacial strain. To investigate the interfacial strain, a bare substrate crystal which had been polished prior to thin film deposition was studied. Again, the asymmetric profiles were observed around all reflections which could be modelled by a strained layer of substrate which exponentially increased the lattice parameter from the bulk value ($c_0 = 3.78$ Å) at about 3000 Åunder the surface to a larger value ($c' = 3.82$ Å) on the surface. Such surface damage is presumably caused by the mechanical polishing damage of the substrate prior to growth which is used to produce an optically smooth surface. The observed increase of the lattice parameter close to the substrate surface is consistent with an increased dislocation density caused by mechanical polishing. A kinematical simulation result of the scattering expected from 3000 Åthick sample with a similar interfacial strain in the uppermost layers of the substrate is shown with the experimental data in Fig. 2. The simulation correctly models the asymmetry and provides a close fit to the data around the Bragg reflections. The Bragg reflections themselves are not accurately modelled because of dynamical effects which are not modelled in our kinematical simulation.

In addition to the morphology, x-ray scattering can also provide information on the structure of the film. Fig. 4 shows a 2-dimensional x-ray scattering map around the $(303)_s$ reflection. In this map, three peaks are clearly observed, the intense $(303)_s$ reflection and

two weaker peaks at (2.9635, 0, 2.9256) and (2.9138, 0, 2.9256) which are due to $(309)_f$ and $(039)_f$ reflections respectively. The separation of these two peaks indicates that the films have orthorhombic structure and twinned. The lattice parameters are determined which $a_f = 3.822$ Å, $b_f = 3.887$ Åand $c_f = 11.622$ Å. In comparison with the bulk YBCO lattice parameter values [6], the differences are below 0.02% in a, b and 0.5% in c ($\Delta_a = 0.020\%$, $\Delta_b = 0.001\%$ and $\Delta_c = 0.495\%$).

We have examined the morphology of YBCO thin films grown on LAO substrates by PLD method. The YBCO thin films were found orthorhombic structure and twinned. The lattice parameters were measured and found close to bulk values. The XRD and SEM results present that the YBCO films are almost complete c-oriented with some a/b-grains concentrated in the surface region of the thicker film. The phenomenon is related to the accumulation of the stress of the lattice mismatch between the film and the substrate. This is also the reason why the error of the c lattice parameter of YBCO is larger than that of a or b. The interfacial strain is found in both thin films and substrate. The shorter coherent length along the surface-parallel direction indicate that there are more defects which are due to the interface sheer strain. The inhomogeneously strained interface region within the substrate surface was found in simulation of the x-ray scattering. This is a very surprising result because other reports have found strain fields in the thin films but not in the substrates. The increase of the lattice parameter of the strained substrate effects a reduced lattice mismatch which could results in improved morphological quality of the films. We believe that this strain is due to mechanical polishing of the substrate prior to thin films growth.

We are grateful to H. Vass for his excellent technical assistance throughout and to Xu Shifa for the sample growth. Partial financial support for our programme was obtained from the Engineering and Physical Sciences Research Council, the Royal Society and the Chinese Academy of Sciences.

References

[1] Q. X. Su, S. F. Xu, D. F. Cui, H. B. Lu, Y. J. Tian, Y. Z. Zhang, Z. H. Chen, L. Li, and G. Z. Yang, Modern Phys. Lett. **B6** 477 (1992).

[2] J. H. Li, W. J. Lin, P. D. Hatton, Z. H. Mai, and S. F. Xu, Physica **C245** 139 (1995).

[3] C. A. Lucas, E. Gartstein, and R. A. Cowley, Acta Cryst. **A45** 416 (1989).

[4] U. J. Cox, J. Crain, P. D. Hatton, G. S. Green, and D. Y. Dai, J. Appl. Phys. **75** 7966 (1994).

[5] I. K. Robinson, Phys. Rev. **B33** 3830 (1986).

[6] J. D. Jorgensen, B. W. Veal, A. P. Paulikas, L. J. Nowicki, G. W. Crabtree, H. Claus, and W. K. Kwok, Phys. Rev. **B41** 1863 (1990).

Systematic X-Ray Diffraction Study of $Ba_{1-x}K_xBiO_3$ Single Crystals†

T. J. Lee[1], A. Wang[1], H. K. Fun[2], Cheng-Hung Chou[1], H. Y. Tang[3], C. M. Lei[3], M. K. Wu[3], L. S. Liou[4], and J. C. Wang[4]

[1]*Department of Physics, National Tsing Hua University, Hsinchu, Taiwan 300, R.O.C.*

[2]*X-ray Crystallography Unit, School of Physics, Universiti Sains Malaysia, 11800. USM Penang, Malaysia*

[3]*Materials Science Center, National Tsing Hua University, Hsinchu, Taiwan 300, R.O.C.*

[4]*Department of Chemistry, Soochow University, Taipei, Taiwan 111, R.O.C.*

(Received September 1, 1995)

Crystal structures of ten $Ba_{1-x}K_xBiO_3$ single crystals (BKBO), grown by the anodic electrocrystallization process, were analysed to compare with previous studies on sintered powder samples. Results show that BKBO prepared in this way exhibit the same crystal symmetry of space group Pm3m for a wide range of x-values (0.39 to 0.66) and also indicates that there are solubility distrbutions both for potassium and oxygen. Oxygen deficiency lowers the superconducting transition temperature T_c. Electron density maps, calculated from room temperature X-ray diffraction data, do not show conspicuous difference between superconducting and nonsuperconducting samples.

PACS. 74.70.-b - Superconducting materials.
PACS. 74.62.Bf - Effects of material synthesis, crystal structure, and chemical composition.
PACS. 61.10.-i - X-ray diffraction and scattering.

Sleight [1] discovered in 1975 that $BaPb_{1-x}Bi_xO_{3-y}$ (BPBO) exhibits superconductivity with a transition temperature near 12 K. In 1981 Wu *et al.* [2] revealed that the superconducting phenomenon exists in some range of the doped Pb content, and the highest T_c appears at the metal-semiconductor transition point.

Partially inspired by the research on BPBO, Bednorz and Müller [3] discovered a new superconductor La-Ba-Cu-O with T_c close to 35 K in 1986. This achievement gave a big boost to the superconductivity research. By calculating the electron band structure, Mattheiss *et al.* [4] suggested in 1988 that doping impurity atoms into $BaBiO_3$ may raise its T_c. Immediately, Cava's *et al.* [5] grew a highly pure phase of $Ba_{1-x}K_xBiO_3$ (x=0.4) with an onset T_c near 30 K.

Previous investigations [6-8] of BKBO showed that its structure depends on the content of doped potassium atom . Using neutron diffraction technique, Pei *et al.* [9]

† Refereed version of the contributed paper presented at the 1995 Taiwan International Conference on Superconductivity, August 8-11, 1995, Hualien, Taiwan, R.O.C.